UNIVERSITY OF CALIFORNIA, SAN DIEGO

Preparation and Characterization of Calcium Phosphate Ceramics and Composites as Bone Substitutes

A dissertation submitted in partial satisfaction of the

requirements for the degree Doctor of Philosophy

in

Materials Science and Engineering

by

Xing Zhang

Committee in Charge:

Professor Kenneth S. Vecchio, Chair
Professor Prabhaker Bandaru
Professor Sadik C. Esener
Professor Michael J. Heller
Professor Robert Sah

2007

The dissertation of Xing Zhang is approved, and it is acceptable in quality and form for publication on microfilm:

Chair

University of California, San Diego

2007

TABLE OF CONTENTS

LIST OF FIGURES

LIST OF TABLES

ACKNOWLEDGEMENTS

I wish to acknowledge and deeply thank my advisor, Professor Kenneth S. Vechhio, for his strong encouragement, support, and direction during the course of this research. I would also like to thank Director Jennifer B. Massie, Professor Choll W. Kim and Mark Wang in Department of Orthopaedics at UCSD, for their collaboration with the in-vivo testing and further analysis.

I wish to express my gratefulness to my committee members for their time and helpful suggestions: Professor Prabhaker Bandaru, Professor Sadik C. Esener, Professor Michael J. Heller and Professor Robert Sah.

I would like to recognize my colleagues for their assistance and help in the lab: Dr. Fengchen Jiang, Dr. Raghav Adharapurapu, Todd Groth, Brandon Reynante, Christian Deck, Gregg McKee, Hesham Khalifa, Jason Flowers, John Miessner, Justin Cheney, and Robb Kulin. I would also thank my dear friends, I-Chen Chen, Yuhui Cheng, Xiangrong Ye and others for their help during my Ph.D. study.

I graciously acknowledge the financial support, a grant from the von Liebig Foundation in the Jacobs School of Engineering at UC San Diego.

Finally, I wish to thank my parents, sister and other family members for their concern and encouragement all the time. I also wish to thank all the other friends and colleagues who gave me help and encouragement.

Chapter 4, in part, was a reprint of the materials in previous publications: 1. K.S. Vecchio, X. Zhang, J.B. Massie, M. Wang, C.W. Kim. *Acta Biomaterialia* 2007, 3:910-

918; 2. K.S. Vecchio, X. Zhang, J.B. Massie, M. Wang, C.W. Kim. *Acta Biomaterialia* 2007; 3:785-793; 3. X. Zhang, K.S. Vecchio. *Materials Science and Engineering C* 2006; 26: 1445-1450.

Chapter 5, in part, was a reprint of the materials in the previous publication: X. Zhang, K.S. Vecchio. *Journal of Crystal Growth* 2007, 308:133-140.

Chapter 6, in part, was a reprint of the materials in the manuscript: X. Zhang, F. Jiang, T. Groth and K.S. Vecchio. Preparation, Characterization and Mechanical performance of β-TCP Ceramics with/without Magnesium Substitution. Submitted to *Journal of Materials Science: Materials in Medicine*.

CURRICULUM VITAE

Eduation

Ph.D. in *Materials Science and Engineering*, University of California, San Diego (UCSD), December, 2007.

M.S. in *Materials Science and Engineering*, University of California, San Diego (UCSD), July, 2004.

B.S. in *Materials Science and Engineering*, University of Science and Technology of China (USTC), July, 2003.

Publications

X. Zhang, F. Jiang, T. Groth and K.S. Vecchio. **Preparation, Characterization and Mechanical performance of β-TCP Ceramics with/without Magnesium Substitution**. Submitted to *Journal of Materials Science: Materials in Medicine*.

X. Zhang, K.S. Vecchio. **Hydrothermal Synthesis of Hydroxyapatite Rods**. *Journal of Crystal Growth* 2007, 308:133-140.

K.S. Vecchio, X. Zhang, J.B. Massie, M. Wang, C.W. Kim. **Conversion of Bulk Seashells to Biocompatible Hydroxyapatite for Bone Implants**. *Acta Biomaterialia* 2007, 3:910-918.

K.S. Vecchio, X. Zhang, J.B. Massie, M. Wang, C.W. Kim. **Conversion of Sea Urchin Spines to Mg-substituted Tricalcium Phosphate for Bone Implants**. *Acta Biomaterialia* 2007; 3:785-793.

X. Zhang, K.S. Vecchio. **Creation of Dense Hydroxyapatite (Synthetic Bone) by Hydrothermal Conversion of Seashells**. *Materials Science and Engineering C* 2006; 26: 1445-1450.

Selected presentations

X. Zhang, K.S. Vecchio, J.B. Massie, M. Wang, C.W. Kim. **Hydrothermal Conversion of Marine Skeletons to Calcium Phosphates**. Poster in SFB conference, Chicago, Illinois, April 2007.

X. Zhang, K.S. Vecchio. **Preparation of Bioresorbable Magnesium-substituted Tricalcium Phosphate Ceramics**. Poster in SFB conference, Chicago, Illinois, April 2007.

X. Zhang, K.S. Vecchio. **Synthetic Bone Substitutes Derived from Marine Materials: A Comprehensive Study of Microstructure, Mechanical and Biological Properties**. Presentation in TMS conference, Orlando, Florida, February 2007.

K.S. Vecchio, X. Zhang. **Creation of Nanostructured Hydroxyapatite (Synthetic Bone) by Hydrothermal Conversion of Seashells**. Presentation in TMS conference, San Francisco, California, March 2005.

ABSTRACT OF THE DISSERTATION

Preparation and Characterization of Calcium Phosphate

Ceramics and Composites as Bone Substitutes

by

Xing Zhang

Doctor of Philosophy in Materials Science and Engineering

University of California, San Diego, 2007

Professor Kenneth S. Vecchio, Chair

Marine $CaCO_3$ skeletons have tailored architectures created by nature, which give them structural support and other functions. For example, seashells have dense lamellar structures, while coral, cuttlebone and sea urchin spines have interconnected porous structures. In our experiments, seashells, coral and cuttlebone were hydrothermally converted to hydroxyapatite (HAP), and sea urchin spines were converted to Mg–substituted tricalcium phosphate (β-TCMP), while maintaining their original structures. Partially converted shell samples have mechanical strength, which is close to that of compact human bone. After implantation of converted shell and spine samples in rat femoral defects for 6 weeks, there was newly formed bone growth up to and around the implants. Some new bone was found to migrate through the pores of converted spine samples and grow inward. These results show good bioactivity and osteoconductivity

of the implants, indicating the converted shell and spine samples can be used as bone defect fillers.

Calcium phosphate powders were prepared through different synthesis methods. Micro-size HAP rods were synthesized by hydrothermal method through a nucleation-growth mechanism. On the other hand, HAP particles, which have good crystallinity, were prepared by wet precipitation with further hydrothermal treatment. β-TCP or β-TCMP powders were prepared by a two-step process: wet precipitation of apatitic tricalcium phosphate ('precursor') and calcination of the precursor at 800℃ for 3 hours. β-TCMP or β-TCP powders were also prepared by solid-state reactions from $CaHPO_4$ and $CaCO_3$ with/without MgO. Biphasic calcium phosphate, which is mixture of HAP and β-TCP, can be prepared though mechanical mixing of HAP and β-TCP powders synthesized as above.

Dense β-TCP and β-TCMP ceramics can be produced by pressing green bodies at 100MPa and further sintering above 1100℃ for 2 hours. β-TCMP ceramics ~99.4% relative dense were prepared by this method. Dense β-TCP ceramics have average strength up to 540MPa. Macroporous β-TCMP ceramics were produced with sucrose as the porogen following a two-step pressing method. Porous β-TCMP ceramics were also prepared by replication of polyurethane sponge. β-TCMP ceramics with porous structures in the center surrounded by dense structures were created. The outside dense structures give the scaffold mechanical strength, while the central porous structures enable cells migration and vascular infiltration, and finally in-growth of new bone into the scaffold.

1 INTRODUCTION

The regeneration potential of human bone appears to be limited, given in the ability to repair large bone defects, such as those associated with comminuted fractures or bone tumor resection. In these cases, autograft, allograft and bone graft materials have been widely used. Autograft bone is bone transplanted from one part of body to another in the same individual. Allograft is the transplant of bone from one individual to another of the same species.

Autograft bone has long been considered as the gold standard for graft material [1]. Autograft does not carry the risk of transmissible disease, and it is highly osteoinductive. Disadvantages of this material include increased operative time, morbidity of the donor site, insufficient quantity. Alternatively, an allograft is used [2], so as to avoid morbidities often associated with an autograft. However, there are some disadvantages of allograft bone, such as delayed time to fusion, increased rate of nonunion, delayed or incomplete graft incorporation because of an immune response elicited by the graft, transmission of infection, poor osteoinductive capabilities, and less osteogenic competence as compared with autograft. Another issue is the high cost of the bone banking system for allografts.

Considering the disadvantages of autograft and allograft, synthetic bone graft materials, such as calcium phosphate based ceramics and cements, and a variety of of polymers and composites, have been widely studied and used [3-7]. The use of calcium phosphates (CaPs) for bone substitution, augmentation and repair has gained clinical

acceptance in many areas of orthopedics and dentistry. Dental applications include fillers for periodontal bony defects, alveolar ridge augmentation, immediate tooth root replacement, coating for dental metal implants and maxillofacial reconstruction [8-12]. Medical applications include ear implants, spine fusion, repair of bony defects, and coating for orthopedic metal implants [13-15].

CaPs differ in composition from each other, reflecting the differences in their origin (e.g. natural or synthetic) and methods of preparation, and can be prepared in different physical forms, e.g. dense, microporous and/or macroporous particles or blocks. Among them, hydroxyapatite [$Ca_{10}(PO_4)_6(OH)_2$, HAP] and β-tricalcium phosphate [$Ca_3(PO_4)_2$, β-TCP] are widely used in orthopedic applications. Both HAP and β-TCP are biocompatible and bioactive, which can directly form bonding to bony tissue. HAP is poorly resorbable, and will remain for years after the implantation, while β-TCP has much faster resorption rate, absorbed in ~3-6 months in-vivo. To control the resorption rate, biphasic calcium phosphates (BCP), which consist of HAP and β-TCP combined, have been investigated. The resorption rate of BCP depends on the molar ratio of β-TCP/HAP in the mixture. The higher the ratio, the faster the resorption.

In this investigation, hydrothermal, wet precipitation and solid-state reactions were employed to synthesize calcium phosphates. Material properties, such as crystalline phases, thermal properties, chemical bonding, particle size and morphology of these calcium phosphates or composites were characterized by a variety of instruments. Synthetic bone substitutes were either hydrothermally converted from marine $CaCO_3$ skeletons or produced by ceramic sintering. The mechanical and biological properties of

synthetic bone substitutes were evaluated by mechanical tests and in-vivo tests in rat femur defects.

Chapter 2 gives a brief background of the history, properties, synthesis, and applications of bone graft materials. Background on bone and bone repair are also included.

Chapter 3 discusses the experimental setup, important experimental methods and reaction equations. Characterization methods are also included.

Chapter 4 describes the experimental results from hydrothermal conversion of marine $CaCO_3$ skeletons to calcium phosphates. The conversion mechanisms and microstructures of the products are well studied. Results from mechanical tests of some products and in-vivo tests of the implants are included.

Chapter 5 is about synthesis and characterization of HAP powders. The growth mechanism of HAP rods is discussed. A two-step method to synthesize good crystalline HAP particles is introduced.

Chapter 6 discusses preparation and characterization of β-TCP and β-TCMP ceramics. Synthesis of β-TCP or β-TCMP by two-step preparation and solid-state reactions are discussed. Preparation of dense ceramics, porous ceramics and bone-mimicking ceramics with porous structure in the center with dense structure outside are described. Effects of Mg substitution on the phase transformation, densification and mechanical performance of ceramics are investigated.

Chapter 7 includes a summary and suggested future work.

2 BACKGROUND

For more than a century, research has been conducted with the goal of finding a suitable material to repair or replace bony segments of the musculoskeletal system. First reproducible investigations for bone regeneration are present from the 18th century by Duhamel du Monceau. He showed with silver wire loops wraped around bones of young animals, that the coil of the wire came to lie closer to the marrow cavity during the process of growth. He concluded this was a phenomenon similar to the growth of a tree. In 1821, von Walter described the successful clinical application of an autogenous bone transplant for the first time in Germany [16]. Ollier [17] used the periosteum for the formation of new bone and represented the view that autogenous bone covered with periosteum can survive, when being transplanted.

In 1889, Senn [18] reported on muriatic acid-decalcified ox bone for use in filling defects caused by tumor removal or osteomyelitis, representing the use of bone substitutes. Gluck [19] filled bone defects with ivory cylinders in 1891. Since then, the common practice to fill bone defects with bone substitutes has become accepted. The first bone bank for the use of allogenic transplants was established in 1945 in New York by Bush and Garber [20]. In 1965, Urist [21] demonstrated the presence of a bone morphogenic protein (BMP) in the bone matrix. The use of xenogenic bone substitutes ended around 1986.

2.1 Basics of bone

Bone is a remarkable living tissue, which performs several key functions within the body. Bone functions to move, support, and protect the various organs of the body, produces red and white blood cells and store minerals. Bone is a living, highly vascular, dynamic, mineralized, connective tissue, which is characterized by its hardness, resilience and growth mechanisms, and its ability to remodel and repair itself. Simply, bone is a dense multi-phase material made up of cells embedded in a matrix composed of both organic (collagen fibres, lipids, peptides, proteins, glycoproteins, polysaccharides and citrates) and inorganic (calcium-phosphates, carbonates, sodium, magnesium and fluoride salts) elements [22]. Bone in its natural environment is engaged in a constant cycle of resorption and renewal, undergoing continual chemical exchange and structural remodelling, due to both internal hormonal regulation and external mechanical demands. There are total 206 bones in the adult body, and in five types: long, short, flat, irregular and sesamoid.

2.1.1 Bone structure

Mature bone has two architechtural forms: trabecular, also called cancellous or spongy bone (around 20% of the total skeleton), and cortical or compact bone (around 80% of the total skeleton). Bone surfaces consist of cortical bone, and the thickness of this protective layer increases in mechanically demanding regions such as the shafts of long bones, while cancellous bone is found in the interior of bones, such as within the femoral head and vertebra. Lamellar bone (Figure 2-1) exists on the periosteol surface

of long bones, as interstitial lamellae and concentric lamellae of osteons in osteonal bone, and within trabeculae of trabecular bone [23].

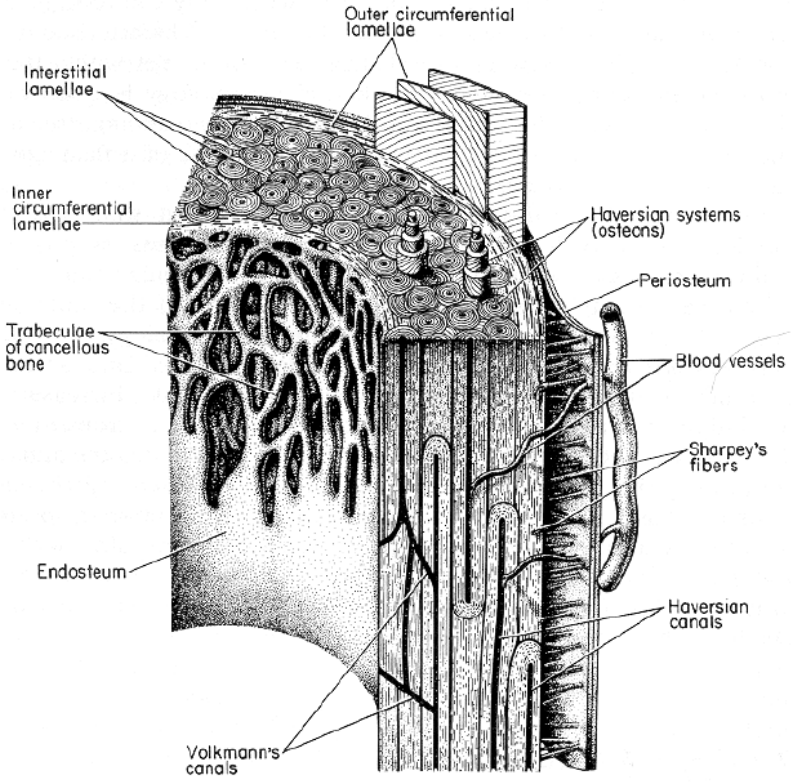

Figure 2-1. Illustration of Lamellar bone structure

The mechanical properties of bone and bone components are shown in Table 2-1 [24]. Cortical bone has much higher strength than that of cancellous bone, which only has a compressive strength of about 1-10 MPa. On an elementary level, the fabric of bone may be split into three main components: bone matrix, bone cells, bone marrow and its associated vascular network. The bone matrix provides mechanical strength and acts as the body's mineral store, the various bone cells are responsible for maintaining the structure of the matrix, regulating its oxygen and nutrient supply, and storing or

releasing minerals as required. The marrow and vasculature provides the source of stem cells, and the main means of communication and interaction with the rest of the body.

Table 2-1. The mechanical properties of bone and bone components.

	Testing direction	Compressive strength (MPa)	Tensile strength (MPa)	Young's modulus (GPa)
Cortical bone	longitudinal	193	133-150	17-25
	transverse	133	50	12
Cancellous bone	longitudinal	3.6-9.3	-	0.26-0.90
	transverse	0.6-4.9	-	0.01-0.40
Hydroxyapatite	n/a	-	9-120	80-117
Collagen	longitudinal	-	100	1.5

2.1.2 The matrix

The extra-cellular matrix has two main components: the organic collagen fibres and the inorganic bone mineral crystals. Together they make up ~95% of the dry weight of bone, and the other 5% is composed of organic molecules and 'amorphous' or poorly crystalline inorganic salts. Figure 2-2 shows the hierarchical organization of collagen fibres and bone minerals.

Collagen is the most abundant protein found in the body, and occurs in a number of different connective tissues both calcified and non-calcified, such as skin. Collagen accounts for 70 – 90% of the non-mineralized component of the bone matrix and varies from an almost random network of coarse bundles to a highly organized system of parallel-fibred sheets or helical bundles. Collagen consists of carefully arranged arrays of tropocollagen molecules, which are long rigid molecules (300 nm long and 1.2 nm

wide) as shown in Figure 2-2, composed of three left-handed helices of peptides known as α-chains that are bound together in a right-handed triple helix. To date, there are more than 22 different types of collagen that have been identified, with the most common being types I-IV. Bone contains mostly of type-I collagen, which accounts for 90% of the body's total collagen.

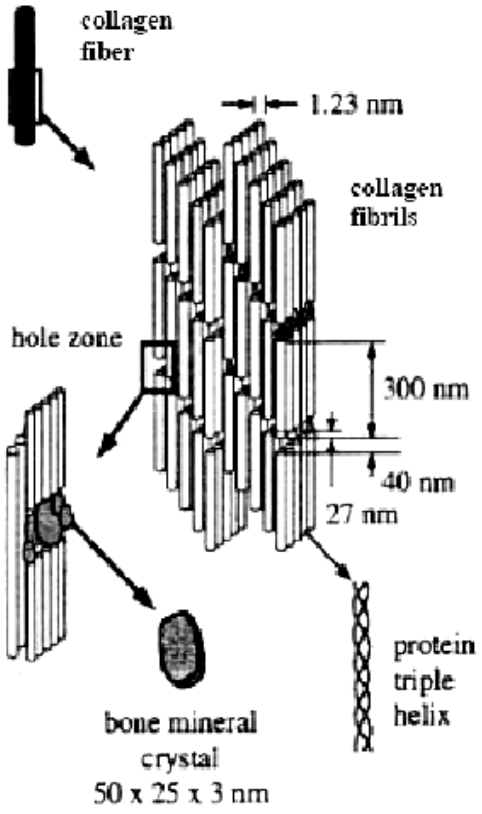

Figure 2-2. Hierarchical organization of collagen fibres and bone minerals.

The main inorganic crystal phase within bone is called biological apatite, which is characterized by calcium, phosphate and hydroxyl (reported Ca:P ratios of 1.37 – 1.87) [25, 26]. Significant levels of additional trace elements are present within bone mineral,

shown in Table 2-2 [27]. Bone apatite is not a direct analogue of HAP, as is commonly believed, but more closely related to an A – B type carbonate-substituted apatite [28, 29]. Type A is a CO_3-for-OH substitution, and type B is CO_3-for-PO4 substitution.

Table 2-2. Composition of inorganic phases of adult human bone.

Component	Weight percentage
Calcium, Ca^{2+}	34.8
Phosphorus, as P	15.2
Sodium, Na^{+}	1.71
Magnesium, Mg^{2+}	0.72
Potassium, K^{+}	0.03
Carbonate, as CO_3^{2-}	7.4
Fluoride, F^{-}	0.03
Chloride, Cl^{-}	0.13
Pyrophosphate, $P_2O_7^{4-}$	0.07
Total inorganic	65.0
Total organic	25.0
Absorbed H_2O	10.0
Trace elements: Sr^{2+}, Pb^{2+}, Zn^{2+}, Cu^{2+}, Fe^{3+}, etc.	

There is some disagreement about the exact mechanisms of the mineralization in bone, although many investigators agree that mineralization originates within matrix vesicles. Generally amorphous calcium phosphates with a Ca:P ratio varying between 1.44 and 1.55 are believed to be deposited under the control of osteoblasts. Once deposited, this amorphous tricalcium phosphate is present as a reservoir for apatite crystallite nucleation and growth independently of the cells [30]. Other organic substances present in the matrix have long been thought to be responsible for promoting the initial nucleation and deposition of bio-apatite, and regulating the orientation, size and growth rate of the crystals.

Growth factors (GFs) are peptides that are secreted by many cell types and function as signaling molecules. The binding of a growth factor to its receptor initiates intracellular signaling that will lead to different events, such as promoting and/or prevention of cell adhesion, migration, proliferation and differentiation. Bone GFs influence the synthesis of new bone by acting on the local cell population present in bone marrow and on bone surfaces. Among these proteins, bone morphogenetic proteins (BMPs) are among the most potent osteoinductive factors. BMPs belong to the transforming growth factor beta (TGF-β) supergene family, which currently has 43 members. BMP2 and BMP7 are being clinically applied for fractures and non-unions for a limited number of patients.

2.1.3 Bone cells

There are many cells associated with bone. Among them, three are of special interest: the osteoblast, osteocyte and osteoclast, which are responsible for the production, maintenance, and resorption of bone, respectively.

Osteoblasts are the cells that form new bone, which have only one nucleus, come from the bone marrow and are related to structural cells. Osteoblasts produce new bone called "osteoid" which is made of bone collagen and other protein. Then osteoblasts control calcium and mineral deposition to form new bone. After the team of osteoblasts has finished filling in a cavity, the cells become flat. They line the surface of the bone. These old osteoblasts are also called lining cells.

Osteocytes are cells inside the bone, which come from osteoblasts. Some of the osteoblasts turn into osteocytes while the new bone is being formed, and the osteocytes

then get surrounded by new bone. They are not isolated, however, because they send out long branches that connect to the other osteocytes. These cells can sense pressures or cracks in the bone and help to direct where osteoclasts will dissolve the bone.

Osteoclasts are large cells that dissolve the bone, which come from the bone marrow and are related to white blood cells. They are formed from two or more cells that fuse together, so the osteoclasts usually have more than one nucleus. They are found on the surface of the bone mineral next to the dissolving bone.

However, these three types of cells are highly specialized differentiated cells and do not generally proliferate (replicate). Less differentiated (immature) cells are generally known as stem cells and in the case of bone formation are often referred to as osteogenic cells. The osteogenic bone-forming cells originate from the mesenchymal bone marrow stromal cell line and exist in the endosteum and periosteum. Biochemical signalling molecules stimulated during remodelling and fracture healing result in local population increases in these cells.

2.1.4 Bone repair

Bone is unique among all vertebrate tissue in its ability to heal via the formation of new bone; all other tissue, such as heart, muscle and brain heal by replacement with connective tissue rather than original tissue. Fractured bone invariably heals through endochondral ossification in a five-step process [31].

(i) Firstly, a haematoma (blood clot) is formed, resulting from injury to the periosteum and local soft tissue.

(ii) As a consequence of this disruption in the blood supply, osteocytes nearest to the fracture die, resulting in local necrosis of the bone around the fracture. Simultaneously, there is a demand for the repair of the bone, the stabilization of the damaged area and the removal of the dead tissue.

(iii) In response to this, macrophages and fibroblasts are recruited to the site to remove tissue debris and to express extracellular matrix, respectively. In response to growth factors and cytokines released by these inflammatory cells, mesenchymal stem cells are recruited from the bone marrow and periosteum, which then proliferate and differentiate into osteoprogenitor cells.

(iv) This leads to an apparent thickening of the periosteum and the production of collars of external fracture callus around the fracture site. Those osteoprogenitor cells that lie close to undamaged bone (and are thus within reach of a ready supply of oxygen) differentiate into osteoblasts and form the osteoid, which is rapidly calcified into bone, while those farther away become chondroblasts and form cartilage. Angiogenesis is induced concurrently and, almost as soon as the cartilage has been formed. The fracture site is stabilized, and is replaced by woven cancellous bone, via endochondral ossification, in which osteoclasts and osteoprogenitor cells invade the cartilaginous callus preceded by capillary formation.

(v) The uncalcified material is resorbed and new bone is deposited on the remaining spinicules of calcified cartilage. The woven bone is then remodelled into lamellar bone and the process is completed by the return of

normal bone marrow within cancellous regions, while in repairing cortical bone the spaces between trabeculae are gradually filled in with successive layers of bone so forming new Haversian canals. Thus load-bearing capabilities and a new vascular network are restored.

Although bone has the ability to heal by itself, the regeneration potential appears to be limited in some cases, such as repair of large bone defects. In these cases, autograft, allograft and bone graft materials have to be used.

2.2 Autogenous bone grafts

When it is necessary to fill a bony defect, autogenous bone remains the 'gold standard' for bone grafts. Autogenous bone grafts may contain an osteoconductive matrix, osteoinductive proteins and osteogenic cells. Autografts are completely histocompatible, and don't have disease transmission issues. Available autogenous bone grafts include cancellous, vascularized cortical, nonvascularized cortical, and autogenous bone marrow grafts.

Autogenous cancellous bone is easily revascularized and is rapidly incorporated into the recipient site, but does not provide substantial structural support. Cancellous grafts act as osteoconductive substrates, which support the ingrowth of bone vessels and the infiltration of new osteoblasts and osteoblast progenitors. Cancelllous bone also releases osteoinductive proteins and osteogenic cells during the resorption process. Cancellous

bone is commonly harvested from the iliac crest, as shown in Figure 2-3 (A: Posterior view of the pelvis. Strips of corticocancellous bone, as well as cancellous bone, can be harvested with the most posterior extent of the harvest being no closer than 4 cm from the posterior superior iliac spine. B: Corticocancellous strips consist of cancellous bone attached to a thin layer of cortical bone. C: Cancellous bone can be removed from between the inner and outer tables of the ilium and is best stored in a container where it can be kept moist) [32].

Autogenous cortical bone can be collected from the fibula, ribs and iliac crest. These grafts are mostly osteoconductive, but have little or no osteoinductive properties. Cortical grafts provide excellent structural support, which are good choice for segmental defects larger than 5 to 6 cm.

There are some disadvantages for using autogenous bone in bone repair. Harvesting autograft requires an additional surgery at the donor site, which can cause complications, such as inflammation, infection, and chronic pain. The amount of bone tissue that can be harvested is restricted, creating a supply problem. In one retrospective study (1950-1969), it was estimated that with 118 autografts taken from the iliac crest 6% had minor complaints such as harvest site pain, hypersensitivity, and buttocks anesthesia [33]. Younger and Chapman examined the medical records of 239 patients and found a higher morbidity at donor sites than seen previously. They noted an overall major complication rate of 8.6% and a minor complication rate of an additional 20.6% [34].

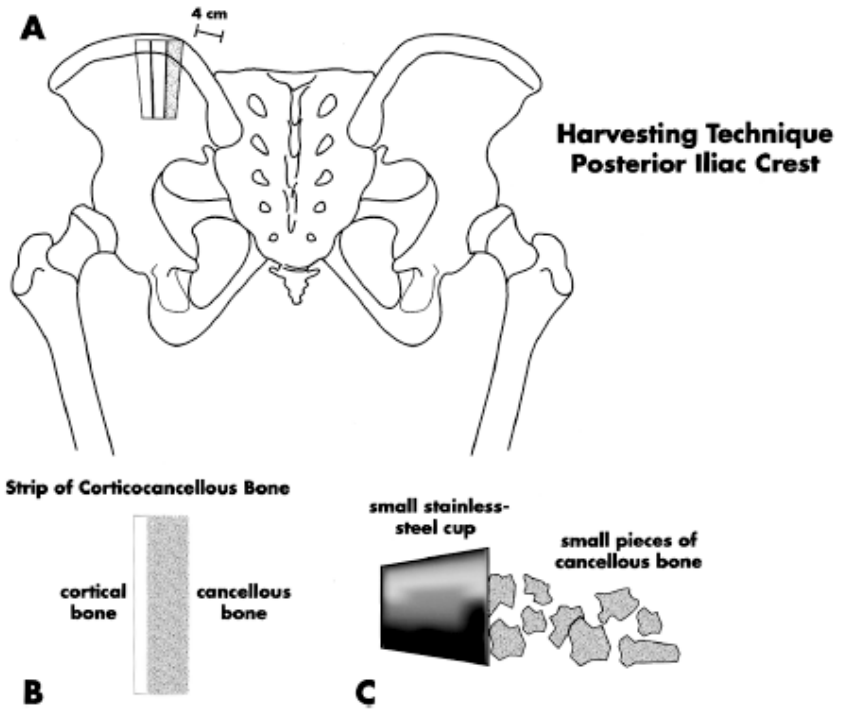

Figure 2-3. Illustration of harvesting cancellous bone from the iliac crest.

2.3 Allogeneic bone grafts

Allogenic bone has been used as the most common autograft extender or surrogate. It is used in 34% of all bone grafts performed in the United States [35]. Allogeneic bone, with variable biologic properties, is available in many forms: morselized and cancellous chips, corticocancellous and cortical grafts, and osteochondral and whole-bone segments.

Morselized and cancellous allografts are osteoconductive and provide some mechanical support, mainly in compression. Allografts are most often preserved by freeze-drying (lyophilization) and vacuum-packing, and undergo stages of incorporation

similar to those of autologous cancellous bone. Morselized allograft can be used for packing bone defects such as bone cysts after curettage or in periarticular metaphyseal locations to support elevated articular surfaces after articular depression such as occurs with tibial plateau or tibial pilon fractures. Morselized allograft is also useful to augment autogenous cancellous bone and to fill larger defects when the supply of autologous bone is limited.

Osteochondral and cortical allografts are available as whole-bone or joint segments (i.e., as the whole or part of the tibia, humerus, femur, talus, acetabulum, ilium, or hemipelvis) for limb salvage procedures or as cortical struts to buttress existing bone, to stabilize and reconstitute cortical bone after periprosthetic fractures, and to fill bone defects.

Advantages of allografts include the lack of procurement morbidity, the potential for immediate structural support, and a 60%-90% success rate in massive osseous restoration procedures. Shortcomings include the slower incorporation and less consistent clinical results compared with autografts. In addition, there are risks of disease transmission and immunogenic response. In a study of 1146 femoral heads considered suitable for bone-bank donation, unexpected disease was found in 8%, including 3 undiagnosed malignant bone tumors [36].

2.4 Xenografts

Xenogeneic bone grafts are bone from species other than human being. A number of xenograft products have been marketed, primarily composed of bovine bone. However,

these products have limited success. Generally, the organic component of xenograft bone is eliminated, rendering the materials non-immunogenic. Although partial deproteination and defatting of xenograft has been shown to decrease the antigenicity, this process also removes the osteoinductive proteins. Studies consistently demonstrate the lack of an osteogenic response, when xenograft is implanted into either hard or soft tissue sites. As a result, xenogeneic bone is generally not considered for use as a bone graft substitute.

2.5 Synthetic bone grafts

In the United States, usage of allograft and autograft is fairly equal. However, worldwide, the use of banked bone allograft is much lower than autograft. Current bone graft products in use globally is divided into approximately 45% autograft, 40% allograft, and 15% synthetic materials. The synthetic alternatives are playing an increasing important role. Available synthetic bone void fillers in the market can be categorized into ceramics, polymers and composites. Table 2-3 shows the most commonly used synthetic bone void fillers on the US market [37].

Synthetic ceramics provide an osteoconductive scaffold to which chemotatic, circulating proteins and cells can migrate and adhere, and within which progenitor cells can differentiate into functioning osteoblasts. Calcium phosphate based ceramics and cements have been widely used for bone substitution, augmentation and repair has gained clinical acceptance in many areas of orthopedics and dentistry. Among them, hydroxyapatite [$Ca_{10}(PO_4)_6(OH)_2$, HAP] and β-tricalcium phosphate [$Ca_3(PO_4)_2$, β-TCP]

are widely used in orthopedic applications. More information about hydroxyapatite and β-tricalcium phosphate will be described in Section 2.6.

Table 2-3. Most commonly used synthetic bone void fillers on the US market.

Product	Manufacturer	Composition	Forms
BonePlast	Interpore-Cross Intl.	Calcium sulfate	Injectable paste
BoneSource	Stryker	Calcium phosphate cement	Paste
Calceon 6	Synthes	Calcium sulfate	Pellets
Collagraft	Zimmer/NeuColl	HA/TCP Granules w/bovine collagen gel	Strips
Healos	Depuy Spine	Cross-linked bovine collagen with hydroxyapatite	Strips
Jax	Smith & Nephew	Calcium sulfate	Granules
OsteoSet	Wright Medical Inc.	Calcium sulfate	Pellets
PeoOsteon	Interpore-Cross Intl.	Coralline HA	Granules/blocks
TruGraft/ TruFit	OsteoBiologics, Inc.	Polylactide-co-glycolide, calcium sulfate, polyglycolide fibers and surfactant	Granules/plugs/ wedges/blocks
Vitoss	Orthovita	β-tricalcium phosphate	Granules/blocks
α-BSM	Depuy	Calcium phosphate cement	Injectable paste

Calcium phosphate bone cements are mixtures of various calcium phosphate powders, such as $CaHPO_4 \cdot 2H_2O$, $Ca_4(PO_4)_2O$, $CaHPO_4$, $Ca_8H_2(PO_4)_6 \cdot 5H_2O$, $Ca(H_2PO_4)_2 \cdot H_2O$, or $Ca_3(PO_4)_2$, with water or another liquid (e.g. H_3PO_4 or Na_2HPO_4 solution) [38]. The mixture transforms into HAP during setting, forming a porous body even at 37ºC [39-42]. The setting time of calcium phosphate cements can be only several minutes. The decay of the cements, when they come into contact with blood, can be prevented by adding sodium alginate [43]. Bone cements are easy to fill in bone defects in different morphology. Calcium phosphate cements can also be used as filling

of the teeth root canals or as drug-delivery systems. The disadvantage of calcium phosphate cements is their relatively poor mechanical strength [43, 44].

Bioactive glasses are hard solid (non-porous) materials, consisting of calcium, phosphate, and silicate (the main component). By varying the components, bioactive glasses can be produced from soluble to non-resorbable. Bioactive glasses are both osteoconductive and osteointegrative. A mechanically strong bond between the bioactive glass and bone forms eventually, through bone minerals created on the interface [45]. However, bioactive glasses are relatively brittle and prone to fracture with cyclic loading; they resist drilling and shaping. To improve the fracture toughness, stainless steel fibres and ceramic particles are incorporated into bioactive glasses [46].

Implants manufactured from resorbable polymers, such as copolymers of polylactic acid and polyglycolic acid (PLG), gelatin and collagen, have been used to promote bone repair in craniofacial applications [47-49], and as fixation devices, both in sports medicine and trauma procedures [50]. Abundant evidence shows these materials degrade during the healing process and are replaced with normal tissue. Three-dimensional porous scaffolds can be developed from biodegradable polymers. One technique uses salt leaching to create pores in the polymer substrate. Recent work [51] has demonstrated the ability of these matrices to support proliferation of osteoblasts and phenotypic expression in the scaffold.

Composite materials, especially composites from degradable polymers and calcium phosphates, have been widely studied, since human bone is mainly composed of collagen imbedded with biological apatites. The composite materials usually show improved mechanical and biological properties over their single component materials

when used for defect filling [52-55]. Composite materials can also work for delivery of bone morphogenetic proteins [56].

2.6 Calcium phosphates (CaPs)

CaPs differ in composition from each other, reflecting the differences in their origin (e.g. natural or synthetic) and methods of preparation, and can be prepared in different physical forms, e.g. dense, microporous and/or macroporous: particles or blocks. Table 2-4 shows various calcium phosphates with their respective Ca/P atomic ratios. The acronym of these calcium phosphates will be use in this thesis hereafter.

Table 2-4. Various calcium phosphates with their respective Ca/P atomic ratios.

Ca/P	Name	Formula	Acronym
2.0	Tetracalcium phosphate	$Ca_4O(PO_4)_2$	TTCP
1.67	Hydroxyapatite	$Ca_{10}(PO_4)_6(OH)_2$	HAP
1.67-1.50	Calcium-deficient HAP	$Ca_{10-x}(HPO_4)_x(PO_4)_{6-x}(OH)_{2-x}$	CDHAP
1.50	Apatitic tricalcium phosphate	$Ca_9(HPO_4)(PO_4)_5(OH)$	ATP
1.50	Tricalcium phosphate (α, β, γ)	$Ca_3(PO_4)_2$	TCP
1.33	Octacalcium phosphate	$Ca_8H_2(PO_4)_6{\cdot}5H_2O$	OCP
1.0	Dicalcium phosphate dihydrate	$CaHPO_4{\cdot}2H_2O$	DCPD
1.0	Dicalcium phosphate anhydrous	$CaHPO_4$	DCPA
1.0	Calcium pyrophosphate (α, β, γ)	$Ca_2P_2O_7$	CPP
1.0	Calcium pyrophosphate dihydrate	$Ca_2P_2O_7{\cdot}2H_2O$	CPPD
0.7	Heptacalcium phosphate	$Ca_7(P_5O_{16})_2$	HCP
0.67	Tetracalcium dihydrogen phosphate	$Ca_4H_2P_6O_{20}$	TDHP
0.5	Monocalcium phosphate monohydrate	$Ca(H_2PO_4)_2{\cdot}H_2O$	MCPM
0.5	Calcium metaphosphate (α, β, γ)	$Ca(PO_3)_2$	CMP

Monocalcium phosphate monohydrate (MCPM), Monocalcium phosphate anhydrous (MCPA): Crystallize from very acidic solutions only. The anhydrous form is formed at temperatures above 100ºC.

Dicalcium phosphate dihydrate (DCPD), Dicalcium phosphate anhydrous (DCPA): DCPD (brushite) has been proposed as an intermediate phase in precipitation reactions. It can be formed at pH 6 and 37ºC. DCPA is the anhydrous form of DCPD and is formed by drying DCPD or by precipitation from solutions above 60ºC.

Octacalcium phosphate (OCP): OCP has also been proposed as an intermediate reaction product in the precipitation of CaP from oversaturated solutions. It can be formed similar to DCPD but at somewhat lower pH.

Hydroxyapatite (HAP): Most stable CaP phase, end-product of precipitation reactions under physiological composition, pH, and temperature.

Tricalcium phosphate (TCP): TCP can not be directly obtained from aqueous solutions. It is somewhat more soluble than HAP, and is being used as a bioceramic, pure or mixed with HAP (biphasic calcium phosphate). Both α-TCP and β-TCP are high temperature phases, only formed above 800ºC.

Tetracalcium phosphate (TTCP): Can not be precipitated from calcium orthophosphate solutions. Pure phases have only limited biocompatibility.

Among them, hydroxyapatite [$Ca_{10}(PO_4)_6(OH)_2$, HAP] and β-tricalcium phosphate [$Ca_3(PO_4)_2$, β-TCP] are widely used in orthopedic applications. Both HAP and β-TCP are biocompatible and bioactive, which can directly form bonding to bony tissue. The combination (mixture) of HAP and β-TCP is called biphasic calcium phosphate (BCP).

2.6.1 Hydroxyapatite (HAP)

HAP is hexagonal with space group $P6_3/m$, with lattice parameters a = b= 9.4214 Å, c=6.8814 Å, α=β=90°, γ=120° [57]. The hexagonal structure is characterized by a six-

fold c-axis perpendicular to three equivalent a-axes at 120° angles to each other. Calcium cations (Ca^{2+}) and phosphate anions (PO_4^{3-}) are arranged around columns of monovalent hydroxyl anions (OH^-), which is shown as Figure 2-4 [58]. It is this network of phosphate groups that provides the skeletal framework and gives the structure its stability.

Hydroxyapatite has the formula of $Ca_{10}(PO_4)_6(OH)_2$ or $Ca_5(PO_4)_3(OH)$. Synonyms and abbreviations that have been given include: HAP, HAp, OHAp and HA. In this thesis, HAP will be used for abbreviation of hydroxyapatite.

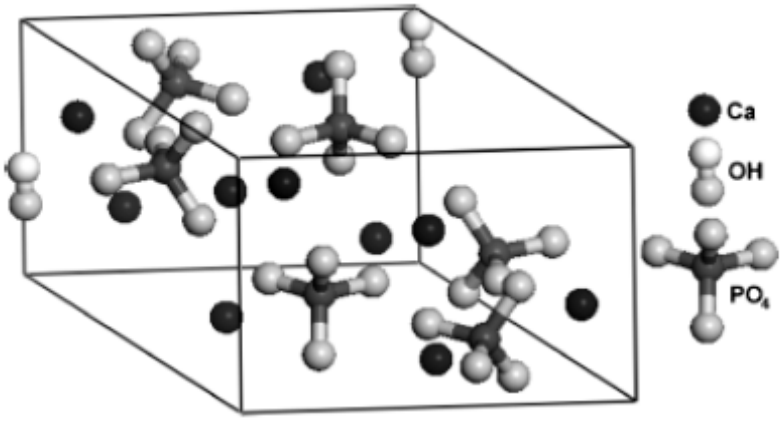

Figure 2-4. Crystal structure of hydroxyapatite.

Figure 2-5 shows hydroxyapatite structure projected down the c axis on to the basal plane. The a and b axes, intersecting at 120°, are perpendicular to the c axis. These three axes make up the unit cell volume, which contains the formula $Ca_{10}(PO_4)_6(OH)_2$. The numbers in the atoms are the c-axis (z) parameters. In the OH group, the O is at z = 0.20 or 0.30 and at z = 0.70 or 0.80; H is at z = 0.06 or 0.44 and at z = 0.56 or 0.94. The dashed and dotted lines outline the calcium triangles at z = 1/4 and z = 3/4, respectively [59].

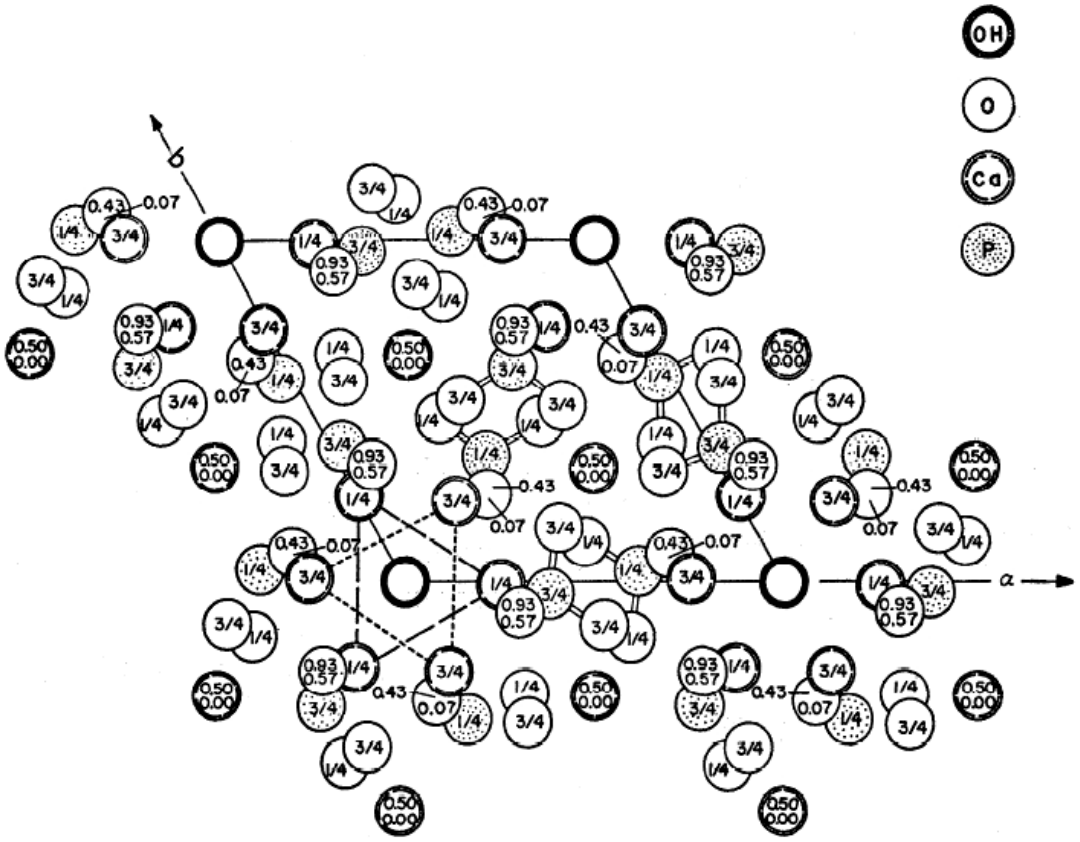

Figure 2-5. Hydroxyapatite structure projected down the c axis on to the basal plane.

HAP powders can be prepared by multiple techniques. Two main ways of preparing HAP powders are wet chemical reactions and solid-state reactions. Wet chemical reactions include precipitation [60-63], hydrothermal [64-68] and hydrolysis of other calcium phosphates [69, 70]. Depending on the techniques, materials with different morphology and level of crystallinity can be prepared. Solid-state reactions usually give a stoichiometric, highly-crystalline product with large particle size [71-73]. In our experiments (Chapter 5), HAP rods were prepared by hydrothermal reaction with a nucleation-growth mechanism. In addition, HAP particles with good crystallinity were prepared through precipitation followed by low-temperature hydrothermal treatment.

2.6.2 Beta-tricalcium phosphate (β-TCP)

Beta-TCP [$Ca_3(PO_4)_2$] has the rhombohedral space group $R\bar{3}c$ with unit cell a=10.439 Å, c=37.375 Å with 21 formula units per hexagonal unit cell [74] and room temperature density is 3.07 g·cm^{-3}. Atoms in the β-TCP structure are arranged in A and B columns shown as in Figure 2-6 [28]. There are three A and nine B columns in β-TCP and its derivatives (Figure 2-7 and Figure 2-6) [28].

The important derivatives of β-TCP is magnesium-substituted tricalicum phosphate [β-TCMP, $(Ca_xMg_{1-x})_3(PO_4)_2$)]. It is possible to replace up to about 15% of the Ca^{2+} by Mg^{2+} ions without changing the β-TCP structure [75, 76]. The $Ca^{2+}$are not randomly replaced by Mg^{2+} ions. Two sites, Ca(4) and Ca(5) as shown in Figure 2-7, are favored to be occupied by smaller Mg^{2+} ions. The Ca(5) site is most readily occupied, which has octahedral coordination, uncomfortably constrained for a Ca^{2+}ion, but suitable for smaller Mg^{2+} ion. The ionic contents of β-TCP and β-TCMP in one third of the hexagonal unit cell are shown in Table 2-5 (□ indicates unoccupied site).

β-TCP can be prepared by heating a mixture of the calculated quantity of DCPA and $CaCO_3$ [77]. After heating the mixture at 1000ºC for several hours, the reaction to produce β-TCP can be completed. Another method used to prepare β-TCP and β-TCMP is performed with two steps [78, 79]. The precursor, apatitic tricalcium phosphate [$Ca_9(HPO_4)(PO_4)_5(OH)$], is first prepared by wet precipitation from calcium and phosphate solutions. The precursor is then heated at 800ºC for 3 hours to produce β-TCP. Both methods will be used and described with details in Chapter 6.

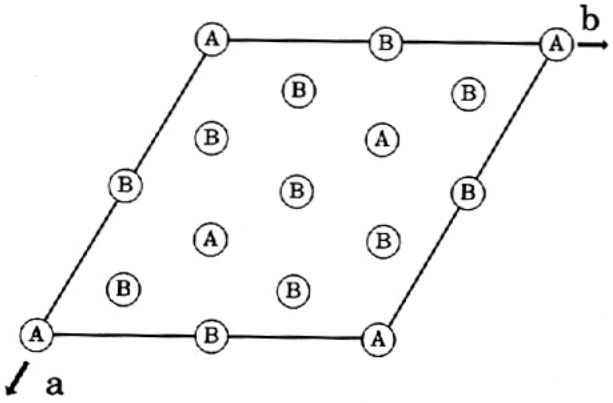

Figure 2-6. Arrangement of A and B columns in the hexagonal unit cell of β-TCP and its derivatives. The c-axis is out of the plane.

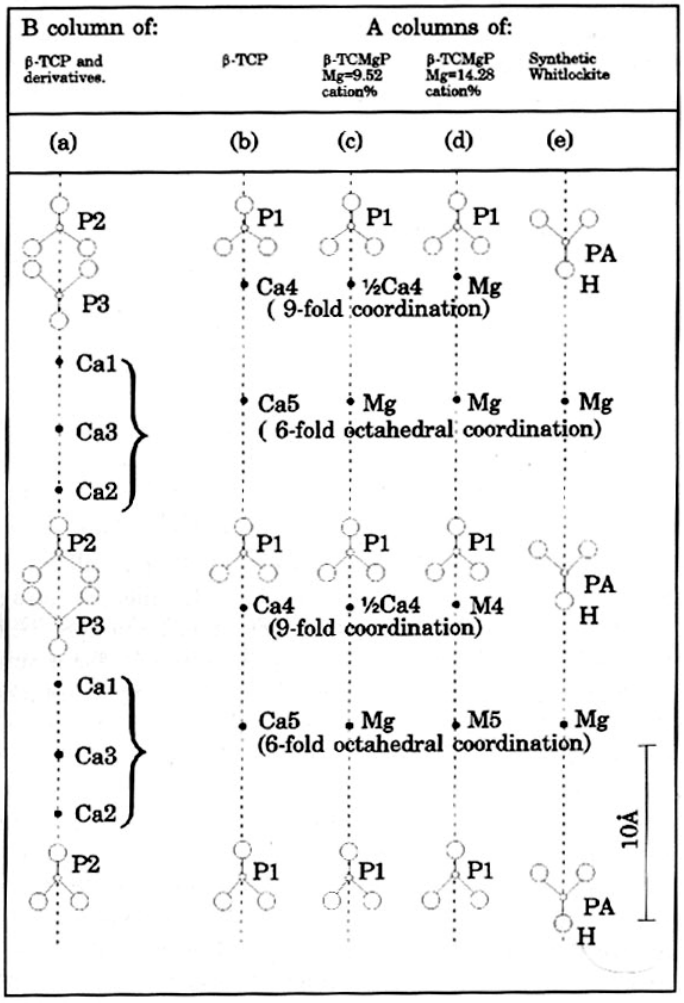

Figure 2-7. Configuration of A and B columns (length shown is c-axis parameter of the hexagonal unit cell plus an additional PO_4 to show continuity of the columns).

Table 2-5. Ionic contents of β-TCP and β-TCMP in one third of the hexagonal unit cell.

Compound	Ion contents			
	Site	Ca(5)	Ca(4)	PO_4
β-TCP, $Ca_3(PO_4)_2$	Ca_{18}	Ca_2	(Ca, □)	PO_4
β-TCMP, Mg 9.52%	Ca_{18}	Mg_2	(Ca, □)	PO_4
β-TCMP, Mg 14.28%	Ca_{18}	Mg_2	(Mg, □)	PO_4

2.6.3 Biphasic calcium phosphate

HAP products are poorly resorbable, which retain for years after the implantation. β-TCP has much faster resorption rate. β-TCP products can be absorbed in ~3-6 months after the implantation. To control the resorption rate, biphasic calcium phosphates (BCP), which consist of HAP and β-TCP combined, have been investigated. The resorption rate of BCP depends on the molar ratio of β-TCP/HAP in the mixture. The higher the ratio, the faster the resorption.

Figure 2-8 shows the equilibrium phase diagram of different calcium phosphates [80]. The shaded region shows the area of BCP formation. BCP can be prepared by mechanical mixing of HAP and β-TCP or from a precipitation method [81]. Solid-state reaction [82], microwave processing [80] and heating bovine cancellous bone with the addition of $(NH_4)_2HPO_4$ [83] were also reported to prepare BCP.

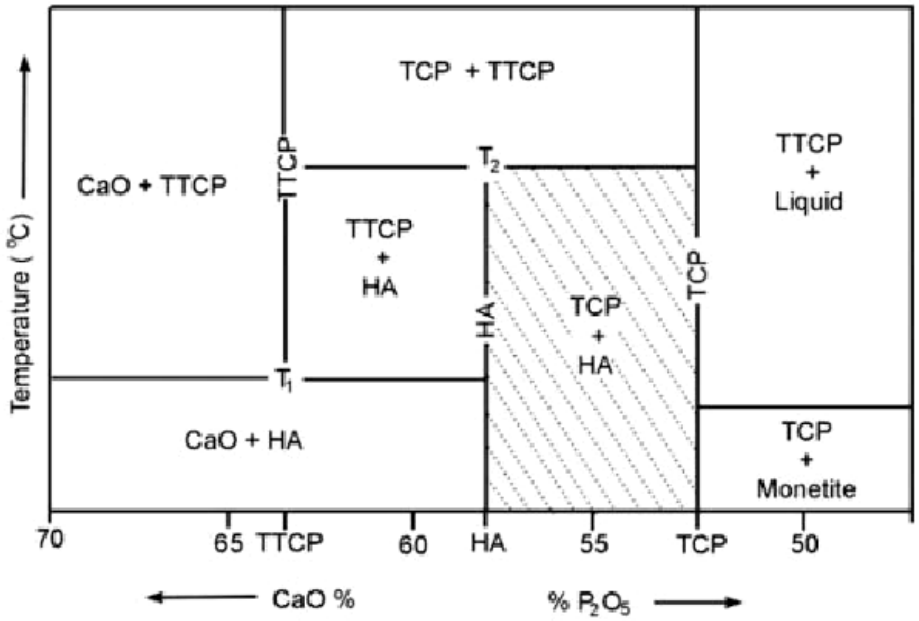

Figure 2-8. Equilibrium phase diagram of different calcium phosphates. The shaded region shows the phases of interest for BCP formation (T1=1360℃ and T2=1475℃).

2.7 Research outline

Calcium phosphate ceramics have been used in orthopaedics and dentistry since the 1980s. HAP has a stoichiometry similar to bone mineral, whereas TCP has a stoichiometry similar to amorphous bone precursor. Both HAP and TCP ceramics are highly biocompatible. They differ in the biologic response at the host site. Porous TCP ceramics is resorbable after implantation, while HAP is more permanent. Microstructures of HAP and TCP ceramics are essential when the implant is intended to function as scaffolds.

Dense ceramics have high mechanical strength, which can be used as scaffolds in some load-bearing cases, but don't facilitate new bone formation. Porous scaffolds

provide greater surface area for vascularization, and bone in-growth. The rate and quality of bone integration to the porous implants are believed to be dependent on pore size, porosity volume fraction, interconnection size, and interconnection density. However, many porous ceramics are too brittle, which don't have mechanical strength required for practical surgery. In this thesis research, HAP, β-TCP and β-TCMP ceramics with tailored structures were produced, considering the functions of structural permeability and mechanics when used as bone substitutes.

Well-crytalline HAP powders (Chapter 5) were also synthesized, which can be used to prepare HAP and BCP ceramics in future. Large HAP rods synthesized in Chapter 5 have potential applications for protein purification in liquid chromatography and can also be used to increase the fracture toughness of HAP ceramics.

2.7.1 Dense HAP ceramics

Dense HAP ceramics have better mechanical performance than porous ceramics, thereby making it a desirable substitute for some load-bearing cases. Traditionally, dense HAP has been made by sintering HAP powders at high temperature. However, formation of dense HAP is controlled by many factors, such as Ca/P molar ratio, sintering temperature and so on [27]. Development of new methods to produce dense HAP with high mechanical strength at relative low temperatures is valuable from the perspective of costs and effectiveness.

The mollusc shells are microlaminate composite of mineral and biopolymers, and exhibit exceptional nanoscale regularity and a strength ~3000 times greater than the

mineral crystals themselves [84-86]. Among these, the giant clam (Tridacna gigas) and conch (Strombus gigas) have mechanical properties, such as compressive strength and modulus similar to natural bone [87]. In Section 4.1, *Strombus gigas* (conch) shell and *Tridacna gigas* (Giant clam) shell were converted to dense HAP through hydrothermal reaction at relative low temperatures. Experimental factors, such as solution concentration, reaction temperature and duration, were controlled to tailor the dense HAP layers on the shell. The micro- and meso-structures of the original and converted shells are studied in this section, as well as the mechanical and biological properties of converted shell samples. Partially converted shell samples have good biocompatibility and bioactivity from HAP layers outside, and high mechanical strength with dense lamellar shell structures inside, when used as bone implants.

2.7.2 Porous HAP ceramics

Porous HAP ceramics have been widely applied as bone substitute. Porous HAP exhibits strong bonding to the bone, and provide a mechanical interlock leading to a firmer fixation of the material. To fabricate porous HAP ceramics (pore size of 100–600 μm), HAP powder is usually sintering with appropriate pore-creating additives (for example paraffin, naphthalene, or hydrogen peroxide) which evolve gases at elevated temperatures [27]. Several low-temperature methods have also been applied to fabricate porous HAP. HAP can also be cast into the $CaCO_3$ skeleton, which is then dissolved, leaving a porous network [88]. Natural porous materials, like coral skeletons made of $CaCO_3$, can be converted into HAP under hydrothermal conditions [89].

Coral and cuttlebone are mainly composed of aragonite phases with a small amount

of organic materials. Both coral and cuttlebone have three-dimensional macroporous structures (pore size >50 μm). In Section 4.3, coral and cuttlebone were converted to HAP, while maintaining original porous structures. The interconnected macroporous structures of HAP products would allow good supply of blood and nutrients from the surrounding environment after the implantation. Macroporous HAP scaffolds support infiltration of bone cells and vessels, and finally encourage new bone ingrowth. Microstructures of original and converted coral and cuttlebone, and the conversion mechanisms were studied.

2.7.3 Dense β-TCP and β-TCMP ceramics

Highly dense β-TCP ceramics is hard to prepare, due to insufficient compaction when sintering below the β- to α-TCP transition temperature [90, 91]. Above the transition temperature (~1125℃), β- to α-TCP transformation causes the expansion of TCP during the sintering process and creates micro-cracks in the ceramics, which prevents TCP ceramics from further densification [92, 93]. Previous results indicate that the presence of Mg can stabilize the β-TCP structure [28, 94]. With the increase of Mg^{2+} content in β-TCP structure, β- to α-TCP transition temperature increases [76]. Highly dense Mg-substituted tricalcium phosphate (β-TCMP) ceramics could be prepared by sintering green bodies at temperatures above 1125℃ without phase transformation.

In Section 6.1, β-TCP powders with/without Mg^{2+} substitution were produced. The effects of Mg^{2+} substitution to the crystal lattice contraction, and β- to α-TCP transition

temperature were investigated. Dense β-TCP and β-TCMP ceramics can be produced by pressing ceramic green bodies at high pressure (e.g. 100 MPa) and further sintering at 1100℃ for 2 hours. Extremly dense β-TCMP ceramics were prepared by sintering β-TCMP (3 mol% Mg^{2+}) at 1250℃ for 2 hours. Mechanical strength of dense β-TCP and β-TCMP ceramics were investigated. The microstrcutures of original ceramic samples and fracture surfaces were observed, and fracture mechanism is studied.

2.7.4 Porous β-TCMP ceramics

Porous β-TCP ceramics may be ideally suitable as scaffolds for bone defects filling, which have osteoconductivity for vascular infiltration and bone in-growth, and resorbability for eventual replacement by natural bone. Natural porous calcium carbonate skeletons, coral and cuttlebone, which are mainly composed of aragonite phase, were both hydrothermally converted to poor resorbable HAP. However, sea urchin spines mainly consist of large single crystals of Mg-rich calcite [$(Ca,Mg)CO_3$] with interconnected porous structures [89]. In Section 4.2, sea urchin spines were hydrothermally converted to resorbable β-TCMP, rather than HAP, while maintaining original porous structures. Evaluation of the suitability of these converted spines for bio-implant materials was then evaluated in terms of their mechanical properties as well as their biocompatibility via *in-vivo* testing.

Porous β-TCMP products from urchin spines have relative small pores (~20-50 μm), which can't rapidly facilitate vescular infiltration and in-growth of new bone. Macroporous β-TCMP ceramics (pore size > 50 μm) with micropores in the struts were

prepared both by the extrusion method with sucrose as a porogen, and the replication method using polyurethane foams (Section 6.2).

2.7.5 Bone-mimicking ceramics

Interconnected macroporous β-TCP ceramics are preferred to be used as bone defect filler, considering the ability for infiltration of bone cells and vessels into the scaffold. However, most macroporous β-TCP ceramics are too brittle to work as temporary scaffolds in implant surgery. Dense β-TCMP ceramics have the strength, which meet the mechanical requirement, but their dense structures don't facilitate new bone ingrowth. Therefore, the combination of dense and porous structure, mimicking human bone, is necessary to meet both permeability and mechanical requirements.

In Section 6.3, resorbable β-TCMP ceramics with porous structures in the center surrounded by dense shell-like structures were created. The outside dense structures give the strength to scaffold, which can then be used in load-bearing cases. The central porous structures enable infiltration of bone cells and vessels, and finally ingrowth of new bone.

3 EXPERIMENTAL TECHNIQUES

3.1 Synthesis

3.1.1 Hydrothermal reactions

Hydrothermal synthesis of HAP rods and hydrothermal conversion of marine skeletons to calcium phosphates were performed either in lab-made autoclaves (Figure 3-1a, temp. up to 250ºC) or Parr benchtop reactor 4843 (Figure 3-1b, temp. up to 350ºC).

(a)  (b) 

Figure 3-1. Hydrothermal reactors: autoclaves (a) and Parr reactor 4843 (b).

Small pieces of samples were cut from marine skeletons, e.g. seashells, sea urchin spines, coral and cuttlebone, cleaned with deionized water and placed in an autoclave or Parr reactor 4843 filled with a specified concentration of $(NH_4)_2HPO_4$ solution. The

autoclave or Parr reactor was then sealed and heated at different temperatures for different durations. Conch shell and urchin spines can also be machined or fashioned into particular shapes, e.g. screws, for different individual implants.

The hydrothermal conversion of calcium carbonate marine skeletons in $(NH_4)_2HPO_4$ solution to produce HAP (Section 4.1 and 4.3), took place as the following reaction Equation (1) [95, 96]:

(1) $10CaCO_3+6(NH_4)_2HPO_4+2H_2O \rightarrow Ca_{10}(PO_4)_6(OH)_2+6(NH_4)_2CO_3+4H_2CO_3$

The hydrothermal conversion of urchin spine skeletons in $(NH_4)_2HPO_4$ solution to produce β-TCMP (Section 4.2), follows the ion-exchange reaction (2) given below [89]:

(2) $3(Ca,Mg)CO_3+2(NH_4)_2HPO_4 \rightarrow (Ca,Mg)_3(PO_4)_2+2(NH_4)_2CO_3+H_2CO_3$

Synthesis of HAP rods by hydrothermal reaction between DCPA and CaCO3 took place as the following Equation (3) (Section 5.1). The byproduct β-TCP was produced as Equation (4).

(3) $6CaHPO_4 + 4CaCO_3 + 2H_2O \rightarrow Ca_{10}(PO_4)_6(OH)_2 + 4H_2CO_3$

(4) $2CaHPO_4 + CaCO_3 \rightarrow \beta\text{-}Ca_3(PO_4)_2 + H_2CO_3$

3.1.2 Wet precipitation

Wet precipitation was used to prepare HAP (Section 5.2), shown as Equation (5).

(5) $6(NH_4)_2HPO_4+10Ca(NO_3)_2+8NH_4OH \rightarrow Ca_{10}(PO_4)_6(OH)_2+20NH_4NO_3+6H_2O$

Figure 3-2 shows the precipitation experiment from $(NH_4)_2HPO_4$ solution and $Ca(NO_3)_2$ solution by an auto-titration equipment; $(NH_4)_2HPO_4$ solution was titrated into a $Ca(NO_3)_2$ solution. The pH value of the mixture was adjusted to around 9 with NH_4OH solution, and the temperature is controlled by a water bath.

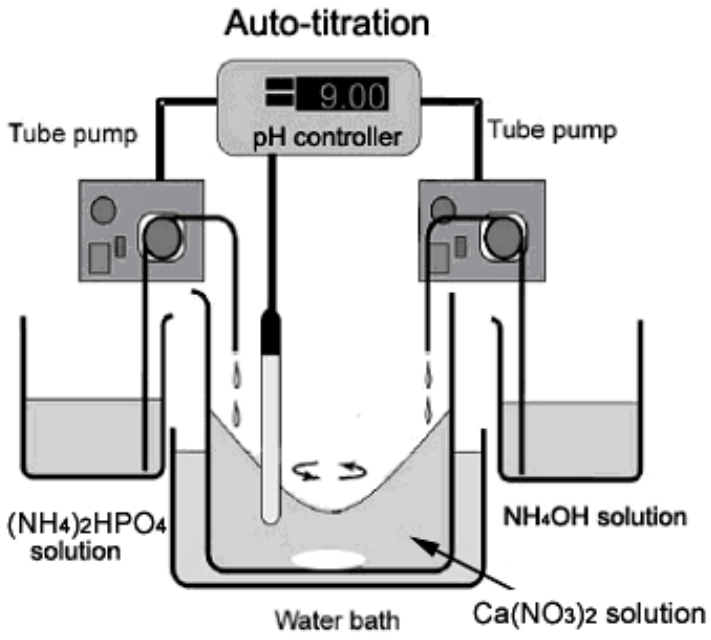

Figure 3-2. Schematic drawing of auto-titration used for wet precipitation.

β-TCP precursor $[Ca_9(HPO_4)(PO_4)_5(OH)]$ powders (Section 6.1) can be prepared by wet precipitation shown as Equation (6). The precursor was then heated at 800 ºC for 3 hours to produce β-TCP, indicated by Equation (7).

(6) $9Ca(NO_3)_2 + 6(NH_4)_2HPO_4 + 6NH_4OH \rightarrow Ca_9(HPO_4)(PO_4)_5(OH) + 5H_2O + 18NH_4NO_3$

(7) $Ca_9(HPO_4)(PO_4)_5(OH) \rightarrow 3Ca_3(PO_4)_2 + H_2O$

For synthesis of β-TCMP precursor [$(Ca_{1-x}Mg_x)_9(HPO_4)(PO_4)_5(OH)$] and β-TCMP, reactions took place as Equations (8) and (9).

(8) $(9-9x)Ca(NO_3)_2+(9x)Mg(NO_3)_2+6(NH_4)_2HPO_4+6NH_4OH \rightarrow$

$$(Ca_{1-x}Mg_x)_9(HPO_4)(PO_4)_5(OH) +18NH_4NO_3+5H_2O$$

(9) $(Ca_{1-x}Mg_x)_9(HPO_4)(PO_4)_5(OH) \rightarrow 3(Ca_{1-x}Mg_x)_3(PO_4)_2+H_2O$

3.1.3 Solid-state reactions

β-TCP and β-TCMP samples were prepared from solid-state reactions (Section 6.2.1). $CaHPO_4$, $CaCO_3$ powders with/without MgO were mixed thoroughly in a mortar. The mixture was then calcined in air at high temperatures in a programmable muffle furnace (Lindberg 1700 ºC Box Furnace). Equation (10) and (11) show the whole reactions. Both reactions were completed at 1000 ºC for 6 hours.

(10) $2CaHPO_4+ CaCO_3 \rightarrow \beta\text{-}Ca_3(PO_4)_2+H_2O+CO_2$

(11) $(1-x)\ CaCO_3+xMgO+2CaHPO_4 \rightarrow (Ca_{3-x}Mg_x)(PO_4)_2+H_2O+(1-x)CO_2$

3.2 Mechanical tests

Quasi-static compression tests were conducted on a servohydraulic test frame (Instron 8501) at a strain rate of 10^{-3}/s. Partially converted shells, with HAP layers on the surface and shell structures inside, were cut into samples about 5mm × 4mm × 3mm, and tested as shown schematically in Figure 3-3. The original spines and converted

spines were cut into cylindrical samples ~10 mm (diameter) × 6 mm (long), and tested as shown in Figure 3-4 with loading parallel to c-axis of the spine. For quasi-static compression of dense β-TCP and β-TCMP ceramics, 10-15 cylindrical specimens [~11.0mm (diameter) × 4.5mm (height)] were tested.

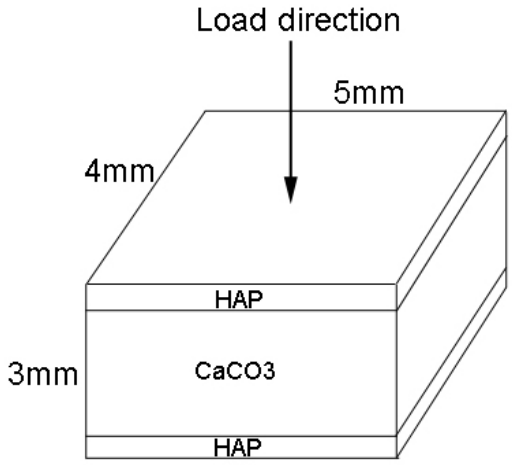

Figure 3-3. Schematic drawing of the compression test of partially converted seashell samples.

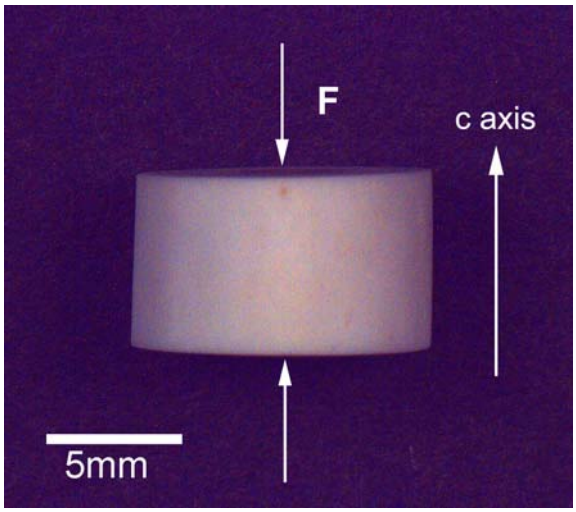

Figure 3-4. Schematic drawing of the compression test of urchin spines or converted spine samples.

3.3 In vivo tests

3.3.1 Surgical procedure

For *in-vivo* tests, 15 rats (5 each for converted clam, conch or spine samples) were induced with isoflurane (3%) in an induction box and weighed. Buprenex (0.02 mg/kg SC) and ketamine (100 mg/kg) were then given by IM injection, which served to provide both intraoperative analgesia and recovery pain control. General anesthesia was then employed via mask (Isoflurane 1-1.5%) and the animal prepped for surgery. An incision was made in the lateral aspect of the distal femur, bilaterally. The lateral aspect of the distal femur was exposed and a 2.0 mm drill was used to introduce a 2 × 3 mm cylindrical defect into and across the distal femurs (axial plane) just above the femoral condyles and growth plate. A 2.0 mm converted shell or spine cylindrical implant was inserted into the defect, laterally. One leg defect was left empty as an untreated control. The muscles were repositioned and sutured, then the wound was closed in a routine manner. The animals recovered and returned to their cages with appropriate postoperative analgesics.

3.3.2 Micro-CT imaging

The eXplore RS micro-CT scanner (GE Medical Systems, London, Ontario) was used for high resolution, *in-vivo*, three-dimensional femur imaging. Whole-body rats may be imaged at isotropic resolutions as low as 27 microns. While under general anesthesia with 1-3% isoflurane, the rats were placed in the scanner following surgery to document placement of the implant. The eXplore RS system includes Windows

based software applications for image acquisition, reconstruction, visualization and data analysis. The distal femurs of all rats in the study were evaluated at the conclusion of the study at 6 weeks for evidence of implant loosening or a halo ring around the implant.

All surgical and micro-CT scanning procedures were performed according to ACORP approved protocols under the direction of the Institutional Animal Care and Use Committee of the VA Medical Center, San Diego, CA.

3.3.3 Hard tissue histology

The femurs were removed en bloc and fixed in 10% buffered formalin followed by dehydration in ethanol, then carefully embedded in methylmethacrylate resin to insure full embedding of the tissue. After curing, the specimens were cut and milled into approximately 50-75 micron sagittal sections and stained with a Sanderson Rapid bone stain and counter stained using Acid Fuchsin.

3.4 Characterization

3.4.1 X-ray diffraction

Sample phases were identified by powder x-ray diffraction (XRD). A Rigaku Rotaflex X-ray diffractometer using CuKα radiation (λ=1.5418Å) was employed. The diffractometer was operated at 40kV and 100mA at a 2θ range of 20-60° with a step size of 0.02° or 0.04°. Phases were indentified with MDI Jade7 software (Materials Data, Inc.) by the ‘search-match’ function. For example, HAP phase was matched with

JCPDF #9-0432, and β-TCP phase was matched with JCPDF #9-0169. Lattice parameters of each phase can also be calculated by Jade7 (Section 6.1.2).

3.4.2 Optical microscopy

Microstructures of polished seashells were observed by optical microscope (Olympus GX51) with image processing functions. Converted seashell samples were mounted with the mixture of Epofix resin and hardener (EPOES, Struers) in the volume ratio of 15:2 overnight. The samples were then polished until final polishing with silicon carbide paper, US grit 1200. Optical images were processed with Pax-it software (Version 6, MIS Inc.) to measure the thickness of HAP layers on the shell samples.

3.4.3 Electron microscopy

The morphology and structures of samples were studied by scanning electron microscopy (SEM) using a Phillips XL20. The elemental compositions of the products were qualitatively identified by energy dispersive x-ray spectrometer (EDS) in the SEM. EDS mapping were performed for the tissue samples (converted clam, conch or spine implants) after 6 weeks implantation. For EDS mapping, the tissue samples were mounted in epoxy, polished, and then coated with carbon for elemental mapping.

The morphology and structures of some samples were also studied by transmission electron microscopy (TEM) using a Phillips EM420.

3.4.4 FTIR analysis

Transmission infrared spectroscopy was performed by the KBr pellet method, using a Fourier transmission infrared spectrometer (FT-IR, Nicolet 550) to determine the various functional groups in the samples. The specimen powder was ground in an agate mortar and thoroughly mixed with spectroscopic grade KBr. Transparent pellets were prepared in a stainless steel die. FTIR spectra were collected in the 4000-400cm^{-1} wavenumber range.

3.4.5 Thermal analysis

Differential thermal analysis (DTA) and Thermogravimetric analysis (TG) were employed to determine the phase stability and the reaction temperatures using a Pyris Diamond TG/DTA (PerkinElmer Instruments). For example, β-TCP powder was heated in air with a heating rate of 5℃/min to 1000℃ and 2℃/min from 1000-1300℃ to detect β- to α-TCP transition temperature (Section 6.1.2).

4 HYDROTHERMAL CONVERSION OF MARINE SKELETONS TO CALCIUM PHOSPHATES

Marine $CaCO_3$ skeletons have hierarchical and optimally designed architectures created by nature. For example, some seashells have the lamellar structures, which give them high mechanical strength and toughness. Coral and cuttlebone have interconnected porous structures with pore size above 100μm, which is suitable as an implant material for infiltration of bone cells and vessels. Sea urchin spines also have three-dimensional interconnected porous structures, with a relatively small pore size, 20-50μm. In our experiments, these $CaCO_3$ skeletons were converted to hydroxyapatite or β-tricalcium phosphate by hydrothermal reactions in $(NH_4)_2HPO_4$ solution. Seashells, coral and cuttlebone were converted to hydroxyapatite [HAP, $Ca_{10}(PO_4)_6(OH)_2$], and sea urchin spines were converted to Mg–substituted tricalcium phosphate [β-TCMP, $(Ca,Mg)_3(PO_4)_2$], while maintaining their original structures. After implantation of converted shell and spine samples in rat femoral defects for 6 weeks, there was new bone growth up to and around the implants. These results show good bioactivity and osteoconductivity of the implants, indicating the converted shell and spine samples can be used as bone defect filler.

4.1 Conversion of seashells to dense hydroxyaptite

The invertebrate phylum known as mollusca includes marine classes such as gastropoda and bivalvia that have external calcareous shells of sufficient mass and size

to be considered for human biomedical structural implants. The mollusc shells are microlaminate composite of mineral and biopolymers, typically consisting of 95-99% $CaCO_3$ by weight and 1-5% organic macromolecules [84], and exhibit exceptional nanoscale regularity and a strength ~3000 times greater than the mineral crystals themselves [84-86]. Among these, the giant clam (Tridacna gigas) and conch (Strombus gigas) have mechanical properties, such as compressive strength and modulus similar to natural bone [87]. In the case of Tridacna gigas, the giant clamshell can weight more than 180 kilograms, measure 1.5 meters across, and can have shell wall thickness in excess of 8 centimeters. The compressive strength of the native Tridacna gigas shell can range between ~50 MPa and 200 MPa, depending on the defect structures present in the shell [87]. For the case of Strombus gigas, the conch shells can grow up to ~30 centimeters in length, weighting a few kilograms, and having shell wall thickness approaching 1 centimeter. The compressive strength of the native Strombus gigas shell can range between ~140 MPa and 300 MPa [87]. In addition to the excellent mechanical properties, a few studies have also shown that nacre is biocompatible and osteoinductive, and can initiate bone formation both *in-vivo* and *in-vitro* [95-98]. Recently, hydrothermal conversions of calcium carbonate skeletons (e.g. coral, cuttlebone, sea urchin spine and seashells) to calcium phosphate bioceramics have been actively studied [89, 99-103].

In this investigation, *Strombus gigas* (conch) shell and *Tridacna gigas* (Giant clam) shell were converted to HAP through hydrothermal reaction. Dense HAP structures were created from these shells throughout the majority of the samples at relative low temperature. Results from *in-vivo* tests in rat femoral defects for 6 weeks indicate good

biocompatibility and bioactivity of these converted shell samples. The micro- and meso-structures of the original and converted shells are presented here, as well as the mechanical and biological properties of converted shell samples.

4.1.1 Materials and Methods

The starting materials in the experiment were diammonium hydrogen phosphate [$(NH_4)_2HPO_4$, Fisher Scientific], *Strombus gigas* (conch) shell (Figure 4-1a) and *Tridacna gigas* (Giant clam) shell (Figure 4-1b). These shells were cut into small pieces (Figure 4-1c), about 28 mm × 20 mm × 3 mm, cleaned with deionized water and placed in an autoclave filled with a specified concentration of $(NH_4)_2HPO_4$ solution. The autoclave was then sealed and heated at different temperatures for different durations. The shells can also be machined or fashioned into particular shapes for different individual implants. Figure 4-1d shows conch and clamshell pieces machined into threaded rod segments, demonstrating the feasibility of fabricating implant devices from these materials.

In these experiments, the starting concentration of $(NH_4)_2HPO_4$ solution ranged from 0.12 g/ml to 0.6 g/ml, and temperatures from 180ºC to 240ºC. For the optimum conversion, the starting $(NH_4)_2HPO_4$ solution was 0.2 g/ml and temperature was 180ºC, replenishing the $(NH_4)_2HPO_4$ solution within the autoclave every 2 days.

The hydrothermal conversion reaction took place as the following reaction Equation (1) [95, 96]:

(1) $10CaCO_3+6(NH_4)_2HPO_4+2H_2O \rightarrow Ca_{10}(PO_4)_6(OH)_2+6(NH_4)_2CO_3+4H_2CO_3$

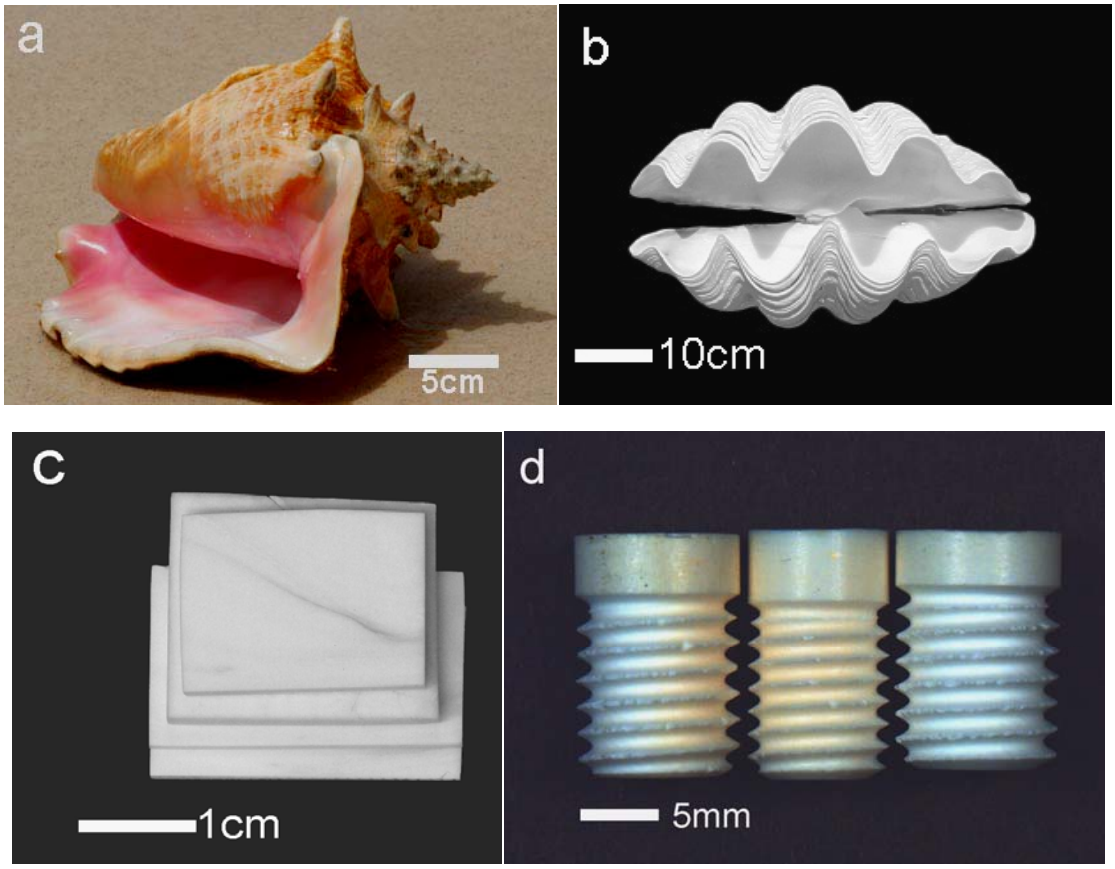

Figure 4-1. Optical images of seashells: (a) conch shell, (b) clamshell, (c) shell samples for hydrothermal conversion and (d) machined screw-shape shells.

For mechanical tests, the shells were converted in a separate hydrothermal process. Seven pieces of conch shells and seven pieces of clam shells ~3 mm thick and ~25 mm square were placed together with 250 ml of 0.16 g/ml $(NH_4)_2HPO_4$ solution in an autoclave. The autoclaved was then sealed and heated at 180ºC. The $(NH_4)_2HPO_4$ solution was refreshed every 2 days. Pieces of conch and clam were collected from the autoclave after 2, 4, 6, 8, 12, 16 and 20 days. Partially converted shells (conch/clam), with HAP layers on the surface and shell structures inside, were cut into samples about 5mm × 4mm × 3mm, and tested as shown schematically in Figure 3-3. Quasi-static

compression tests of these samples were conducted on a servohydraulic test frame at a strain rate of 2×10^{-3}/s.

For *in-vivo* test, 10 rats in total (five designated for the converted conch implants and five for the converted clam implants) were used. Procedures for surgery, micro-CT imaging and histology study follow Section 3.3.1, 3.3.2 and 3.3.3.

4.1.2 Results and discussion

Figure 4-2 shows examples of the microstructures of both the original conch shell and the original clamshell. The boundaries visible in (a) are the first order lamella in two different variant directions. The vertical boundaries visible in (b) are the columnar grain boundaries, while the horizontal, wavy, semi-parallel boundaries are growth bands.

The conch shell structure consists of first-order lamella visible in Figure 4-2a, with second and third order lamella of finer scale, not visible in this image. The giant clamshell structure consists of large columnar grains, which grow parallel to the shell wall thickness direction, and fine-scale horizontal, wavy, semi-parallel growth bands.

Powder XRD patterns of the original conch shells and the conch shell samples hydrothermally converted at 180ºC and 200ºC are shown in Figure 4-3. Figure 4-4 shows powder XRD patterns of the original clamshell and the clamshell hydrothermally converted at 180ºC and 200ºC in the autoclave. The original conch and clamshells are mainly composed of aragonite crystals (Figure 4-3 curve ‘a’ and Figure 4-4 curve ‘a’) with the organic matrix. A small amount of calcite crystals was found in some shell samples. After 10 days conversion at 180ºC, the conch and clamshells were almost entirely converted to HAP. A small amount of aragonite crystals remained, and some

aragonite crystals transformed into calcite (Figure 4-3 curve ‘b’ and Figure 4-4 curve ‘b’). The conch and clamshells were completely converted to HAP at 200ºC for 10 days (Figure 4-3 curve ‘c’ and Figure 4-4 curve ‘c’).

(a)

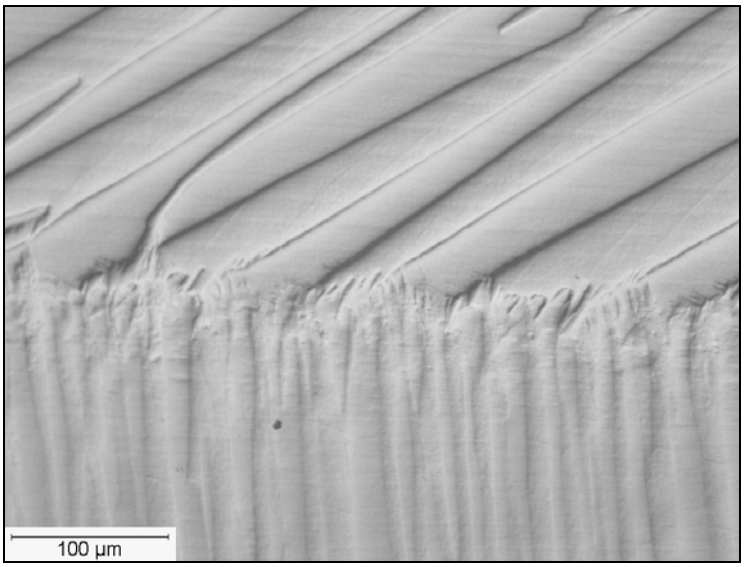

(b)

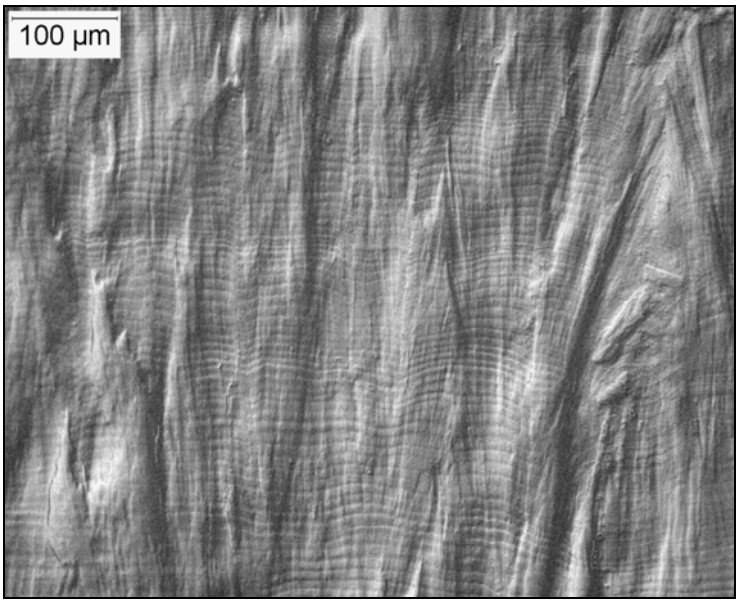

Figure 4-2. Optical micrographs of (a) original conch shell structure, and (b) original giant clamshell.

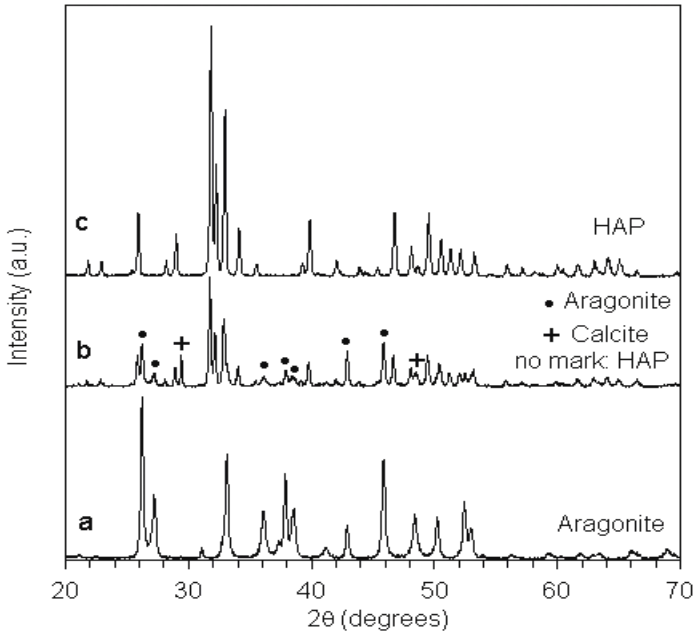

Figure 4-3. Powder XRD pattern of (a) conch shell, (b) conch converted at 180ºC for 10 days and (c) at 200ºC for 10 days.

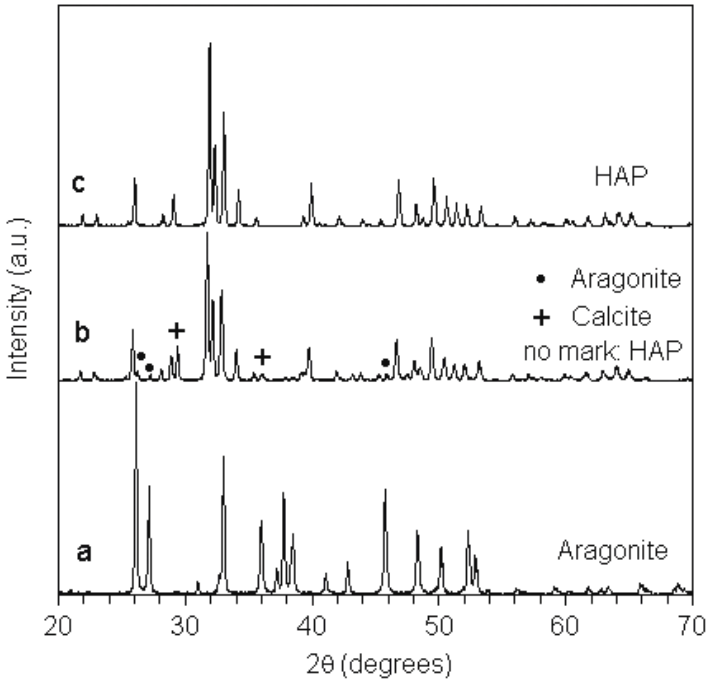

Figure 4-4. Powder XRD pattern of (a) clam shell, (b) clam converted at 180ºC for 10 days and (c) at 200ºC for 10 days.

Figure 4-5 shows FT-IR spectra of (a) conch shell, (b) clamshell and shells converted at 200ºC for 10 days (c) conch and (d) clam. The wavenumbers of absorption bands are marked in the figure. In spectra (a) and (b), bands at 710 cm^{-1} (carbonate ν4), 860 cm^{-1} (carbonate ν2), and 1490 cm^{-1} (carbonate ν3), result from $CaCO_3$ component in the shells [104-106]. Bands in the range of 2800-3000 cm^{-1} are from the organic matrix in the shell [106]. After reaction at 200ºC for 10 days (c) and (d), new peaks from phosphate ν4 (570 and 600 cm^{-1}), phosphate ν1 (960 cm^{-1}) and phosphate ν3 (1040 and 1100 cm^{-1}) are present in the spectra, indicating the conversion from calcium carbonate to HAP [65, 66, 105]. The band at 630 cm^{-1} is from OH liberation. A very small peak from carbonate ν3 (1490 cm^{-1}) still can be found in spectrum (c), which may result from the presence of a small amount of $CaCO_3$ or the incorporation of carbonate ions in the lattice of HAP [65, 66].

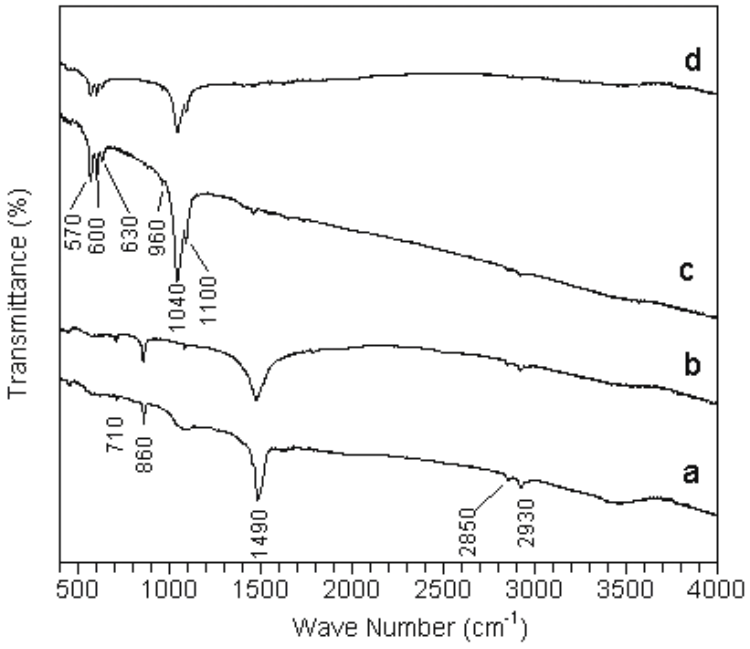

Figure 4-5. FT-IR spectra of (a) conch shell, (b) clam shell, (c) conch converted at 200ºC for 10 days, and (d) clam converted at 200ºC for 10 days.

Molluscan shell can be divided into three primary sections: periostracum (outer), prismatic (middle) and nacreous (inner) layers [107, 108]. The prismatic and nacreous layers are the main structural portions, which determine the mechanical properties of the shell. The original conch shell has three layering scales, composed of first-order lamellae, which are subdivided into second-order lamellae, and further subdivided into third-order lamellae [109-111]. Figure 4-6a shows the optical photograph of polished section of conch converted at 180ºC for 1 day. First-order lamellae (about 30μm thick) and second-order lamellae (about 10-20μm wide) of conch can be observed. The reaction front grew inward from the surface (right side) converting the mineral phase aragonite to hydroxyapatite, while maintaining the structural lamella architecture. Figure 4-6b shows an optical photograph of a polished section of the giant clamshell converted at 180ºC for 1 day. The reaction front grew inward from the surface (right side) converting the mineral phase aragonite to hydroxyapatite, while maintaining the dense structure of the columnar grains of the clamshell.

In order to measure the thickness of the converted HAP layers, pieces from the middle portion of each converted conch shell were sectioned. These pieces were then mounted and polished. The measurement of thickness of the HAP layer on one surface of the shell is schematically shown in Figure 4-6a. Fifteen lines (such as lines: L1, L2 in Figure 4-6a) were drawn across the thickness of the HAP layer, and the average length of the 15 lines was calculated. The average thickness of HAP layer on the opposite surface was calculated by the same method. The summed thickness of these two HAP layers was then used as the total thickness of the HAP layers on converted conch shell in Figure 4-7. Figure 4-7 shows that with increasing reaction time, more

$CaCO_3$ crystals were converted to HAP, in agreement with the XRD results. After 20 days, HAP layers about 830μm thick were formed on the converted conch sample. Similar results were obtained for the giant clamshell conversion.

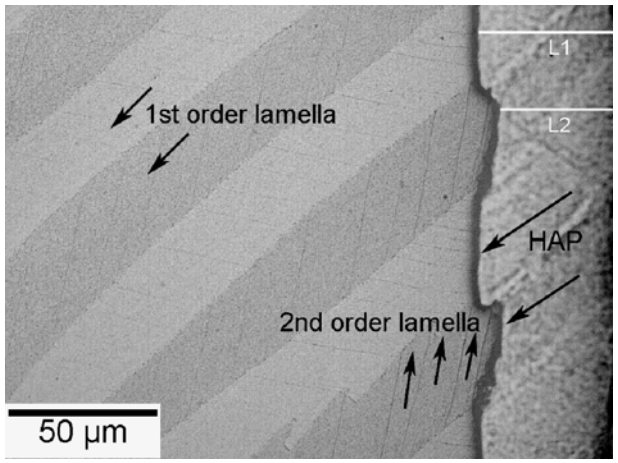

(a)

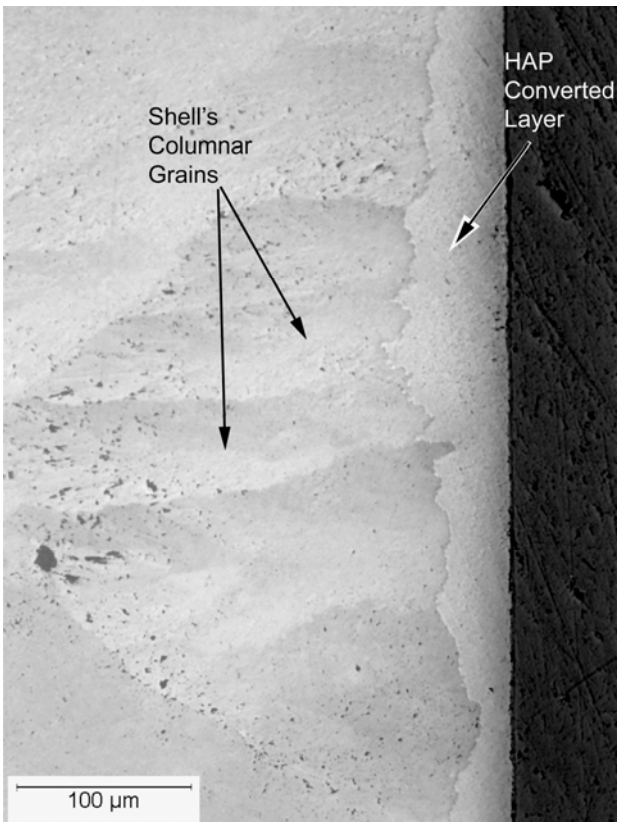

(b)

Figure 4-6. Optical photographs of (a) polished section of conch converted at 180ºC for 1 day, and (b) polished section of giant clamshell converted at 180ºC for 1 day.

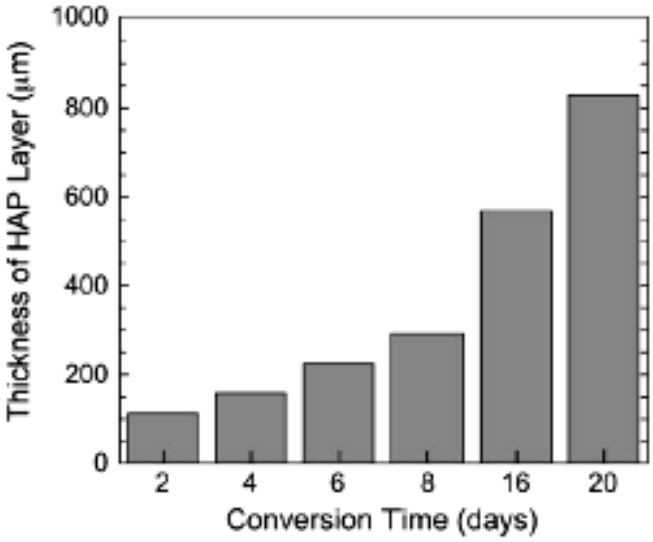

Figure 4-7. Thickness of HAP layers on conch shell converted at 180ºC.

SEM images of the original and converted conch shells and related EDS spectra were shown in Figure 4-8. Figure 4-8a shows the structures of the macro-layer of the conch shell. First-order lamellae (white arrow heads), composed of many second-order lamellae (white arrows), which are formed by third-order lamellae (black arrows) can be seen in Figure 4-8a and Figure 4-8b. Figure 4-8c is the SEM image of conch converted at 180ºC for 10 days. The left portion of the image is from the original shell (black arrows). The HAP layer (marked with a white arrow), which has a very dense structure (Figure 4-7d), replaced the $CaCO_3$ through the hydrothermal reaction. The components of these two phases were identified by EDS (Figure 4-8e and Figure 4-8f). The EDS spectrum from the HAP portion (Figure 4-8f) has the characteristic peak of phosphorus.

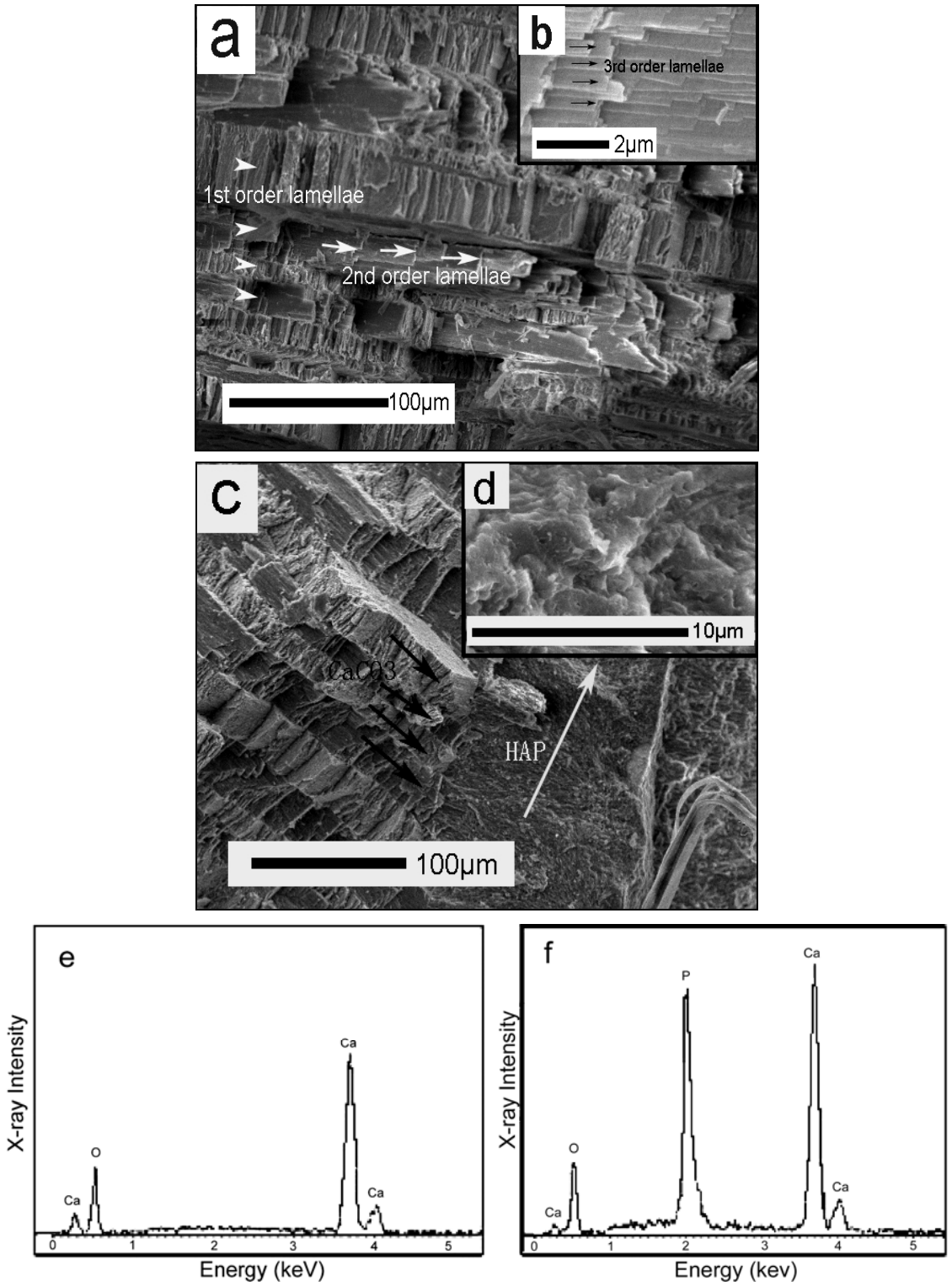

Figure 4-8. SEM images of conch shell (a, b is magnification of second-order lamella), conch converted at 180ºC for 10 days (c, d is magnification of HAP portion), and the EDS spectra from $CaCO_3$ portion (e) and HAP portion (e) in (c).

Figure 4-9 shows SEM images of the original clamshell, the converted clam, and related EDS spectrum. The original clamshell has many layers (Figure 4-9a), which are composed by small, aligned $CaCO_3$ plates (Figure 4-9b), while other parts of the original clamshell are composed of larger $CaCO_3$ plates (Figure 4-9c). Figure 4-9d is an image from clam converted at 180ºC for 20 days, which has the similar morphology to Fig. 10c. The EDS spectrum (Figure 4-9e) from layers in Fig. 10d indicates that they are composed of HAP. This result indicates that the aragonite to HAP conversion occurred in this part preserving the original structural morphology of the shell.

The fracture stresses of three different conch samples converted at 180ºC, and that of compact human bone [27] are shown in Figure 4-10a. The average fracture stresses for the three conch samples were 218, 137 and 164 MPa, respectively. The compressive strength of the compact human bone is about 170-193 MPa, loaded parallel to the bone axis, and about 133 MPa loaded normal to the bone axis [27]. Conch shell samples, after being partially converted to HAP have mechanical strength values very similar to compact bone, which indicates that they can be used as load-bearing implants. Figure 4-10b shows the compression results of original clam shells (S1), clam partially converted at 200℃ for 5 days (S2), and clam completely converted at 200℃ for 10 days, refreshing $(NH_4)_2HPO_4$ solution every 2 days (S3). The average fracture strength for the three clam samples are 149, 89 and 71 MPa, respectively. Due to the formation of small cracks in some samples after the conversion, the fracture strength of completely converted clam (S3) varies more significantly from sample to sample, and the average fracture strength of completely converted clam is only about half that of the original clam shell.

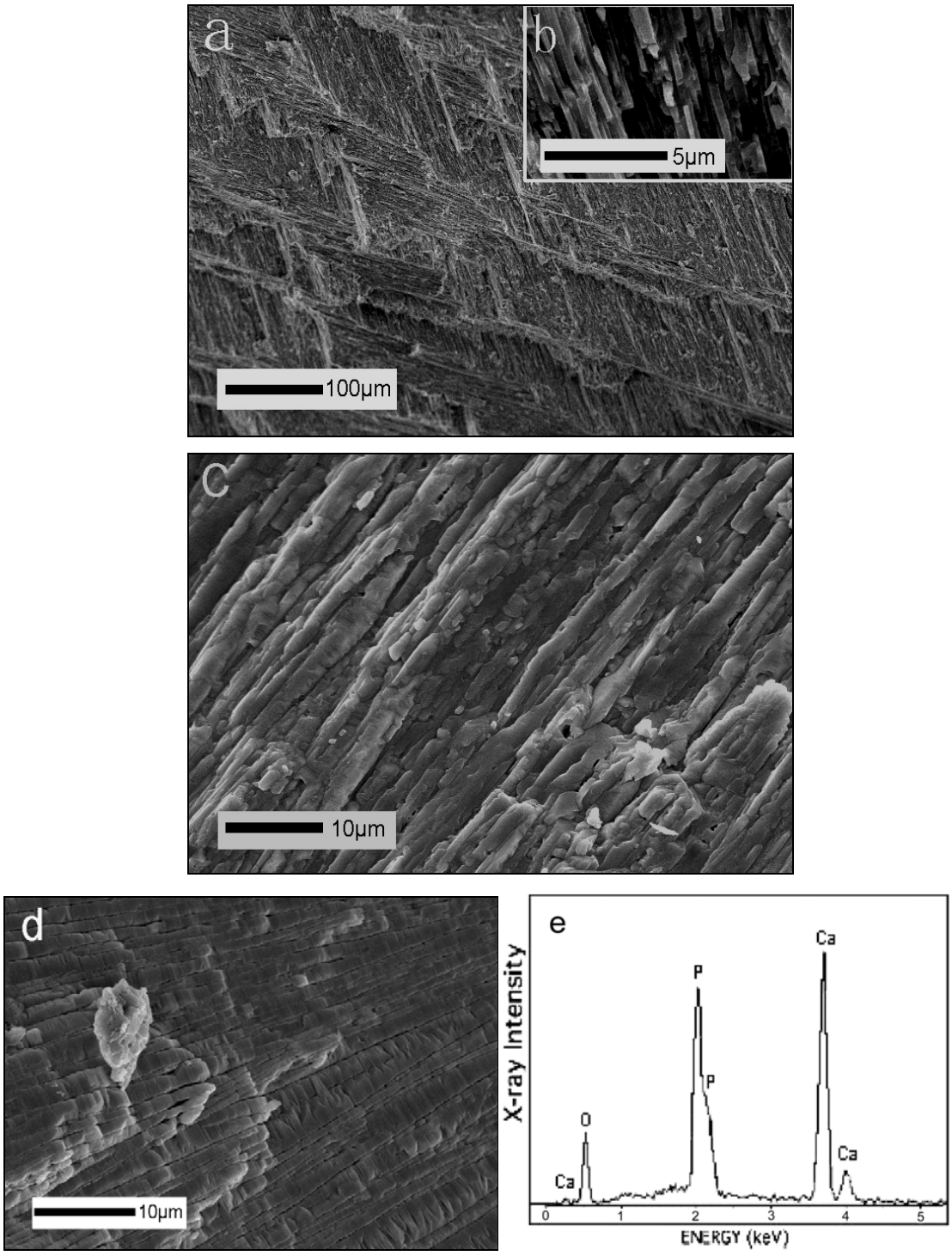

Figure 4-9. SEM images of clamshell [(a), (b), (c); (b) is a higher magnification of a layer in (a)], (d) clam converted at 180ºC for 20 days, and (g) the EDS spectrum from region (d).

Figure 4-11 shows the micro-CT images of the converted conch implant and an untreated control after the operation and after 6 weeks implantation. The micro-CT image after 6 weeks implantation (Figure 4-11b) showed no migration or movement of the implant, compared with the post-operation image (Figure 4-11a). No detectable implant resorption was observed. The untreated control remained empty after 6 weeks (Figure 4-11c), and there is no evidence of a spontaneous fusion. Figure 4-12 shows the micro-CT images of the converted clam implant and an untreated control after the operation and at 6 weeks implantation. The results are similar to those obtained for the converted conch sample. The implant showed no migration or movement of the implant after 6 weeks implantation (Figure 4-12b). No evidence of a spontaneous fusion was found for the control defect (Figure 4-12c).

The histological examination of the sectioned implants (Figure 4-13) shows direct bony apposition with the implant. There was no evidence of fibrosis tissue ring around the implants. These findings indicate that the implant is biocompatible and undergoes osseointegration (Figure 4-13a), also indicating that there was no loosening of implant. The untreated control (Figure 4-13b) remained empty with some evidence of a fibrosis ring (blue ring) around the hole. Newly formed bone can be seen growing up to and around (white arrow heads in Figure 4-13c and Figure 4-13d) the converted conch and clam implants. The interfaces between implant and bone are tightly joined, which indicates the good biocompatibility of these converted shell samples.

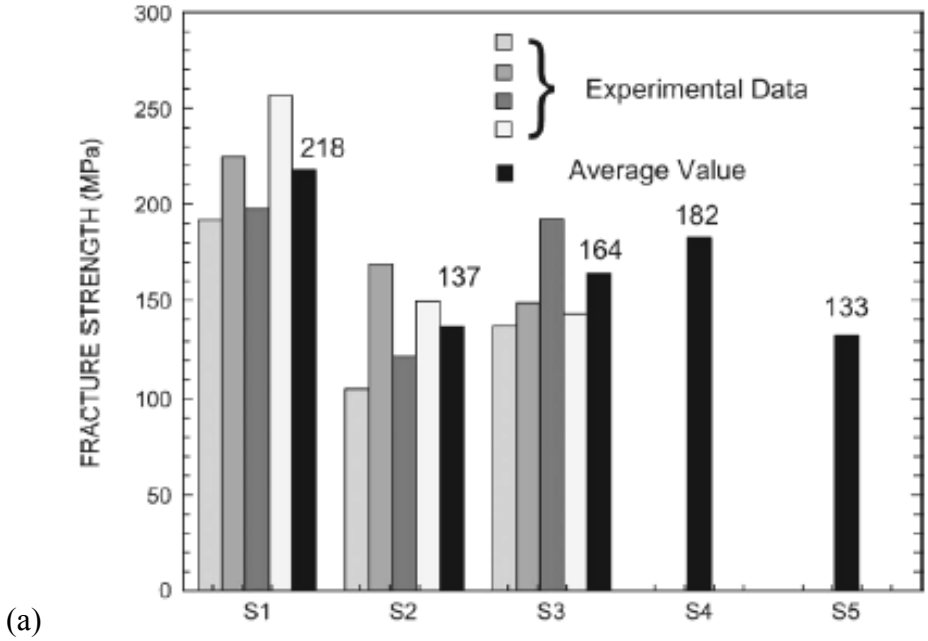

(a)

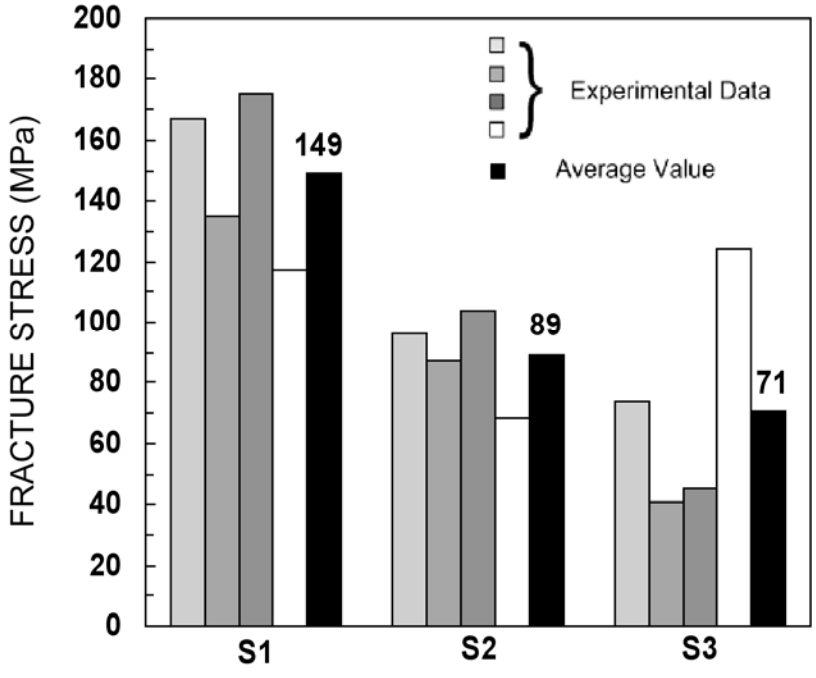

(b)

Figure 4-10. Quasi-static compression results of (a) conch converted 180ºC for 4 days (S1), 8 days (S2), 20 days (S3) and average compressive strength of compact human bone loaded parallel to the bone axis (S4) and loaded normal to the bone axis (S5), and (b) original clam (S1), and clam converted at 200℃ for 5 days (S2) and 10 days (S3).

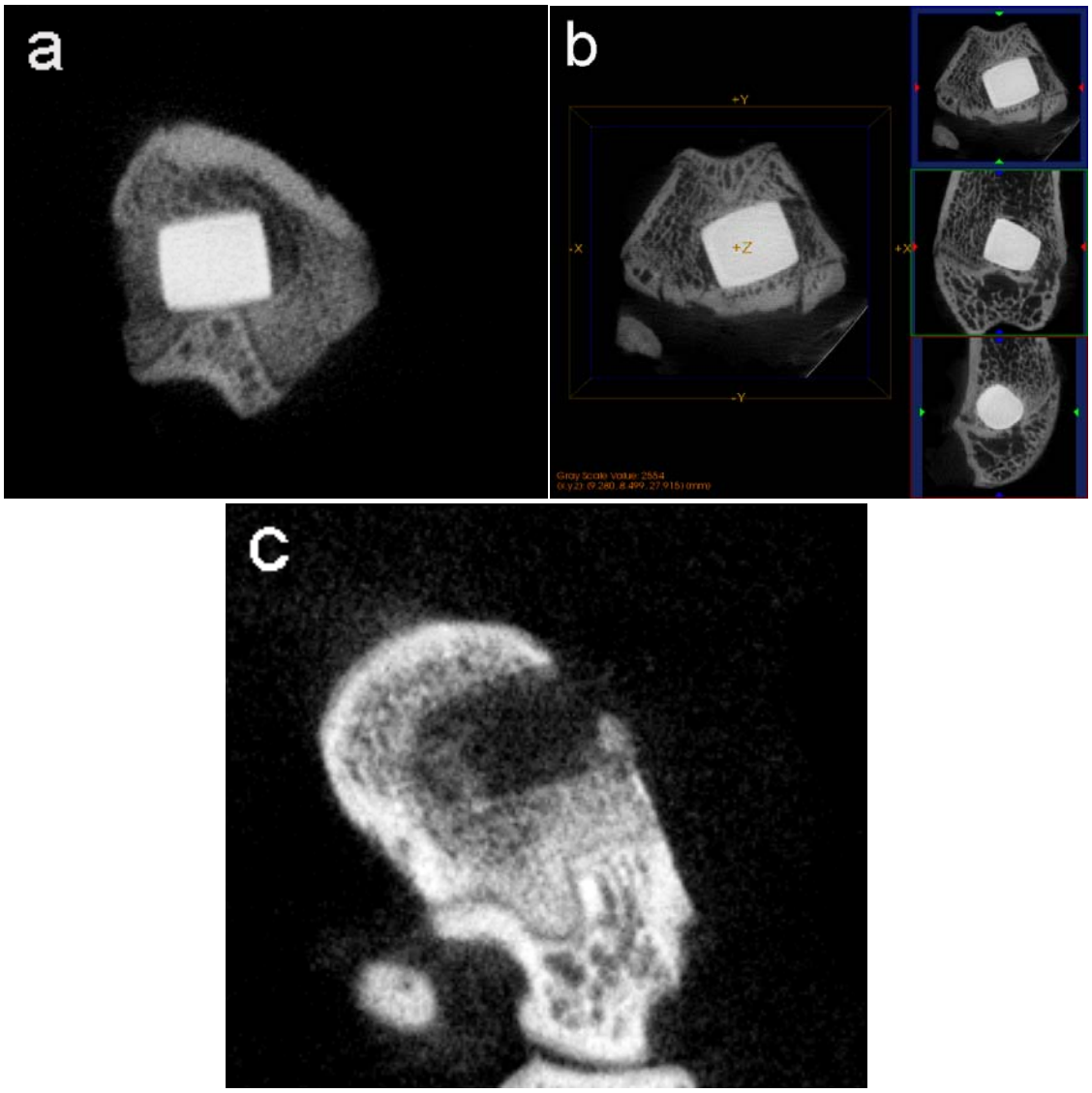

Figure 4-11. Micro-CT images of converted conch implanted in the rat femoral defect: (a) immediately post-operative and (b) after 6 weeks, and (c) images of untreated control defect immediately post-operative.

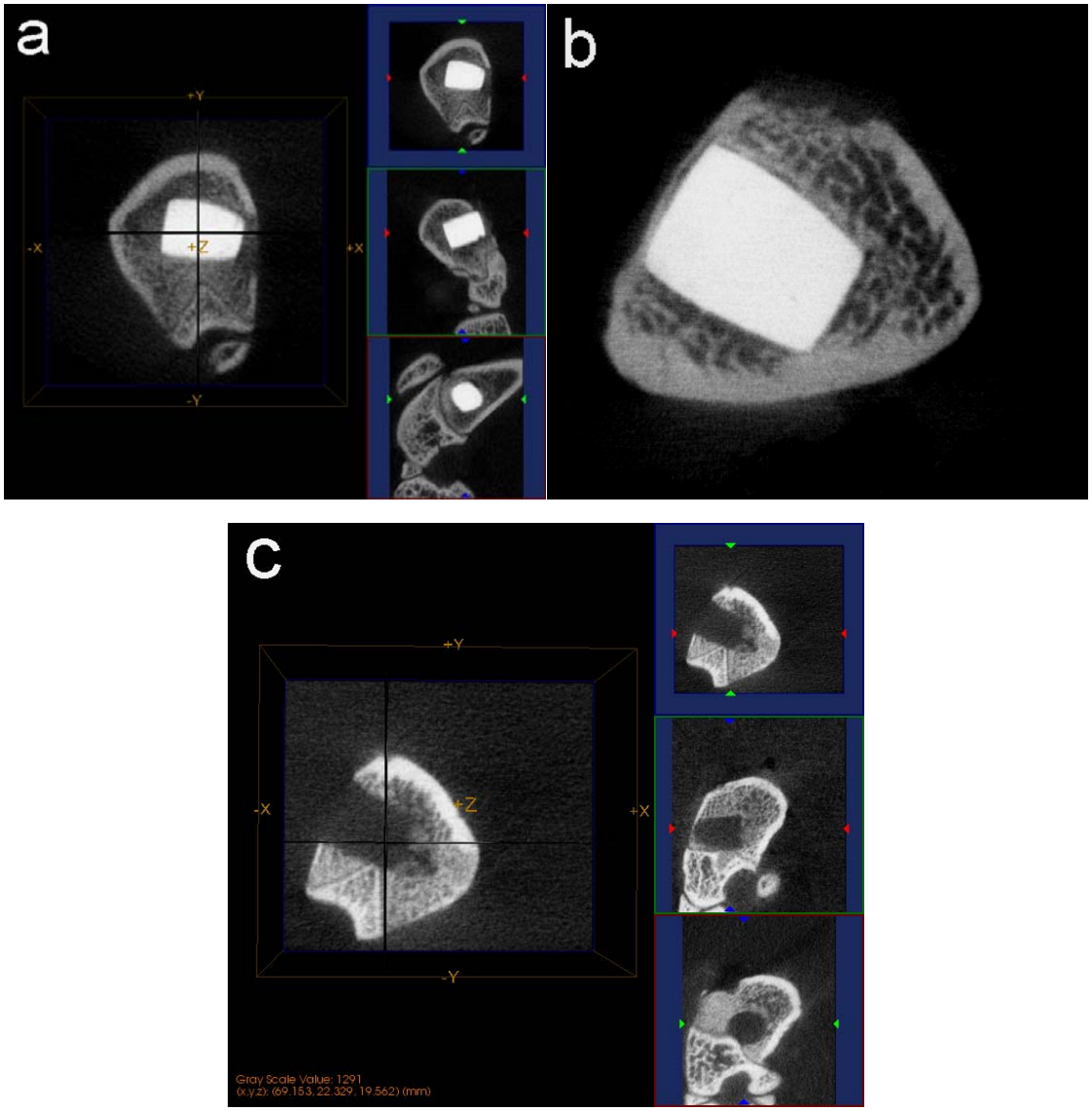

Figure 4-12. Micro-CT images of converted clam sample implanted in the rat femoral defect: (a) immediately post-operative and (b) at 6 weeks, and (c) images of untreated control defect immediately post-operative.

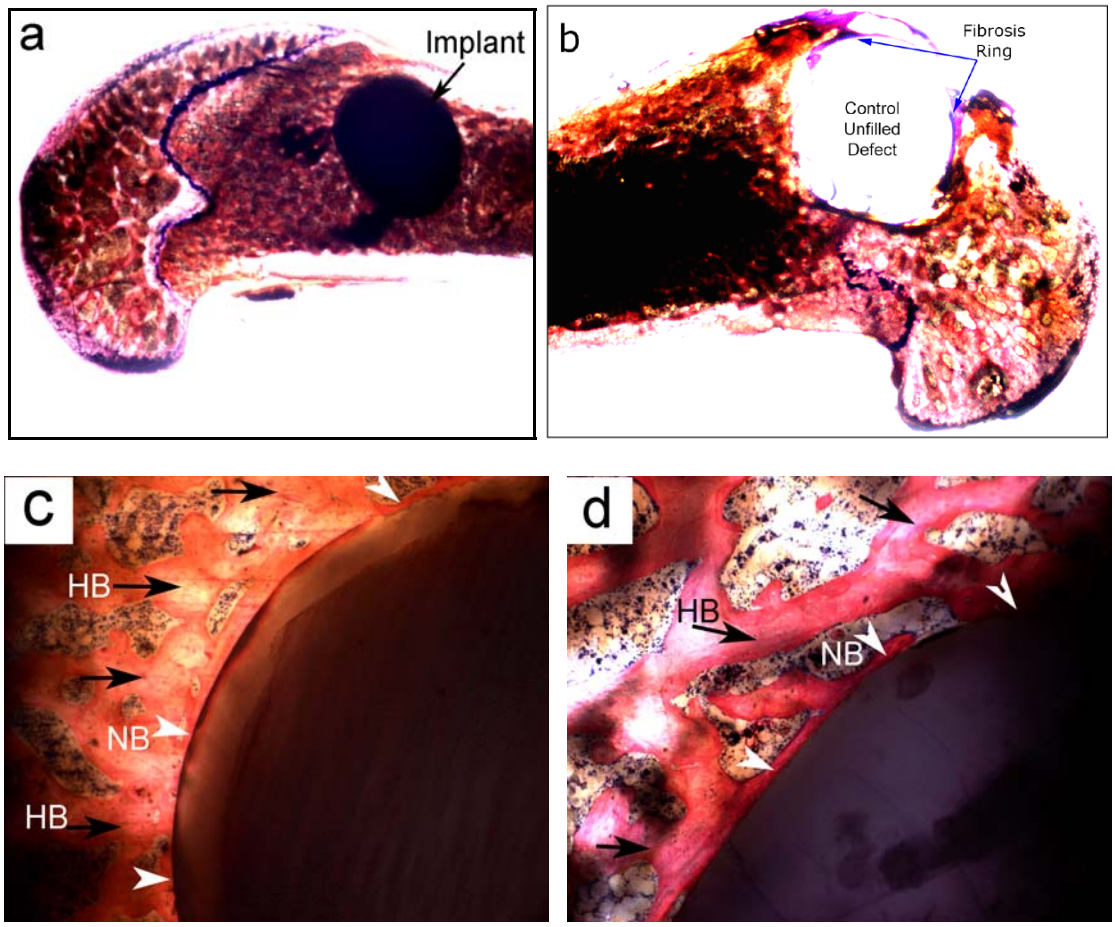

Figure 4-13. Histological sections after 6 weeks implantation: (a) the converted conch implant in the femoral defect, (b) the untreated control defect, (c) magnification of the converted conch implant and (d) magnification of converted clam implant (white arrow heads show the newly formed bone-NB and black arrows indicate adjacent host bone-HB).

SEM images and related EDS mapping of the tissue samples of converted conch and clam implants after 6 weeks implantation are shown in Figure 4-14 and Figure 4-15, respectively. Secondary electron images (Figure 4-14a and Figure 4-15a) clearly show the growth of newly formed bone (NB) around the implants, which indicates good bioactivity of the converted shell implants. EDS mapping of calcium (Figure 4-14b and Figure 4-15b), and phosphorus (Figure 4-14c and Figure 4-15c) show the implants are

homogeneously composed of calcium phosphate, which indicates the good conversion of the shells to HAP. The mapping results also indicate a tightly joined interface between the implants and new bone.

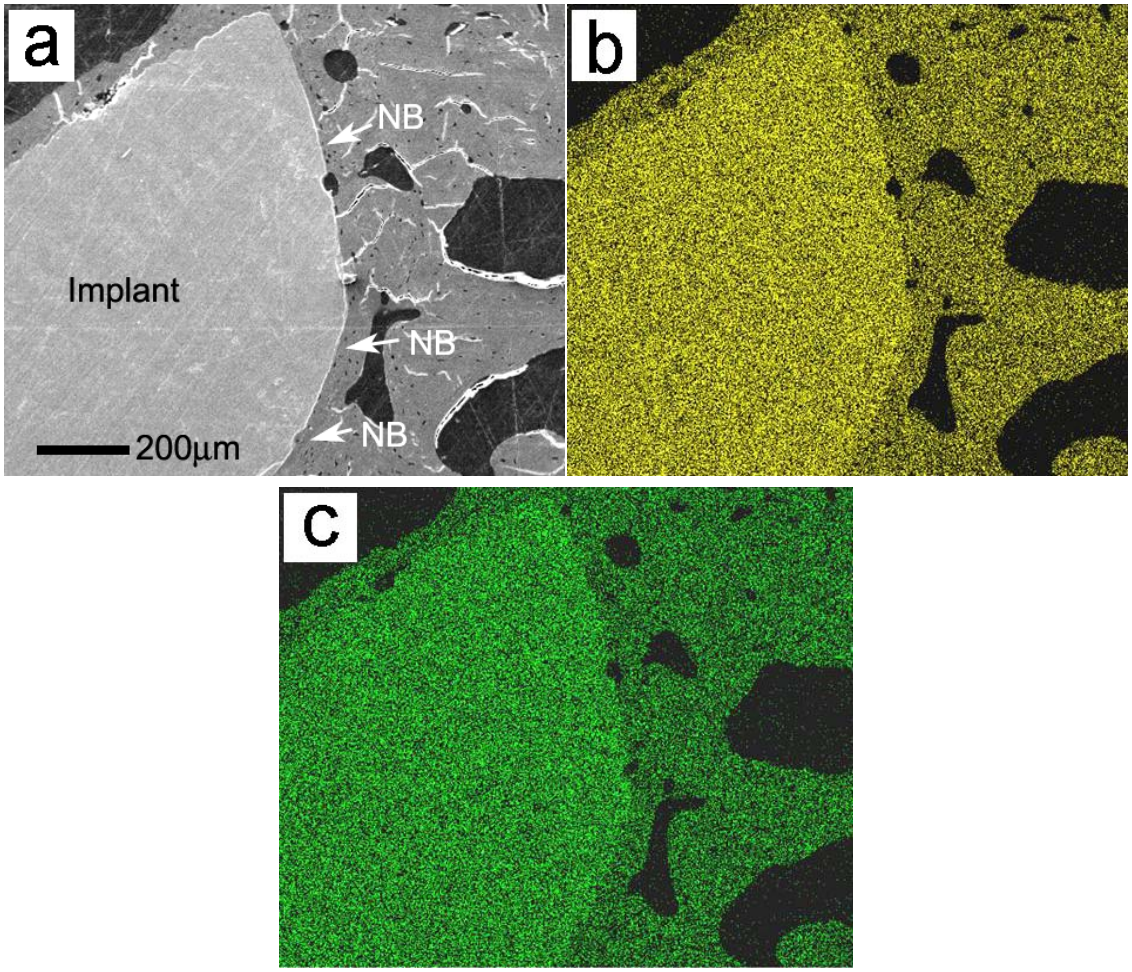

Figure 4-14. (a) Secondary electron image of a polished tissue sample of converted conch implant after 6 weeks implantation [NB indicates the newly formed bone] and related EDS mapping of (b) calcium, (c) phosphorus.

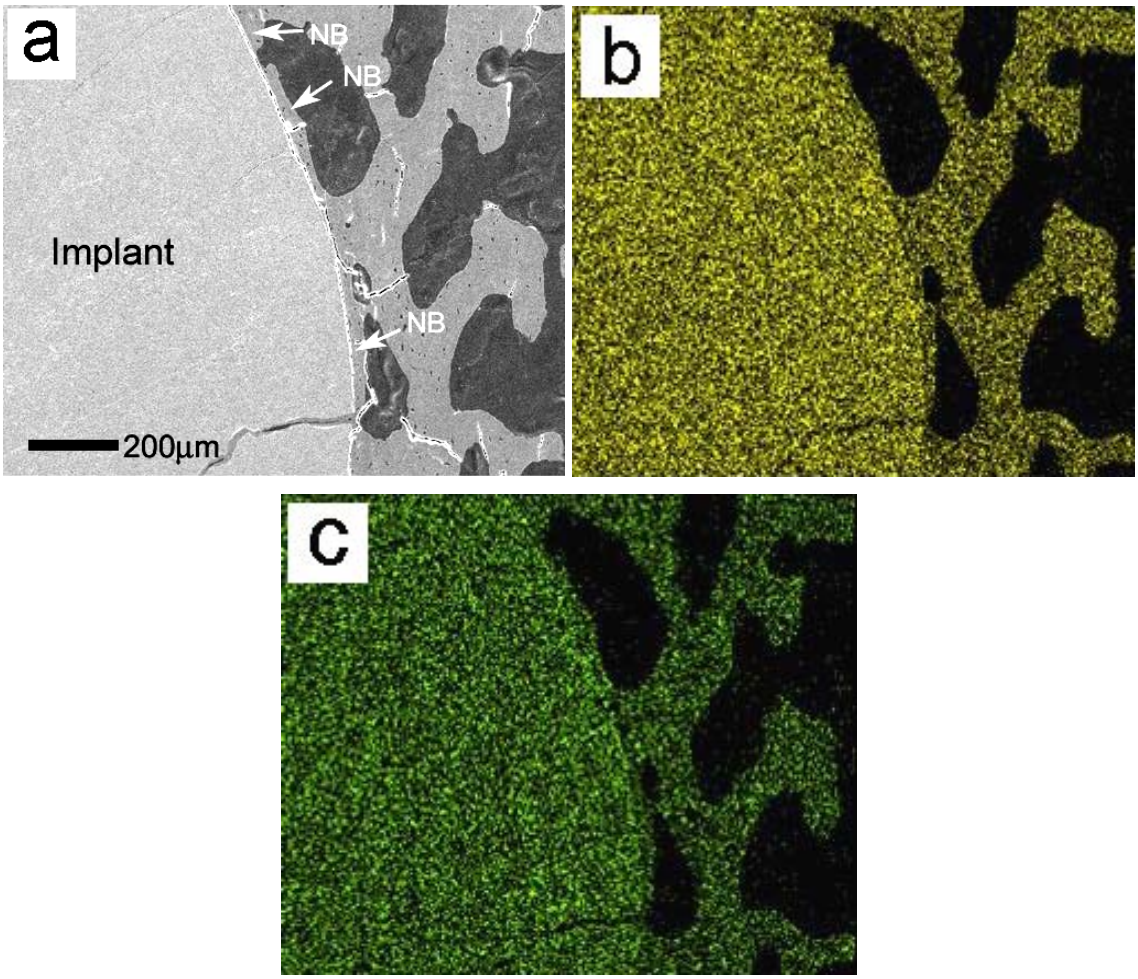

Figure 4-15. (a) Secondary electron image of a polished tissue sample of converted clam implant after 6 weeks implantation [NB indicates newly formed bone] and related EDS mapping of (b) calcium, (c) phosphorus.

4.1.3 Conclusions

Dense structures of HAP were created by hydrothermal conversion of conch and clamshells at relatively low temperature (~200ºC). The conversion process was accelerated at higher temperature, and the thickness of the HAP layer increased with increasing conversion time. The average fracture stress is ~137-218 MPa, for conch shell samples, and ~70-150 MPa for original and converted clamshell samples, which is

close to the mechanical strength of compact human bone. This indicates that the converted shell samples can be used as implants in load-bearing applications. After implantation in rat femoral defects for 6 weeks, newly formed bone was found to grow up to and around the converted shell samples. The tightly joined interface between the implant and bone indicates the good biocompatibility of these converted shell samples.

4.2 Conversion of urchin spines to porous Mg-substituted tricalcium phosphate

Based on observed tissue response, synthetic bone-graft substitutes can be classified into: inert (e.g. alumina, zirconia), bioactive (e.g. hydroxyapatite, bioactive glass) and resorbable substitutes (e.g. tricalcium phosphate, calcium sulfate) [112]. Among them, the resorbable bone-graft substitutes are preferred for bone defect filling because they can be replaced by new natural bone after implantation. Beta-tricalcium phosphate [$Ca_3(PO_4)_2$, β-TCP] ceramics, as an example, have been widely used as bone substitute materials, due to its good biocompatibility, chemical stability and resorbability *in-vivo* [113-118]. Pure β-TCP is hard to prepare in aqueous systems under normal laboratory conditions (i.e. up to 100ºC and at atmospheric pressure). However, preparation of magnesium-substituted tricalcium phosphate [$(Ca,Mg)_3(PO_4)_2$, β-TCMP] by precipitation or hydrolysis methods in solution has been reported [28, 94]. These results indicate that the presence of Mg stabilizes the β-TCP structure. In addition, the presence of Mg in bone substitutes has been reported to promote new bone formation and affect bone mineralization *in-vivo* [5, 119]. Porous β-TCMP structures may be ideally suited

for bone scaffold structures, allowing both osteoconductivity for bone in-growth and good resorbability for eventual full replacement by natural bone.

This investigation describes the preparation of porous β-TCMP by hydrothermal conversion of spines of the echinoid *Heterocentrotus mammillatus* (*H. mammillatus)* and *Heterocentrotus trigonarius* (*H. trigonarius*) sea urchins, and their subsequent evaluation for biocompatibility. Hydrothermal conversion of natural calcium carbonate skeletons to hydroxyapatite (HAP) has been reported [89, 99-102]. However, the spines mainly consist of large single crystals of Mg-rich calcite [$(Ca,Mg)CO_3$] [89]. These single crystals usually have smooth, continuously curved surfaces that form a three-dimensional fenestrated mineral network [120]. After the hydrothermal conversion, the product is β-TCMP, rather than HAP, due to the substitution of Mg. The β-TCMP product still maintains the interconnected porous structure of the original spine. Evaluation of the suitability of these converted spines for bio-implant materials was then evaluated in terms of their mechanical properties as well as their biocompatibility via *in-vivo* testing.

4.2.1 Materials and methods

The synthesis is a hydrothermal conversion process using as starting materials: diammonium hydrogen phosphate [$(NH_4)_2HPO_4$, Fisher Scientific] and spines of the echinoid *Heterocentrotus trigonarius and Heterocentrotus mammillatus* sea urchins, as shown in Figure 4-16a. These spines were cut into cylindrical samples [~10 mm (diameter) × 6 mm (long)] shown in Figure 4-16b, then cleaned with deionized water and placed in an autoclave. The autoclave was filled with a specified concentration of

$(NH_4)_2HPO_4$ solution, sealed and heated at different temperatures, from 180°C to 240°C, for different durations. In these experiments, the concentration of $(NH_4)_2HPO_4$ solution ranged from 0.1g/ml to 0.2g/ml.

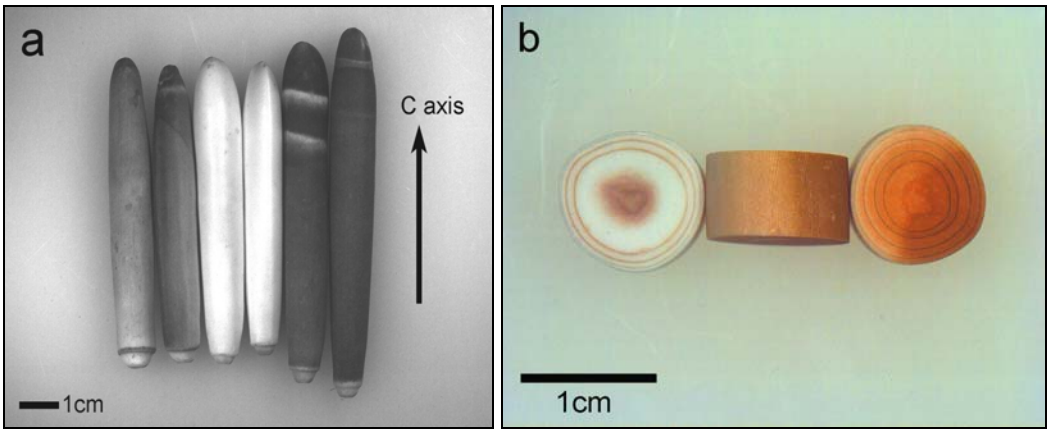

Figure 4-16. Optical images of (a) original spines of *H. mammillatus* and *H. trigonarius*, (b) Spine samples for hydrothermal conversion and compression tests.

Quasi-static compression tests were conducted on a servohydraulic test frame at a strain rate of 10^{-3}/s. The original spines and converted spines were cut into cylindrical samples ~10 mm (diameter) × 6 mm (long), and tested as shown in Figure 3-4.

For *in-vivo* tests, 5 rats were used. Procedures for surgery, micro-CT imaging and histology study follow Section 3.3.1, 3.3.2 and 3.3.3.

4.2.2 Results and discussion

Conversion process

The spines of sea urchin are mainly composed of Mg-rich calcite [89]. Each spine is considered to be a single crystal [120, 121]. These single calcite crystals of spines are believed to form via a transient amorphous calcium carbonate phase [122, 123].

However, Towe [124] reported that the interior portions of spines of *Strongylocentrotus droebachiensis* have the morphology of a single crystal, whereas the exterior is a polycrystalline aggregate with preferred orientation.

Spines of *H. mammillatus* and *H. trigonarius* were used in our experiment. Powder XRD result of a spine is shown in Figure 4-17. Due to the existence of Mg, the diffraction peaks shift to larger angles in the pattern, compared with a pure calcite phase (red dash lines). The lattice constants of Mg-calcite in the pattern were calculated with MDI Jade7 software: a = 4.95Å and c = 16.83Å (pure calcite, hexagonal, a = 4.99Å, c = 17.00Å). This indicates lattice contractions of both a- and c-axes due to the substitution of Mg in the calcite lattice.

Figure 4-18 shows the XRD patterns of spines after hydrothermal conversion at 180°C for (a) 1 day and (b) 2 days. After reaction for 1 day, most of the spine material was converted to β-TCMP, while a small amount of calcite still existed. After reaction for 2 days, the spine was completely converted to β-TCMP. Hydrothermal conversion of other marine $CaCO_3$ skeletons, such as coral, cuttlebone and seashells, have been reported to produce HAP [89, 99-102]. The conversion of urchin spines produced β-TCMP instead of HAP, due to the existence of Mg in the lattice, which stabilizes the β-TCP structure [28, 94].

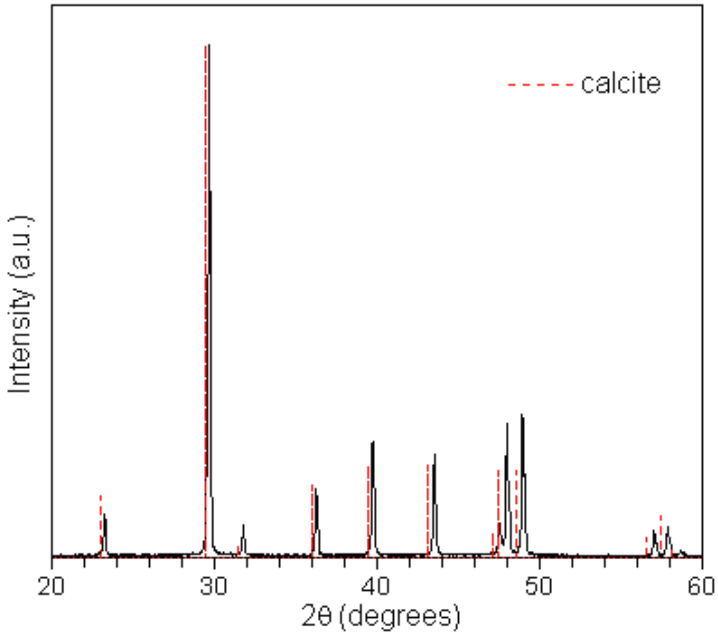

Figure 4-17. Powder XRD pattern of original sea urchin spine.

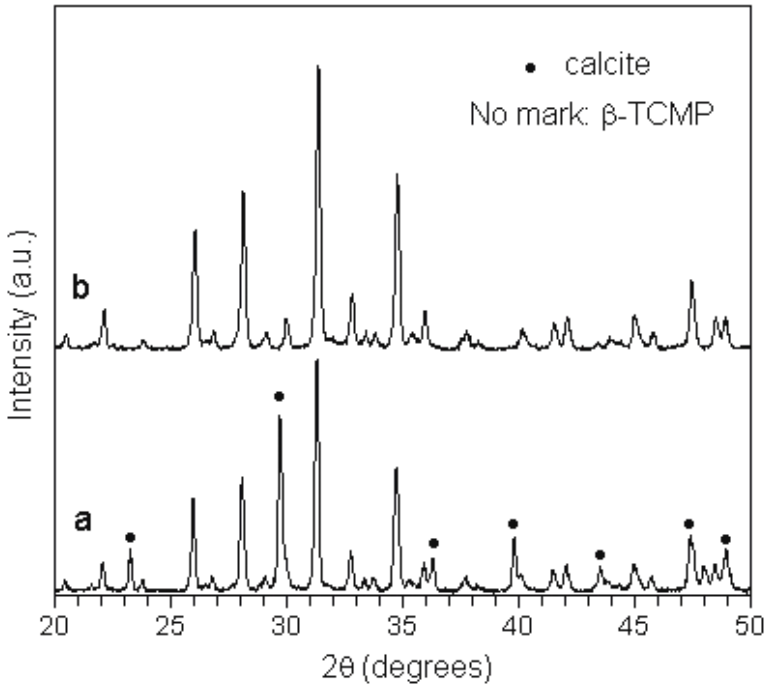

Figure 4-18. Powder XRD pattern of spines converted at 180°C for (a) 1 day and (b) 2 days.

The conversion from Mg-rich calcite [$(Ca,Mg)CO_3$] to β-TCMP [$(Ca,Mg)_3(PO_4)_2$] is thought to follow the ion-exchange reaction (2) given below [89]:

(2) $3(Ca,Mg)CO_3+2(NH_4)_2HPO_4 \rightarrow (Ca,Mg)_3(PO_4)_2+2(NH_4)_2CO_3+H_2CO_3$

Figure 4-19 shows FT-IR spectra of the original spine (a) and spine converted at 180°C for 1 day (b) and 2 days (c). The wavenumbers of absorption peaks are marked in the spectra. In Figure 4-19(a), bands at 724 cm^{-1} (carbonate ν 4), 879 cm^{-1} (carbonate ν 2), and 1424 cm^{-1} (carbonate ν 3), result from the $CaCO_3$ component in the spine [105]. There are also OH bending (1651 cm^{-1}) and OH stretching (~3460 cm^{-1}), which is from absorbed water in the sample. After hydrothermal reaction at 180ºC for 1 day (b), new peaks from phosphate ν 4 (568 and 607 cm^{-1}) and phosphate ν 3 (1044 and 1089 cm^{-1}) are present in the spectrum [68], while a significant decrease in intensity of carbonate peaks is observed. This indicates the conversion from calcium carbonate to calcium phosphate, consistent with the XRD result (Figure 4-18). After reaction for 2 days [Fig. 4 curve (c)], most peaks in the spectrum are from phosphate, with only a small peak from carbonate ν 3 (1424 cm^{-1}), which may result from a small amount of $CaCO_3$ still present in the product. However, the amount of $CaCO_3$ is sufficiently small that it does not appear in the XRD result [Figure 4-18, curve (b)].

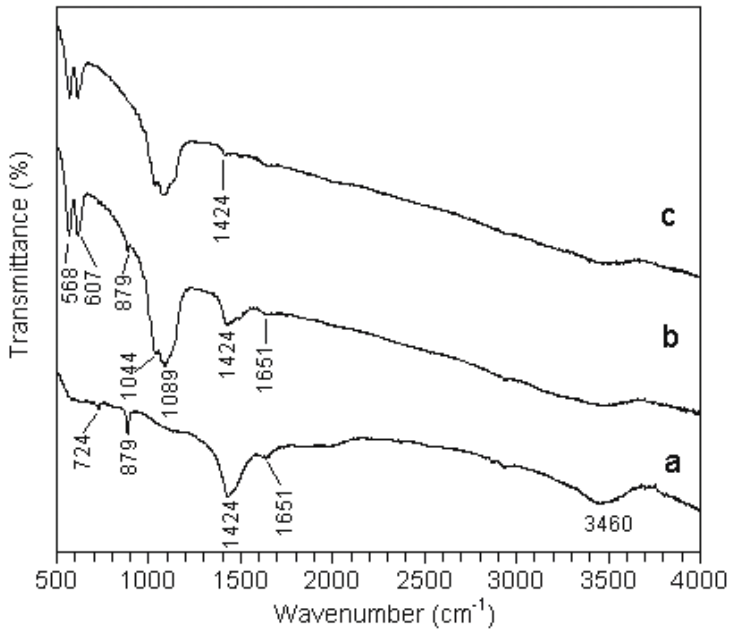

Figure 4-19. FT-IR spectra of (a) sea urchin spine, (b) spine after hydrothermal reaction at 180ºC for 1 day and (c) spine after hydrothermal reaction at 180ºC for 2 days.

Morphology study

The fenestrate microstructure is found in almost all echinoderm skeletal ossicles [125, 126]. However, few sea urchiin spines are large enough for practical applications. Spines of *H. mammillatus* and *H. trigonarius* (Figure 4-16a) have sufficient size to be used for bio-implants and are readily available as a material source. The long axis of the spine is marked as the 'c' axis (Figure 4-16a). The spines are ~1 cm wide and several centimeters long. Figure 4-20a shows the growth rings of the spine in the section normal to c axis. The fenestrated structure can also be observed in the image. Spines can be easily machined or fashioned into particular shapes as different individual implants. Examples of spines machined into screw-like threaded rods, which could be

used as fixation implants are shown in Figure 4-20b. These spines can also be easily machined into digit (finger and toe) replacement bone implants.

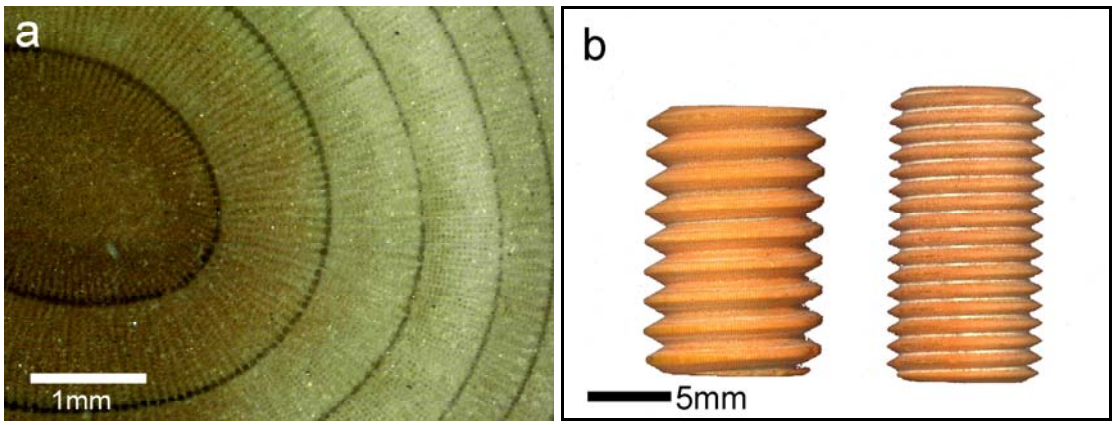

Figure 4-20. Optical images of (a) inner ring structures of a spine, and (b) machined screw-shape spines.

SEM images of spines and related EDS spectra are shown in Figure 4-21. Figure 4-21a is the section of a spine parallel to the c-axis. The growth rings (marked with white arrows) and a highly porous network structure can be observed. Higher magnification of the fenestrated structure (Figure 4-21b) shows the smooth, continuously curved surfaces and smooth fracture surfaces of struts. Most pores in the spine are ~20 – 50μm. Figure 4-21c and Figure 4-21d shows structures of the outer surfaces of spines, which consist of vertical trabeculae, ~100μm thick and parallel to the c-axis. The vertical trabeculae in Figure 4-21c have an obvious gap between each other, while compact vertical trabeculae were found as shown in Figure 4-21d. The EDS spectra, from the inner portion (Figure 4-21e) and the outer surface (Figure 4-21f) of the spine, indicate the characteristic peaks of calcium, magnesium, carbon and oxygen expected for Mg-substituted calcite, consistent with the XRD result (Figure 4-17).

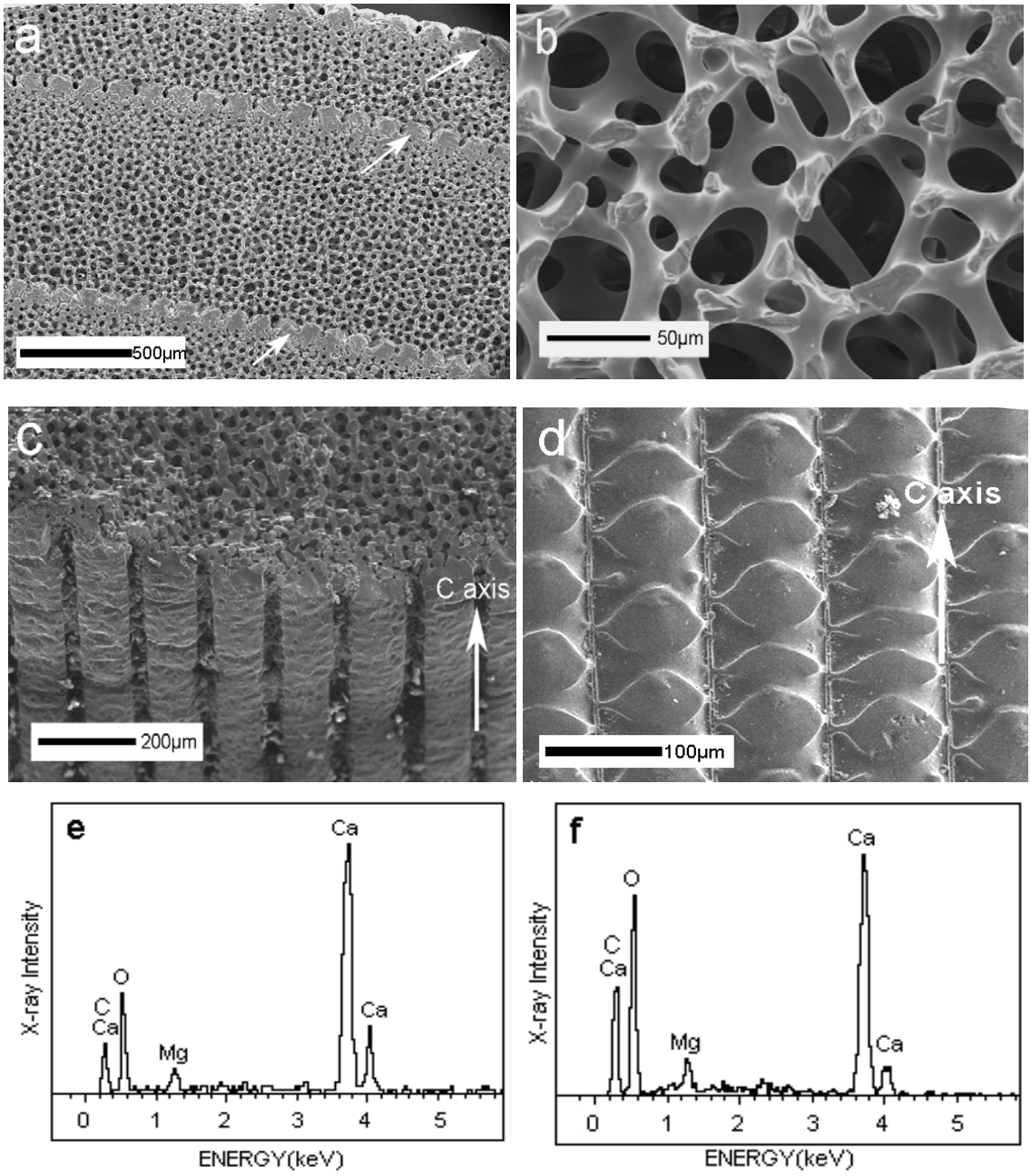

Figure 4-21. SEM images of spines: (a) a section normal to c-axis, (b) magnification of a portion in (a), (c) the vertical trabeculae on the outer surface of a spine, (d) the vertical trabeculae from another spine and EDS spectra of (e) from the inner portion (b) and (f) from the outer surface (d).

Figure 4-22 shows SEM images of the spine after hydrothermal reaction at 180ºC for 4 days and related EDS spectra. Figure 4-22a and Figure 4-22b are images from the

surface and the inner middle portion of the β-TCMP sample, respectively, which indicate that the β-TCMP product still maintains the porous structure of the original spine. The EDS spectrum (Figure 4-22e) from the inner portion shows characteristic peaks of calcium, magnesium, phosphorus and oxygen, which demonstrates the conversion from Mg-rich calcite to β-TCMP. Some precipitates are also observed on the struts at the sample surface (Figure 4-22a). The precipitates are composed of aggregates of tiny particles (Figure 4-22c), and the EDS spectrum from the precipitates (Figure 4-22f) has the characteristic peaks of calcium, phosphorus, oxygen and a small peak of magnesium. These precipitates are believed to be calcium phosphate, formed through the dissolution-reprecipitation process during hydrothermal conversion. On the other hand, the fresh fracture surface of a strut (Figure 4-22d) consists of large particles with dense structures, which is β-TCMP converted from Mg-rich calcite through the ion-exchange reaction. Therefore, the main conversion mechanism in the experiment is the hydrothermal ion-exchange reaction, while there is a secondary dissolution-reprecipitation process to form calcium phosphate precipitates on the surfaces of the sample.

Mechanical Properties

Quasi-static compression tests were performed parallel to the c-axis of the spine at a strain rate of 10^{-3}/s. Compression fracture strengths for the original spines and those converted to β-TCMP at 180ºC for 2 days are compared in Figure 4-23. The fracture strength of typical individual samples and the average values from multiple samples are shown in Figure 4-23. The average fracture strength of spines is ~ 42 MPa, and that of

the converted spines is ~23 MPa. The strength of the converted spines is somewhat higher than the reported fracture strength of cancellous bone (4 – 12 MPa) [127]. This indicates that the converted spine samples (β-TCMP) can be used as either non-load-bearing implants, or minor load-bearing implants, such as digit replacements or spinal fixation scaffolds.

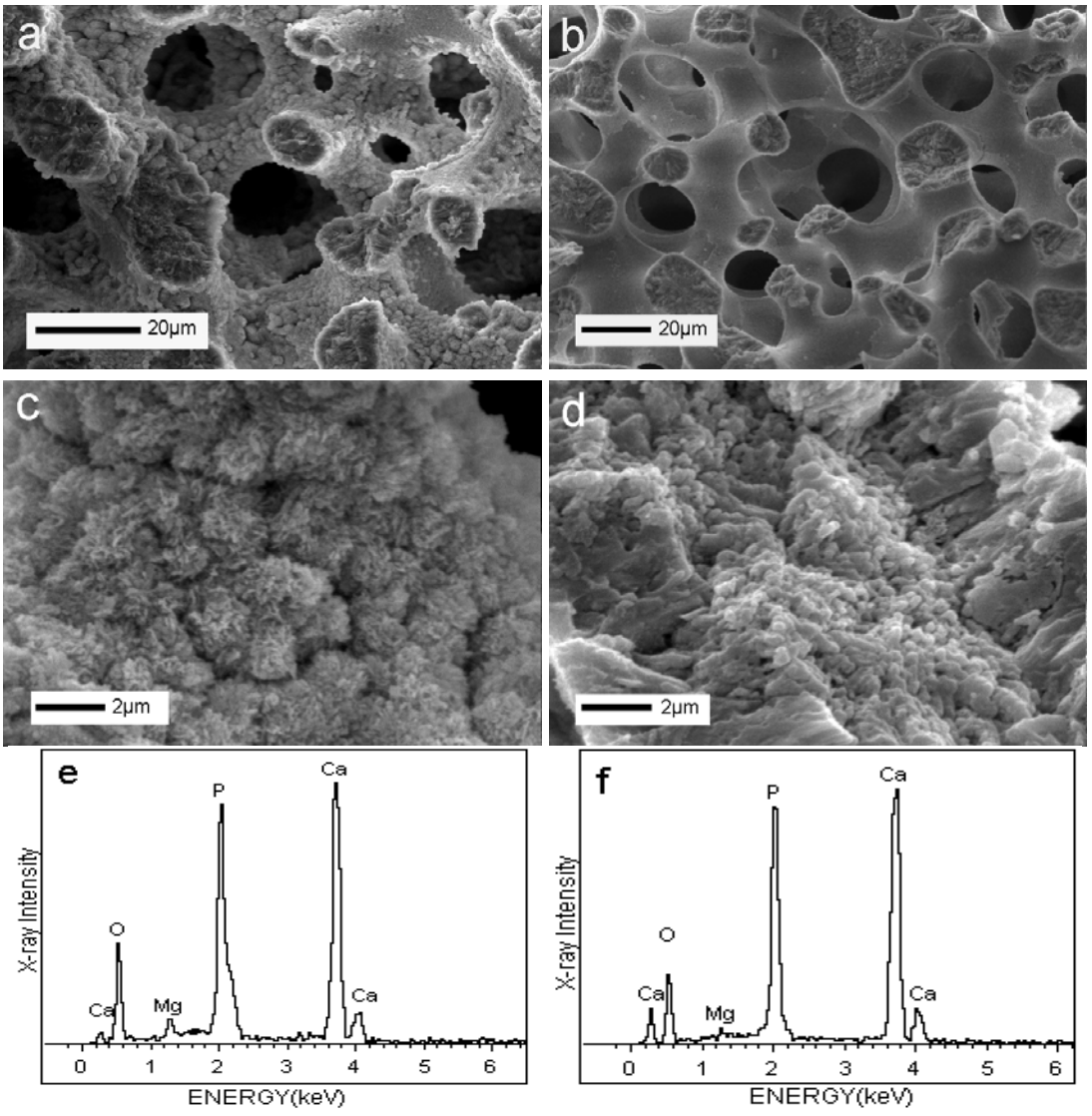

Figure 4-22. SEM images of the spine after hydrothermal reaction at 180ºC for 4 days: (a) sample surface, (b) inner middle portion of the sample, (c) precipitates on a strut in (a), (d) the fracture surface of a strut in (a), and EDS spectra of (e) from inner portion (b) and (f) from precipitates (c).

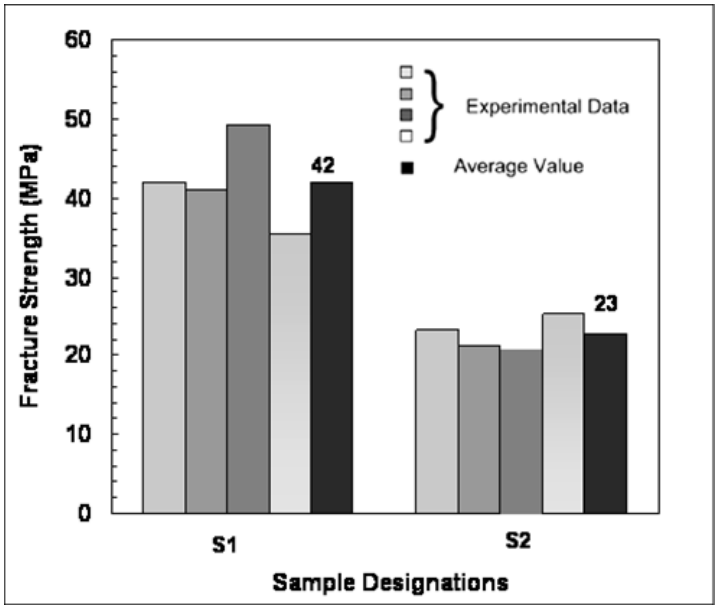

Figure 4-23. Quasi-static compression results of original spines (S1) and spines converted at 180ºC for 2 days (S2).

In-vivo tests

For *in-vivo* test, five β-TCMP samples, spines converted at 180°C for 4 days, were implanted into femoral defects of 5 rats for 6 weeks. Figure 4-24 shows the micro-CT images of the implant and untreated controls immediately post-operative and after 6 weeks implantation. Compared with the post-operative image (Figure 4-24a), the micro-CT image after 6 weeks implantation (Figure 4-24b) showed no migration or movement of the implant. No detectable implant resorption was observed. The untreated control (Figure 4-24c) remained empty after 6 weeks, and there is no evidence of a spontaneous fusion. A faint halo can be seen around the implant on micro-CT imaging (Figure 4-24b).

The histological examination of the sectioned implant (Figure 4-25) shows direct bony apposition with the implant. There was no evidence of fibrosis tissue ring around the implant. These findings indicate that the implant is biocompatible and undergoes osseointegration. The halo seen on micro-CT imaging is likely a consequence of the heightened bone modeling activity seen during early implant incorporation. Newly formed bone can be seen growing up to and around the converted spine implants (small black arrowheads in Figure 4-25c and Figure 4-25d). Some new bone tissue was found to migrate through the pores starting from the outside of the implant through the pores at the edge of the implants (Figure 4-25d). Growth of newly formed bone into the center of the porous structure and resorption of the β-TCMP converted spine may be expected in longer duration *in-vivo* tests. The untreated control (Figure 4-25b) remained empty (i.e. no spontaneous fusion) with some evidence of a fibrosis ring (the blue ring) around the hole.

Figure 4-26 shows the secondary electron image of a polished tissue section containing the β-TCMP implant after 6 weeks implantation and related EDS elemental maps. The brightest network of features in the secondary electron image represents the skeletal structure of the converted spine. The darkest regions in the image are voids filled with epoxy. The medium gray features are natural bone grown up to the surface of the spine structure and migrating into the void spaces of the spine. EDS mapping of Mg (Figure 4-26b) shows the converted spine skeleton, given the spine is originally composed of Mg-rich calcite, and upon conversion now Mg-substituted β-TCP (β-TCMP). EDS mapping of calcium (Figure 4-26c) and phosphorus (Figure 4-26d) indicate that the spine has converted to calcium phosphate, and that the materials filled

in the porous spine skeleton are also composed of calcium and phosphorus, which indicates the newly-formed interpenetrated bone.

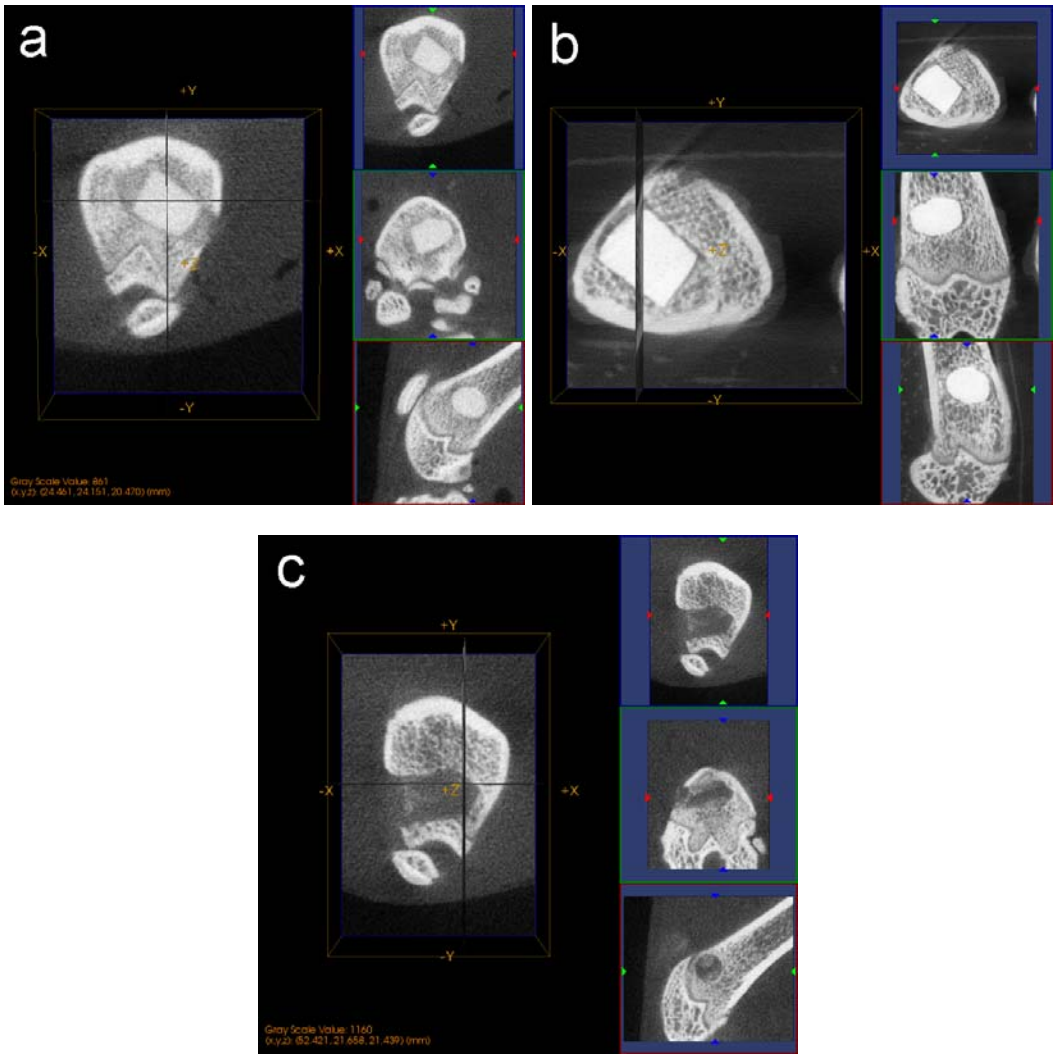

Figure 4-24. Micro-CT images of β-TCMP sample implanted in the rat femoral defect (a) immediately post-operative and (b) at 6 weeks; and (c) images of untreated control defect immediately post-operative.

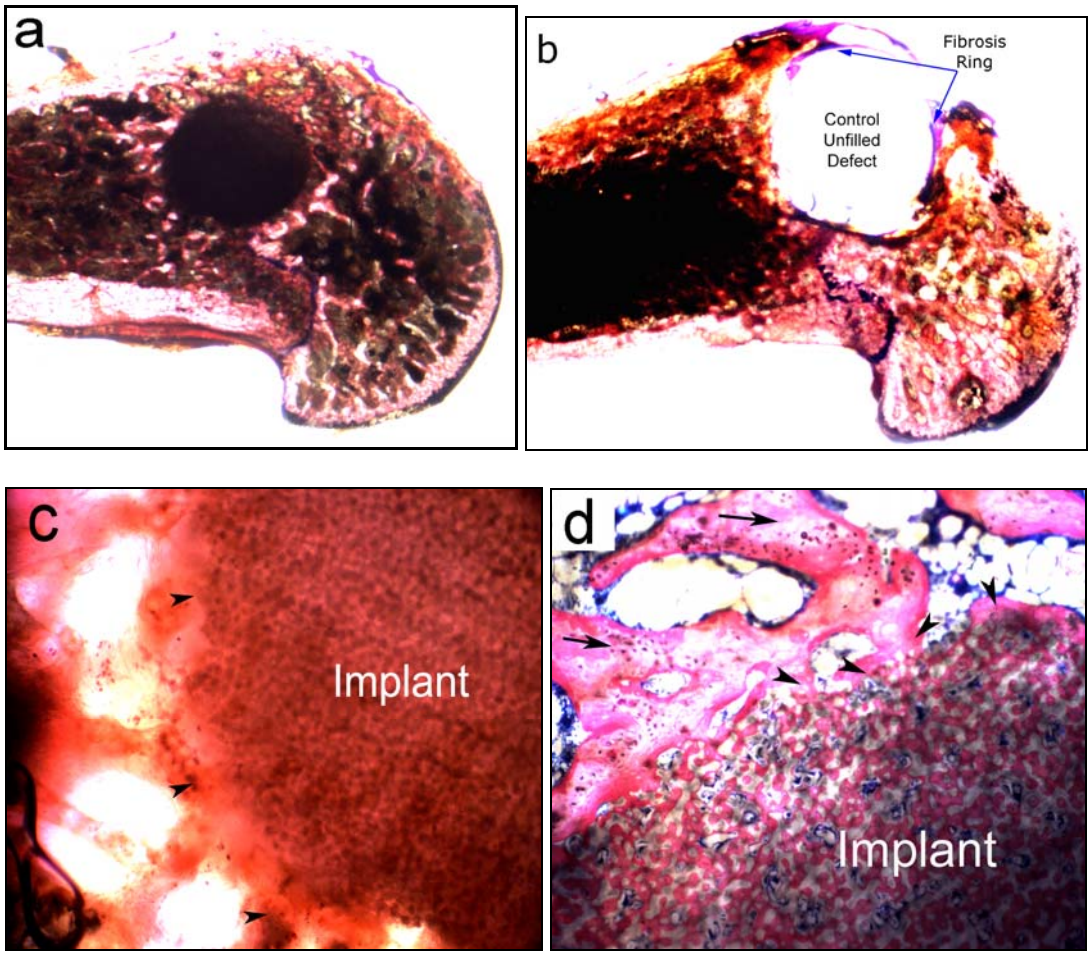

Figure 4-25. Histological sections after 6 weeks implantation: (a) β-TCMP implant in the femoral defect, (b) untreated control defect, (c) and (d) high magnification of the β-TCMP implant (small arrowheads show newly formed bone and black arrows indicate adjacent host bones).

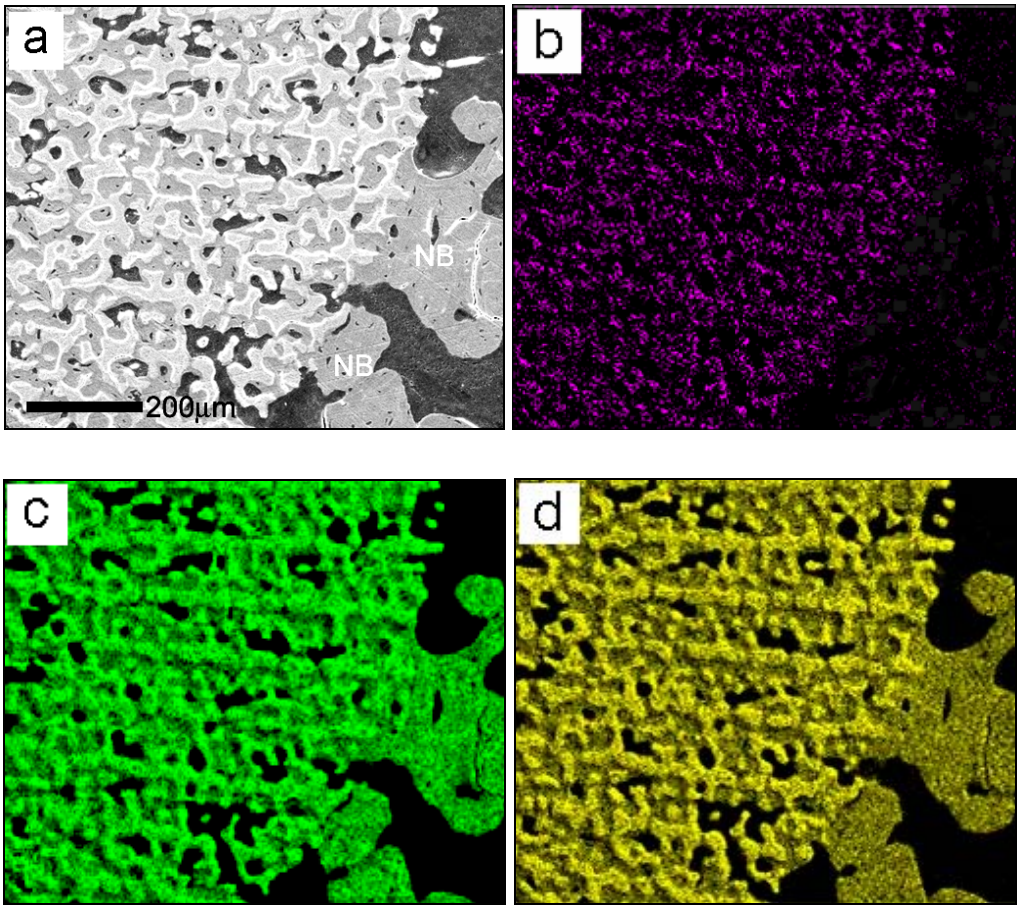

Figure 4-26. (a) Secondary electron image of a polished tissue section containing the β-TCMP implant after 6 weeks implantation (NB indicates newly formed bone) and related EDS mapping of (b) magnesium, (c) calcium and (d) phosphorus.

4.2.3 Conclusions

In this investigation, sea urchin spines were converted to resorbable Mg-substituted tricalcium phosphate (β-TCMP) by the hydrothermal reaction at relative low temperature ~180ºC, while maintaining the three-dimensional interconnected porous structure. The main conversion mechanism is the ion-exchange reaction; however, there is a secondary dissolution-reprecipitation reaction to form some amount of calcium

phosphate precipitates on the surfaces of the sample. The average compressive strength of converted spines is ~ 23 MPa, which is somewhat higher than that of cancellous bone (4 – 12 MPa). The sea urchin spines can be machined into different shapes for individual implant applications. *In-vivo* tests, in rat femoral defects for 6 weeks, show good bioactivity and osteoconductivity of these porous β-TCMP implants. There was no evidence of a fibrosis tissue ring around the implants, indicating that there was no loosening of the implants. New bone was found to grow up to and around the implants. Some new bone was found to migrate through the pores, starting from the outside of the implant through the pores at the edge of the implants. Growth of new bone into the center of the porous structure and the eventual resorption of β-TCMP sample may be expected in longer duration *in-vivo* experiments.

4.3 Conversion of coral and cuttlebone to porous calcium phosphates

Coral and cuttlebone are mainly composed of aragonite phases with a small amount of organic materials. Both coral and cuttlebone have three-dimensional macroporous structures (pore size > 50μm). In this vestigation, coral and cuttlebone were converted to HAP, while maintaining original porous structures. The interconnected macroporous structures of HAP products would allow good supply of blood and nutrients from the surrounding environment after the implantation. Macroporous HAP scaffolds support infiltration of bone cells and vessels, and finally encourage new bone ingrowth.

Coral and cuttlebone were converted to HAP by hydrothermal reaction in $(NH_4)_2HPO_4$ solution following Roy's work [89]. The main conversion took place as the following Equation (1):

(1) $10CaCO_3+6(NH_4)_2HPO_4+2H_2O \rightarrow Ca_{10}(PO_4)_6(OH)_2+6(NH_4)_2CO_3+4H_2CO_3$

The formation of β-TCP in some samples was considered to follow a dissolution-reprecipitaion mechanism.

4.3.1 Conversion of coral

Experimental

The starting materials are diammonium hydrogen phosphate [$(NH_4)_2HPO_4$, Fisher Scientific] and white coral, as shown in Figure 4-27. Small pieces of coral were collected, cleaned with deionized water and placed in the Parr 4843 reactor or autoclaves. The sample chamber was filled with a specified concentration of $(NH_4)_2HPO_4$ solution, sealed and heated at different temperatures, from 200°C to 250°C, for different durations. Coral samples can be completely converted at 250°C for 2 days.

Results and Discussion

The original coral is mainly composed of aragonite crystals (Figure 4-28a), which were converted to HAP with a small amount of β-TCP at 250℃ for 2 days (Figure 4-28b).

Figure 4-27. Photo of white coral used in the experiments.

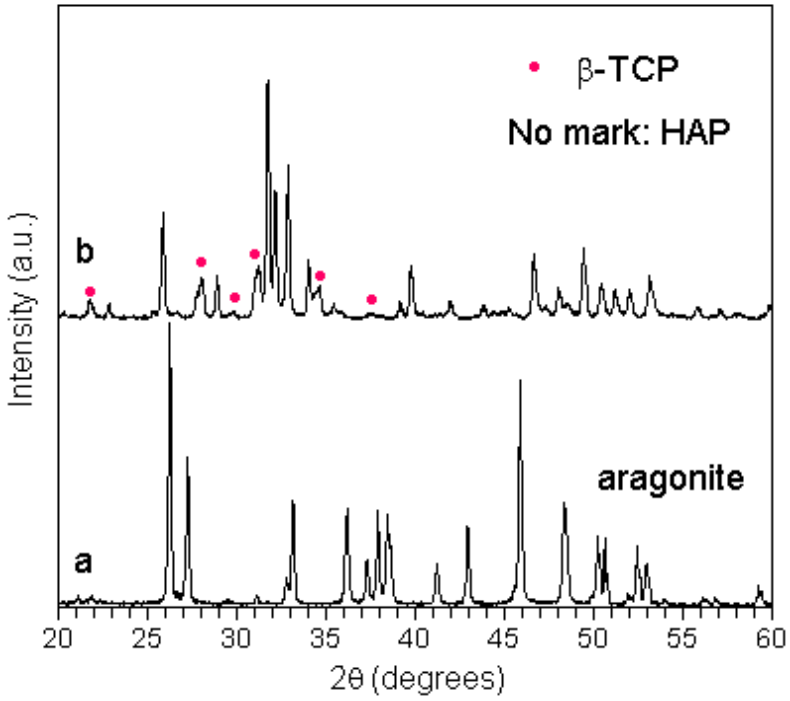

Figure 4-28. XRD results of (a) original coral, (b) coral converted at 250℃ for 2 days.

Figure 4-29a shows the interconnected porous structure of the original white coral (porosity ~40%). The pore size is about 100μm, which is large enough for tissue ingrowth [128, 129]. After conversion at 250℃ for 2 days, HAP scaffold (Figure 4-29b) maintains the interconnected macroporous structure of coral, indicating the conversion process follows the ion-exchange mechanism. However, HAP spheres assembled by HAP slices (Figure 4-29c) and HAP rods (Figure 4-29d) were found on the surfaces of the scaffold. A small amount of rhombohedral-shape particles (Figure 4-29d) was also found, which are believed to be β-TCP crystals, corresponding to XRD result (Figure 4-29b). These HAP and β-TCP particles are believed to form through the dissolution-reprecipitation process.

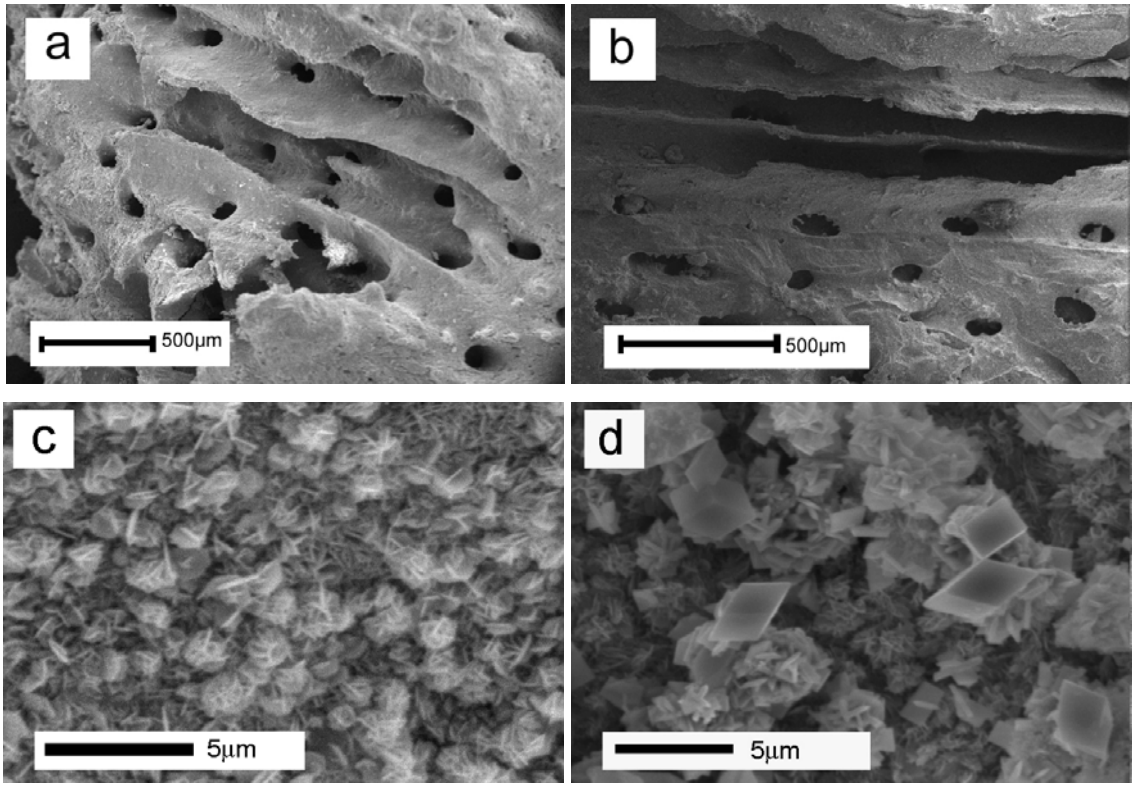

Figure 4-29. SEM images of original coral (a) and coral converted at 250℃ for 2 days: (b) main structure, (c) and (d) particles formed on the strut surfaces.

4.3.2 Conversion of cuttlebone

The cuttlefish, *Sepia officinalis* L., is a common demersal neritic species occurring predominantly near sandy and muddy bottoms up to a depth of 200m. Cuttlefish is abundant in the eastern Atlantic and in the Mediterranean Sea, which it is an important economic resource [130]. This species is one of the most studied cephalopods of the Old World, due to its availability from shallow costal waters, and the feasibility of its laboratory culture.

The cuttlebone, internal shell or bone of the cuttlefish, functions both as a skeletal structure and as a rigid buoyancy tank, enabling the cuttlefish to become more or less dense than sea water. The cuttlebone (~9% of the volume of the animal) is a hollow structure, divided by lamellae, containing both liquid and gas [131, 132]. The cuttlefish changes its density by varying the quantity of liquid within the porous structure of the bone [133].

In this investigation, cuttlebone samples were hydrothermally converted to HAP, while maintaining the original porous lamellar architecture.

Experimental

Diammonium hydrogen phosphate [$(NH_4)_2HPO_4$, Fisher Scientific] and cuttlebone were used as the starting materials. Whole cuttlebones (Figure 4-30) were bought from a local pet store. Small pieces of cuttlebone samples ($1\times1\times1$ cm^3 cubic) were cut from the whole cuttlebone and cleaned with deionized water. $(NH_4)_2HPO_4$ with the same weight as cuttlebone samples was dissolved in the teflon autoclave container.

Cuttlebone samples were then placed in the autoclave, which was filled with $(NH_4)_2HPO_4$ solution, sealed and heated at different temperatures, from 160°C to 200°C, for different durations. Cuttlebone samples were completely converted to HAP at 160°C for 8 hours.

Figure 4-30. Cuttlebone bought from a local store.

Results and Discussion

Cuttlebone is mainly composed of calcium carbonate associated with organic components (3-4.5% by weight) [131]. Bulk XRD from the cuttlebone sample (Figure 4-31a) indicates the matrix is mainly composed of the aragonite phase. After conversion at 160℃ for 2 hours (Figure 4-31b), most of the sample was converted to HAP with a small amount of aragonite phase remained. Cuttlebone sample was completely converted to HAP after reacted at 160℃ for 8 hours (Figure 4-31c).

The calcium carbonate matrix of the cuttlebone has an interconnected macroporous structure (Figure 4-32a). Porosity of cuttlebone is ~93%, and pore size is in the range of 200-400μm. After hydrothermal conversion at 160℃ for 8 hours, HAP scaffold still maintains the macroporous structure of the cuttlebone (Figure 4-32b). Many particles were found on the surfaces of the cuttlebone matrix after the conversion (Figure 4-32c), which are HAP particles (Figure 4-32d) formed through the dissolution-reprecipitaion process.

The disadvantage of the cuttlebone as an implant is the poor mechanical strength. Birchall *et al.* [131] reported the mean crushing strength of cuttlebone was 1.1±0.4 MPa and the flexural strength is 1.8±0.2 MPa. Therefore, the converted cuttlebone samples may only be used as small bone defect filler.

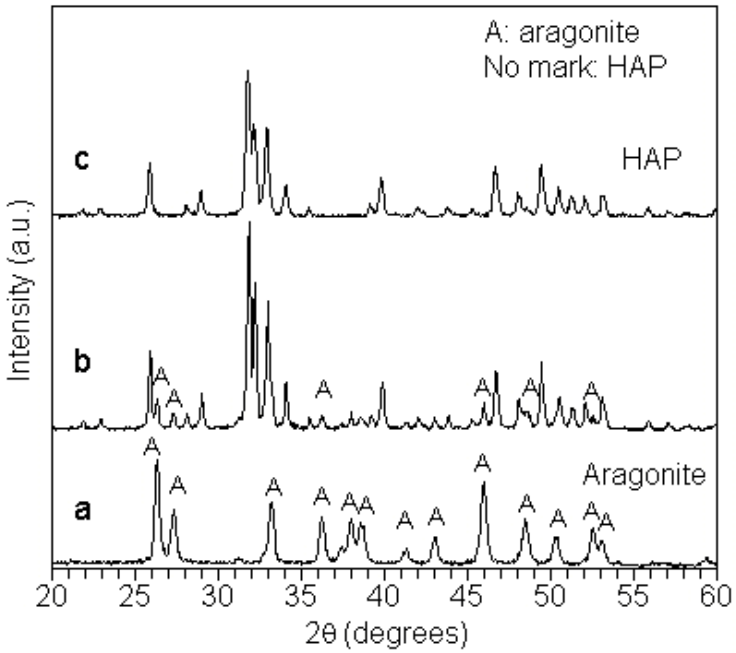

Figure 4-31. XRD pattern of original cuttlebone(a), cuttlebone converted at 160℃ for 2 hours (b), and for 8 hours (c).

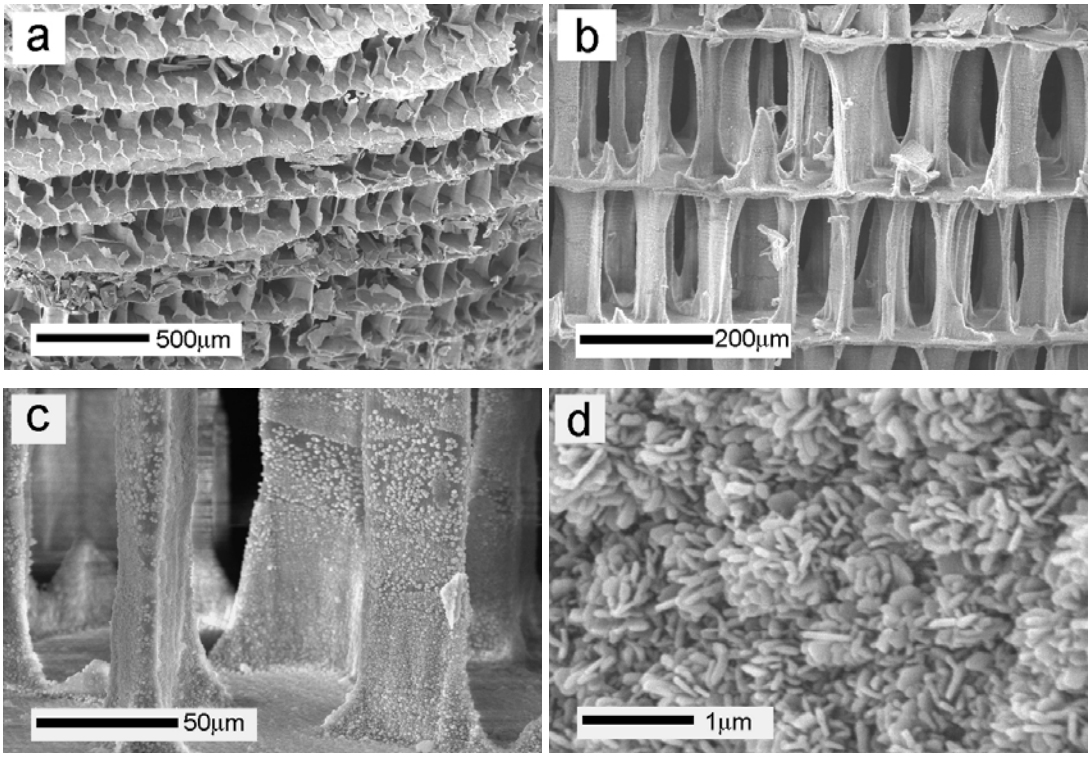

Figure 4-32. SEM images of (a) cuttlebone and (b), (c), (d) cuttlebone converted at 160℃ for 8 hours.

Acknowledgements

Chapter 4, in part, was a reprint of the materials in previous publications: 1. K.S. Vecchio, X. Zhang, J.B. Massie, M. Wang, C.W. Kim. *Acta Biomaterialia* 2007, 3:910-918; 2. K.S. Vecchio, X. Zhang, J.B. Massie, M. Wang, C.W. Kim. *Acta Biomaterialia* 2007; 3:785-793; 3. X. Zhang, K.S. Vecchio. *Materials Science and Engineering C* 2006; 26: 1445-1450.

5 PREPARATION OF HAP POWDERS

Hydroxyapatite ($Ca_{10}(PO_4)_6(OH)_2$, HAP) is similar to the major mineral phase of human bone. Due to its good biocompatibility and osteoconductivity, synthetic HAP has been widely used as bone graft substitutes, drug delivery devices and in purification of proteins [134-137]. Many methods have been developed to synthesize HAP powders. Among them, the hydrothermal method is often used to prepare HAP with good crystallinity and homogeneous size and shape, which can be achieved at low temperature [27, 138]. In this chapter, HAP rods were synthesized by hydrothermal method with a nucleation-growth mechanism. On the other hand, good crystalline HAP particles were prepared following a two-step method: wet precipitation and further hydrothermal treatment.

5.1 Hydrothermal synthesis of HAP rods

Recently, hydrothermal conversion of $CaCO_3$ materials, such as coral [89], seashells [65, 101, 102, 139] and aragonite or calcite crystals [65, 66] to HAP have been actively studied, and the conversion mechanisms: ion-exchange and dissolution-recrystallization, have been discussed. On the other hand, dicalcium phosphate anhydrous ($CaHPO_4$, DCPA) or dihydrate ($CaHPO_4 \cdot 2H_2O$, DCPD) is known to be a nucleation precursor, in aqueous solutions, for apatitic calcium phosphates. The hydrolysis of DCPA or DCPD in different solutions to HAP has been discussed [140-142]. However, the hydrothermal reaction of DCPA and $CaCO_3$, both of which have low solubility, has not been reported.

In this investigation, hydrothermal reactions between DCPA and calcium carbonate chemical (calcite polymorph of $CaCO_3$) or cuttlebone (aragonite polymorph of $CaCO_3$) were performed from 120ºC to 180ºC for different durations. After hydrothermal reaction above 140ºC for 24 hours, most products are HAP rods with a small amount of β-tricalcium phosphate (β-TCP) as a byproduct. Large HAP rods have been confirmed to have higher affinity for proteins than nano-sized ones and good potential applications in liquid chromatography [143-145]. Furthermore, whisker and/or rod-like HAP have been used as reinforcement to increase the fracture toughness of HAP ceramics [27, 146, 147].

The nucleation and growth morphology of HAP in relation to the reactants was studied, and the growth mechanisms of HAP rods are discussed. Strong evidence for a nucleation-growth process is presented.

5.1.1 Experimental procedure

The starting reactant materials were dicalcium phosphate anhydrous (DCPA, Fisher Scientific, USA), $CaCO_3$ chemical (calcite polymorph of $CaCO_3$, EM Science, USA) and cuttlebone powder (aragonite polymorph of $CaCO_3$). The cuttlebone powder was made from the inner part of the cuttlebones, heated at 200ºC for 4 hours and then cleaned with deionized water to eliminate any organic materials. In this paper, "calcite" will be used for the "$CaCO_3$ chemical" and "aragonite" for the "cuttlebone powder".

Calcite or aragonite (0.80g) and DCPA (1.64g) were homogeneously mixed with 30ml-deionized water in a teflon container. The container was then sealed in an

autoclave, which was heated at specified temperatures from 120ºC to 180ºC for various times. The resulting products in the form of powders in the container were collected, rinsed with deionized water, and dried at 80ºC, prior to examination.

5.1.2 Results and discussion

Figure 5-1 shows the XRD pattern of the original dicalcium phosphate anhydrous (DCPA, spectrum 'a' in Figure 5-1, JCPDF #9-0080) and $CaCO_3$ sources, cuttlebone powder (spectrum 'b' in Figure 5-1) and $CaCO_3$ chemical (spectrum 'c' in Figure 5-1). The cuttlebone powder is composed of an aragonite polymorph (JCPDF #5-0453), while $CaCO_3$ chemical is composed of a calcite polymorph (JCPDF #5-0586) of $CaCO_3$. The miller indices of the peaks of the specific phase are marked in the pattern.

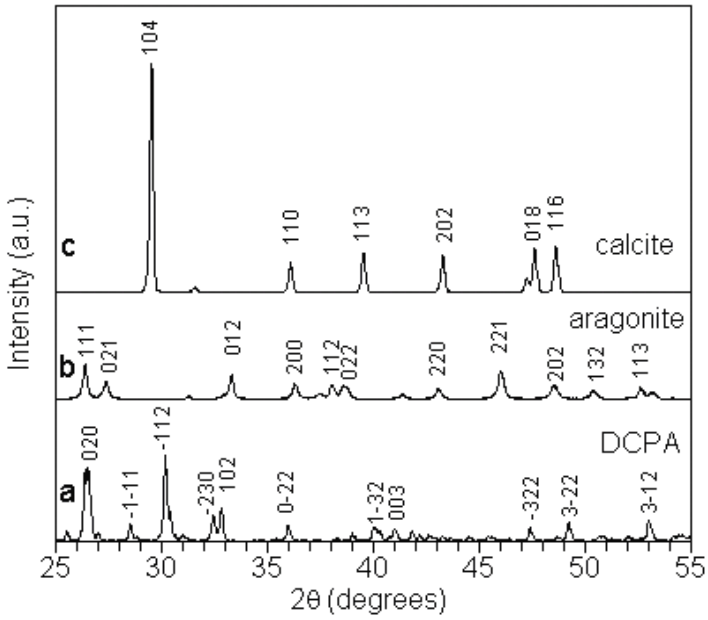

Figure 5-1. XRD pattern of (a) DCPA, (b) cuttlebone powder and (c) $CaCO_3$ chemical.

The XRD patterns of products prepared by hydrothermal reaction of DCPA and calcite at different temperatures are shown in Figure 5-2. After hydrothermal reaction at 120ºC for 24 hours (spectrum 'a' in Figure 5-2), a small peak from calcite [c(104)] was found, which indicates a small amount of calcite remained, although most starting materials reacted to produce HAP (JCPDF #9-0432) and a limited amount of β-TCP (JCPDF #9-0169). Hydrothermal reactions at 140ºC (spectrum 'b' in Fig. 2) and 180ºC (spectrum 'c' in Figure 5-2) for 24 hours were more complete. No peaks from the starting materials were found in these patterns. The final products were composed of HAP crystals, with a small amount of β-TCP crystals.

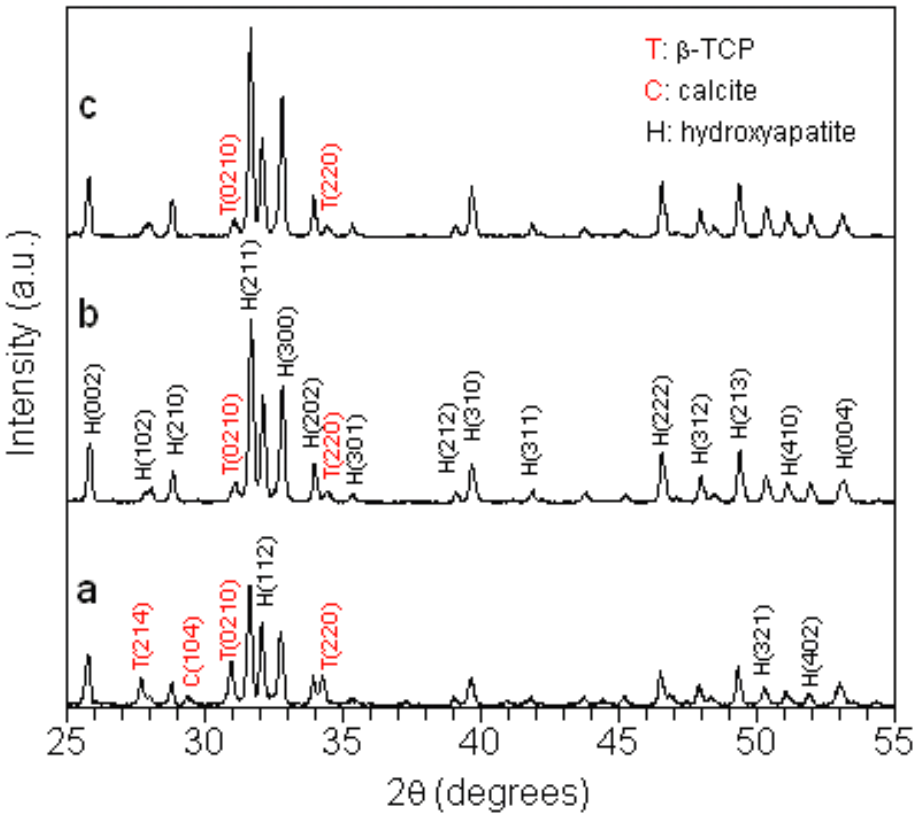

Figure 5-2. XRD pattern of products prepared by hydrothermal reaction of DCPA and calcite at different temperatures: (a) 120ºC, (b) 140ºC and (c) 180ºC, each for 24 hours.

Figure 5-3 shows the XRD patterns of products prepared from DCPA and aragonite at different temperatures, which produced similar results to the reactions between DCPA and calcite. After the hydrothermal reaction at 120ºC for 24 hours (spectrum 'a' in Figure 5-3), peaks from DCPA were still found in the pattern. Hydrothermal reactions at higher temperatures (spectrum 'b' and 'c' in Figure 5-3) were more complete resulting in the formation of HAP.

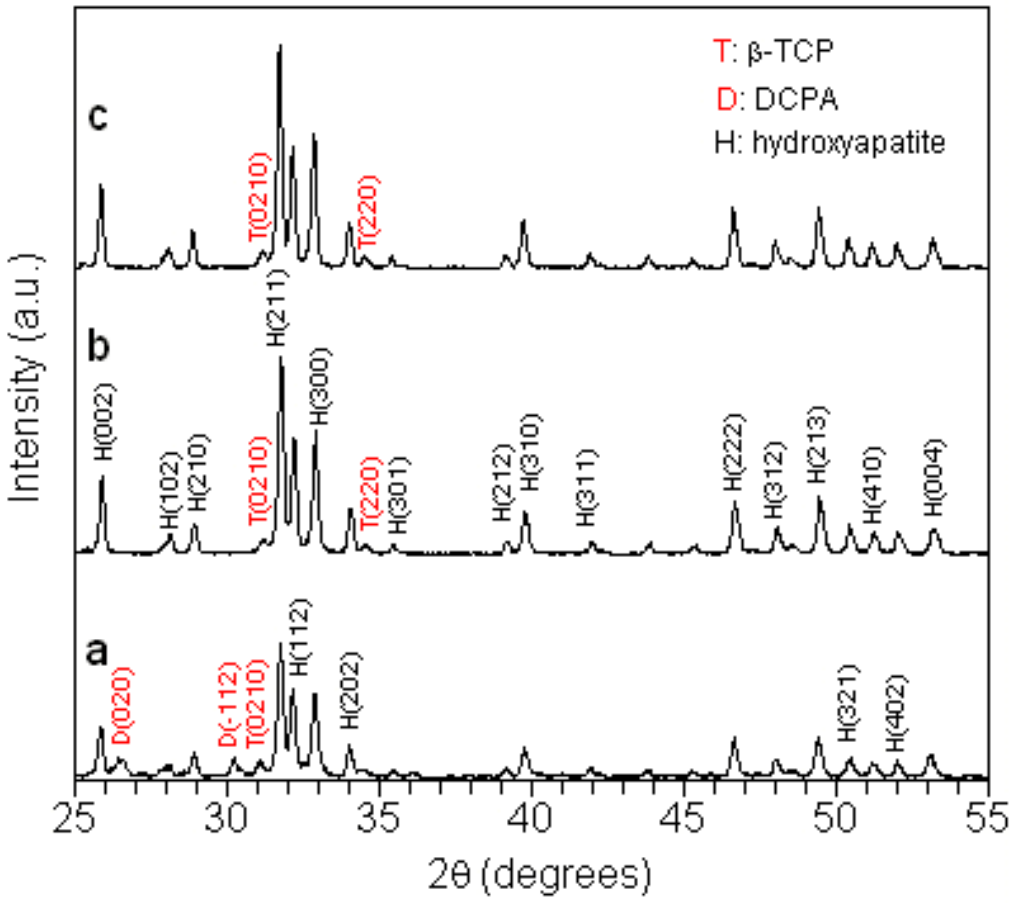

Figure 5-3. XRD pattern of products prepared by hydrothermal reaction of DCPA and aragonite at different temperatures: (a) 120ºC, (b) 140ºC and (c) 180ºC, each for 24 hours.

For comparison, a sample of 1.64g DCPA alone was mixed with 30ml deionized water, put in the autoclave, and heated at 140ºC for 24 hours. No new products were found, and only the starting material, DCPA, was recovered. This indicates no obvious hydrolysis of DCPA to HAP, due to the relatively low solubility of DCPA in this condition, and thus water alone is not sufficient to drive the conversion of DCPA to HAP [142]. However, Ca^{2+} ions [142], CO_3^{2-} ions [140] and $CaCO_3$ [148] were reported to facilitate the hydrolysis of DCPA or DCPD to HAP. Therefore, DCPA reacts with $CaCO_3$ to produce HAP and β-TCP in our experimental conditions. Equations (3) and (4), are suggested as reactions to synthesize HAP ($Ca_{10}(PO_4)_6(OH)_2$) and β-TCP ($Ca_3(PO_4)_2$).

(3) $6CaHPO_4 + 4CaCO_3 + 2H_2O \rightarrow Ca_{10}(PO_4)_6(OH)_2 + 4H_2CO_3$

(4) $2CaHPO_4 + CaCO_3 \rightarrow \beta\text{-}Ca_3(PO_4)_2 + H_2CO_3$

Figure 5-4 shows the XRD pattern of products after the hydrothermal reaction of DCPA and calcite at 140ºC for different times. After 1 hour of reaction (spectrum ‘a’ in Figure 5-4), only peaks from the starting materials, DCPA and calcite, are found in the pattern. After reaction for 1.5 hours (spectrum ‘b’ in Figure 5-4), a small amount of β-TCP can be found in the recovered sample. No peak from HAP was found in the pattern. After 2 hours of reaction (spectrum ‘c’ in Figure 5-4), significant amounts of HAP and β-TCP were found and some calcite and DCPA crystals were still present. The intensity ratio between β-TCP (0210) peak and HAP (211) peak (marked with T(0210) and H(211) in Figure 5-4), $I_{\beta\text{-TCP}\,(0210)}/I_{\text{HAP}\,(211)}$, calculated from the spectrum ‘c’ in Fig. 4 is

about 1.6. With increasing reaction time (spectra 'b-e' in Figure 5-4), the amount of calcite and DCPA decreased. The intensity ratio, $I_{\beta\text{-TCP }(0210)}/I_{\text{HAP }(211)}$, also decreased with increasing reaction time, indicating that HAP phase is the preferred phase over β-TCP. After 24 hours of reaction (spectrum 'e' in Figure 5-4), no peaks from calcite or DCPA can be found in the pattern, and the $I_{\beta\text{-TCP }(0210)}/I_{\text{HAP }(211)}$ ratio is about 0.1. These results indicate that some amount of β-TCP easily formed at the beginning of the reaction, but that increasing amounts of HAP formed from the starting materials with increasing reaction time and that β-TCP may dissolve back into solution.

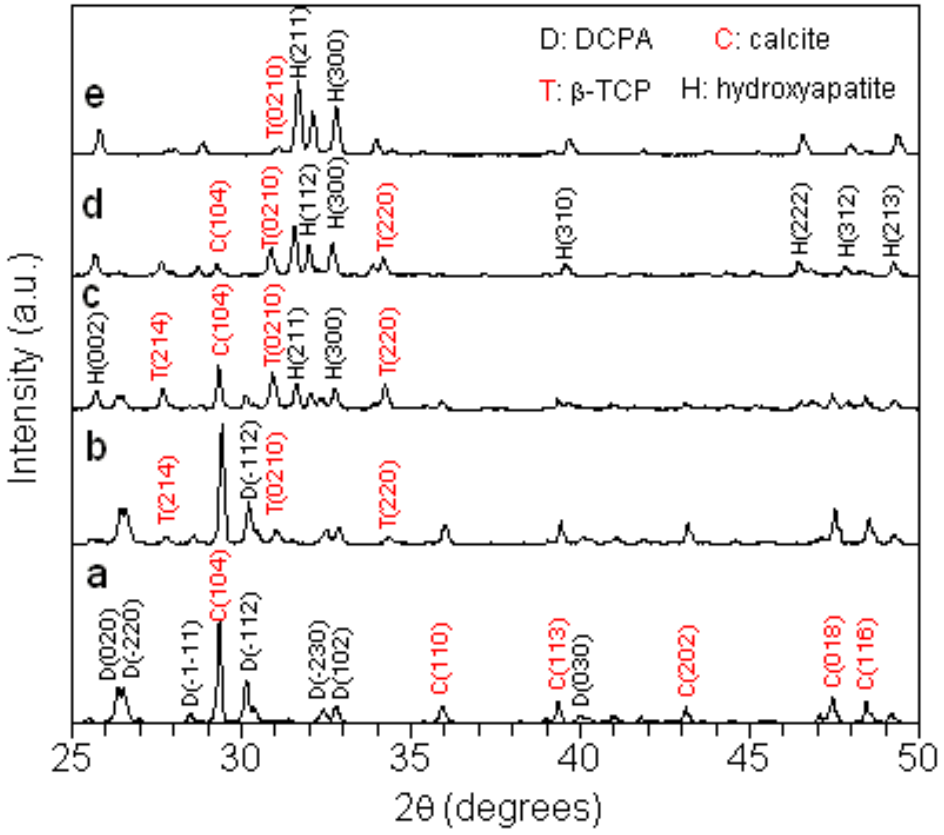

Figure 5-4. XRD pattern of products prepared by hydrothermal reaction of DCPA and calcite at 140ºC for (a) 1 hour, (b) 1.5 hours, (c) 2 hours, (d) 8 hours, and (e) 24 hours.

Figure 5-5 shows the XRD pattern of products after hydrothermal reaction of DCPA and aragonite at 140ºC for different times. After 1 hour of reaction (spectrum 'a' in Figure 5-5), a peak from HAP [H(211)] was found. After 1.5 hours of reaction (spectrum 'b' in Figure 5-5), most of the products are HAP and a small amount of β-TCP exists. The reaction was completed after 24 hours of reaction (spectrum 'e' in Figure 5-5). The x-ray peak ratio, $I_{\beta\text{-TCP }(0210)}/I_{\text{HAP }(211)}$ was also found to decrease with increasing reaction time (spectra 'b-e' in Figure 5-5), as more starting materials reacted to produce HAP. Comparing the reaction of DCPA and aragonite with that of DCPA and calcite, the formation of HAP from aragonite is faster than from calcite, and a much smaller amount of β-TCP was found in the aragonite reaction.

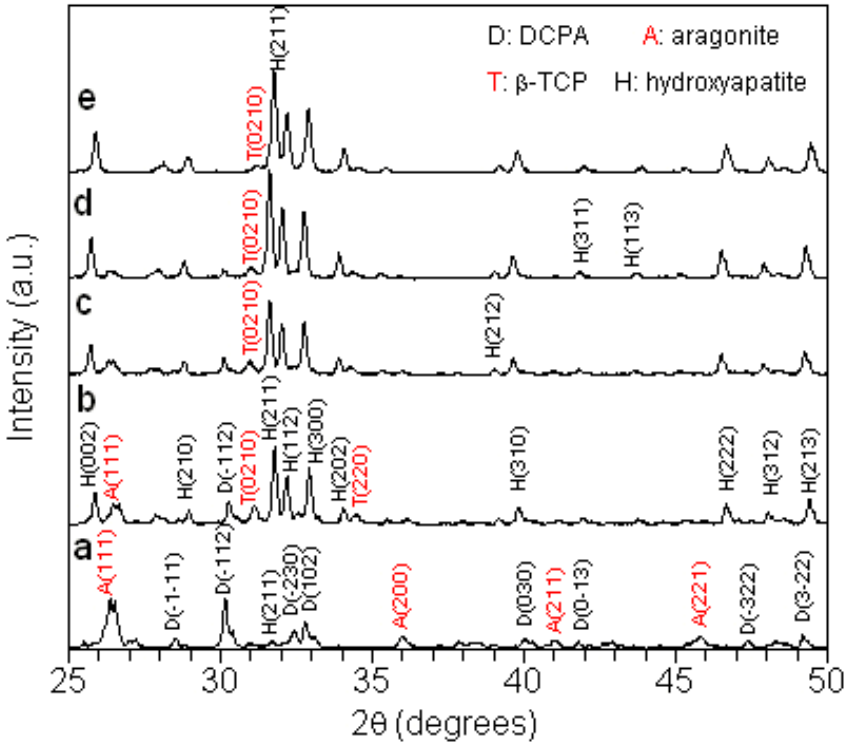

Figure 5-5. XRD pattern of products prepared by hydrothermal reaction of DCPA and aragonite at 140ºC for (a) 1 hour, (b) 1.5 hours, (c) 2 hours, (d) 8 hours, and (e) 24 hours.

SEM images of the products synthesized from DCPA and calcite at 140ºC for various times and the related EDS spectra are shown in Figure 5-6. After the reaction at 140ºC for 1 hour, some calcite particles and DCPA particles remained (Figure 5-6a). The EDS spectrum from DCPA particles (Figure 5-6i) shows the characteristic peaks of calcium, oxygen, and phosphorus, and the EDS spectrum from the calcite portion (Figure 5-6j) shows the characteristic peaks of calcium, carbon, and oxygen. After the reaction at 140ºC for 1.5 hours, some tiny HAP rods grew on DCPA particles (Figure 5-6b), and grew larger after 2 hours reaction (Figure 5-6d). Many small particles formed on the surface of calcite particles after 1.5 hours reaction (Figure 5-6c), which are believed to be β-TCP, based on the XRD result (spectrum 'b' in Figure 5-4), which indicates a small amount of β-TCP formed in this reaction. Portions of the calcite particles dissolved after this reaction. More β-TCP particles growing on calcite and the obvious dissolution of calcite were found after 2 hours reaction (Figure 5-6e). The growth of small HAP rods out of β-TCP particles, which act as the nuclei, was also found in Figure 5-6c and Figure 5-6e. After the reaction for 4 hours (Figure 5-6f) and 8 hours (Figure 5-6g), more HAP rods were found and grew larger with the depletion of the reactants, DCPA and calcite. The reaction was complete at 140ºC after 24 hours, corresponding to the XRD result (spectrum 'e' in Figure 5-4), and most products are HAP rods (Figure 5-6h), which are several microns in length.

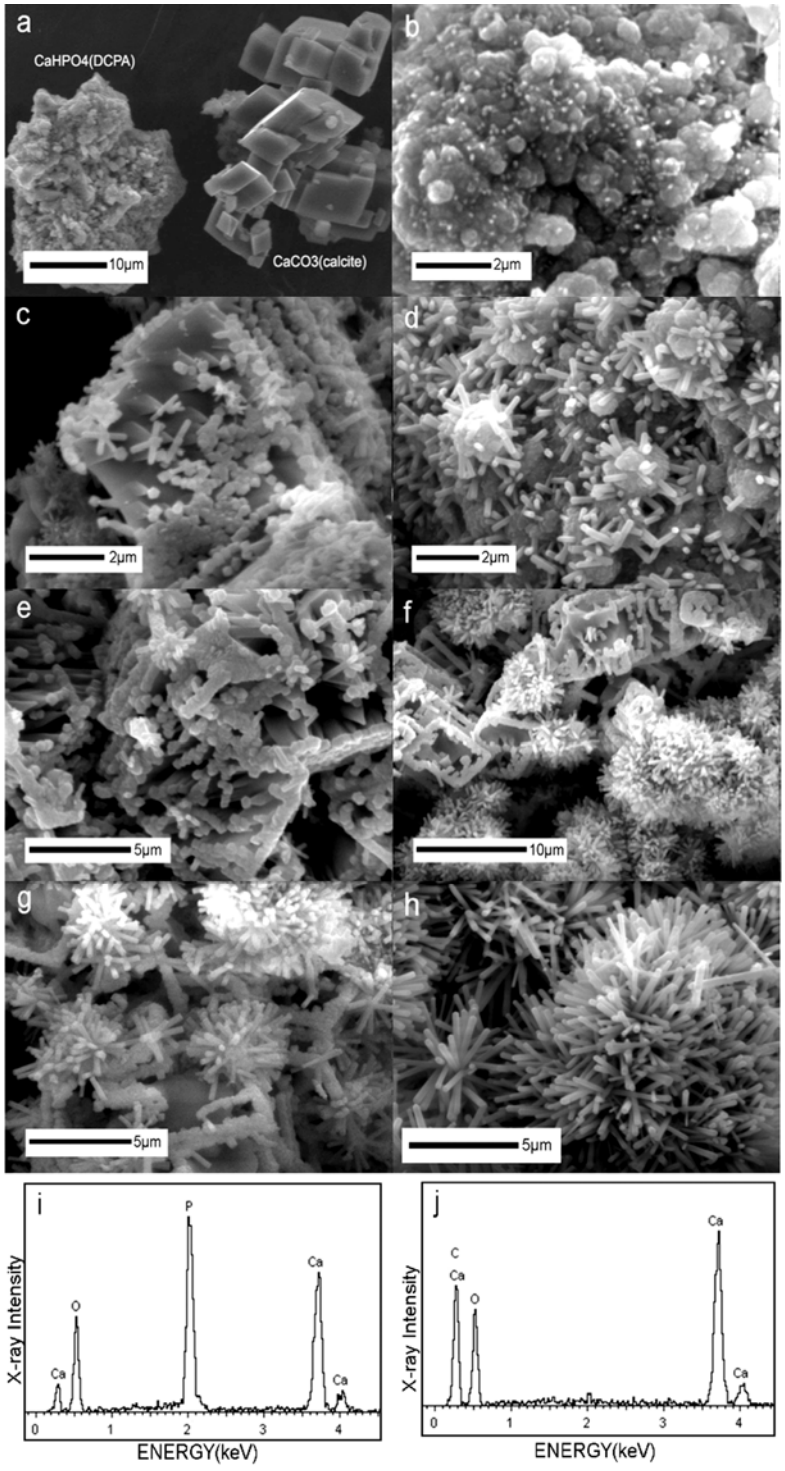

Figure 5-6. SEM images of products from hydrothermal reaction of DCPA and calcite at 140ºC for (a) 1 hour, (b) 1.5 hours (DCPA portion), (c) 1.5 hours (calcite portion), (d) 2 hours (DCPA portion), (e) 2 hours (calcite portion), (f) 4 hours, (g) 8 hours, and (h) 24 hours and EDS spectrum of (i) DCPA and (j) calcite.

The synthesis of HAP is thought to follow a nucleation and growth process. First, some small amount of calcite and DCPA dissolve to form ions in the water. With increasing reaction time, two different processes occur on calcite and DCPA particles, respectively. On calcite particles, β-TCP (a =b= 10.43Å, c = 37.38Å, γ = 120°), which has the same space group, $R\bar{3}C$, as calcite (a = b=4.99Å, c = 17.06Å, γ = 120°), nucleates on the calcite. Some HAP rods are found to grow out of β-TCP particles, which act as the nuclei. On DCPA particles, HAP directly nucleates and grows over the surfaces, which is the main nucleation-growth mechanism for formation of HAP. The formation of specific hexagonal rod-shape morphology is due to the hexagonal crystallographic nature of HAP (a= b=9.432 Å, c=6.881 Å, γ = 120°), which has a space group, $P6_3/m$ [149], and the slow nucleation-growth process in the experimental conditions. The concentration of calcium and phosphate ions in the solution are so low, because of the low solubility of DCPA (Ksp =1×10^{-7} at 25ºC) and calcite (Ksp =3.36×10^{-9} at 25ºC), that HAP can grow slowly and preferably along c-axis and form the hexagonal shape in the hydrothermal conditions [65, 150-152].

With increasing reaction time, more β-TCP particles grow on the surface of calcite. However, the formation of β-TCP slows down eventually, which may be caused by the surface coverage of calcite particles by β-TCP particles and the dissolution of calcite, which limit the available nucleation sites for β-TCP. On the other hand, more HAP, which has much lower solubility (Ksp = 3.2×10^{-58} at 25ºC) than that of β-TCP (Ksp = 1.20×10^{-29} at 25ºC) [28], grow larger into rod-shape particles on DCPA particles. After

reaction at 140ºC for 24 hours, HAP rods grow to several microns in length coupled to the depletion of the starting materials with increasing the reaction time.

Figure 5-7 shows SEM images of HAP rods prepared by hydrothermal reaction between DCPA and aragonite at 140ºC for different times. After the reaction for 1 hour (Figure 5-7a-c), small HAP rods, consistent with the XRD result (spectrum 'a' in Figure 5-5), grew over the surface of DCPA particle (Figure 5-7b) and on some sites of aragonite particles (Figure 5-7c). After 1.5 hours reaction, HAP rods grew across the entire surface of DCPA (Figure 5-7d) and also more HAP rods formed on aragonite (Figure 5-7e). With increasing reaction time (Figure 5-7f and Figure 5-7g), more HAP grew with the depletion the starting materials, DCPA and aragonite. The reaction was completed after 24 hours (Figure 5-7h), consistent with the XRD result (spectrum 'e' in Figure 5-5). XRD results (spectra 'b-e' in Figure 5-5) also indicate a small amount of β-TCP formed in the reactions, which could not be identified in the SEM images, due to the fast formation of a large amount of HAP rods in this process. The formation of HAP rods in this reaction is observed to follow a similar nucleation and growth process as that for the reaction of DCPA and calcite. HAP nucleates and grows mainly on DCPA particles, while a smaller amount of HAP rods form on aragonite particles. In both reactions, dissolution of β-TCP may feed ions into solution facilitating further HAP formation, consistent with the steady level of β-TCP present, suggesting a balance between its formation and its dissolution is necessary.

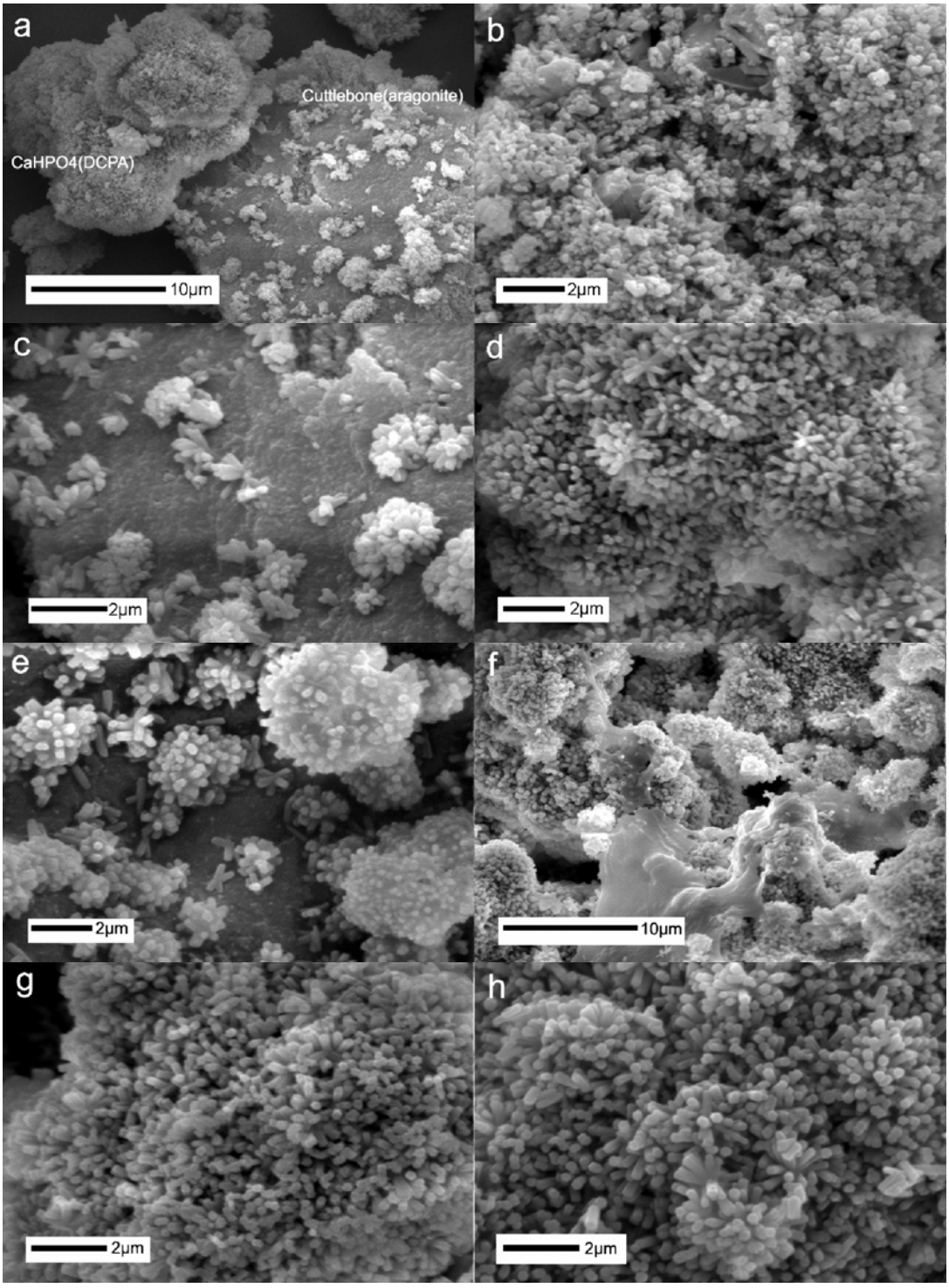

Figure 5-7. SEM images of HAP rods prepared by hydrothermal reaction from DCPA and cuttlebone (polycrystalline aragonite) at 140ºC for (a) 1 hour, (b) DCPA portion and (c) aragonite portion in (a), (d) 1.5 hours (DCPA portion), and (e) 1.5 hours (aragonite portion), (f) 4 hours, (g) 8 hours, and (h) 24 hours.

Figure 5-8 shows TEM images of HAP rods synthesized by hydrothermal reactions of DCPA and calcite (Figure 5-8a-c) or aragonite (Figure 5-8d) at 140ºC for 2 hours. HAP rods, which grew out of a common nucleation site, can be observed. Figure 5-8d shows two HAP rods with their smaller ends attached to each other, which grew from the same nucleating crystallite. All the HAP rods observed had widths of ~200nm. The nucleating site is primarily the DCPA particles in both cases.

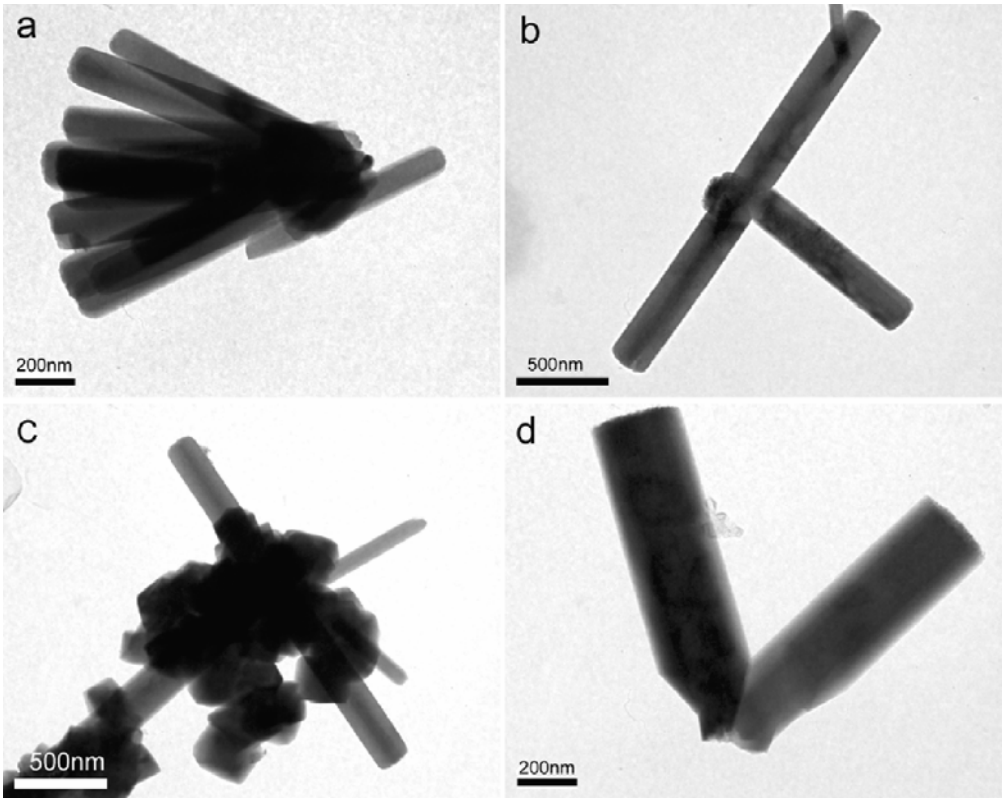

Figure 5-8. TEM images of the products synthesized from the hydrothermal reaction of DCPA with calcite (a, b and c) and with aragonite (d) at 140ºC for 2 hours.

5.1.3 Conclusions

HAP rods, with a small amount of β-TCP as a byproduct, were synthesized by the hydrothermal reaction of dicalcium phosphate anhydrous (DCPA) and cuttlebone powder (aragonite polymorph of $CaCO_3$) or $CaCO_3$ chemical (calcite polymorph of $CaCO_3$) from 120ºC to 180ºC for different durations. The synthesis is observed to be a nucleation-growth process. Both DCPA and calcium carbonate provide ion sources to the solution for the nucleation and growth of HAP.

For the reaction of DCPA and calcite, the nucleation and growth of HAP rods mainly occurred on DCPA particles. The formation of specific hexagonal rod-shape morphology is due to the hexagonal crystallographic nature of HAP and the slow nucleation-growth process in the experimental conditions. The concentration of calcium and phosphate ions in the solution are low, because of the low solubility of DCPA and calcite, that HAP can grow slowly and preferably along its c-axis and form the hexagonal shape in the hydrothermal conditions. β-TCP, which has the same space group, $R\bar{3}C$, as calcite, nucleated and grew on the surface of calcite particles at the beginning of the reaction. Some HAP rods were also found to grow out of β-TCP particles. With increasing reaction time, the formation of β-TCP slowed down. On the other hand, HAP, which has a much lower solubility, grew larger into rod-shape particles on DCPA with the depletion of the starting materials. For the reaction of DCPA and aragonite, HAP also mainly nucleated and grew on DCPA particles, while a smaller amount of HAP rods formed on aragonite particles. A small amount of β-TCP was also found as a byproduct in this reaction.

Large HAP rods synthesized in the experiments have potential applications for protein purification in liquid chromatography and can be used to increase the fracture toughness of HAP ceramics.

5.2 Preparation of HAP by a two-step method

Wet precipitation is a simple way to prepare HAP powders. However, most products prepared directly from precipitation at low temperature are calcium-deficient HAP with relatively poor crystallinity. In this investigation, good crystalline HAP was prepared by a two-step method. First, HAP was precipitated from $(NH_4)_2HPO_4$ and $Ca(NO_3)_2$ solution at 80℃. The precipitate was then hydrothermal treated 140℃ for 24 hours to improve crystallinity.

5.2.1 Experimental

Calcium nitrate tetrahydrate [$Ca(NO_3)_2{\cdot}4H_2O$, ACS reagent, Sigma-Aldrich], ammonium phosphate dibasic [$(NH_4)_2HPO_4$, reagent grade, Sigma-Aldrich] were used as starting reagents, for calcium and phosphorus sources, respectively. The precipitation was performed with an auto-titration machine shown in Figure 5-9. 200mL 0.2M $Ca(NO_3)_2$ solution were prepared in a 600mL beaker, which was kept at 80℃ in the water bath. 100mL 0.24 M $(NH_4)_2HPO_4$ solution was slowly titrated into $Ca(NO_3)_2$ solution with the final Ca/P molar ratio of 1.67 in the mixture. NH_4OH solution (0.01M) was used to controlled pH of the mixture ~9.

After precipitation, the product was aged for 1 hour at 80℃, and then hydrothermally treated at 140℃ for 24 hours. The product was then collected, rinsed with deionized water and dried at 100℃ overnight.

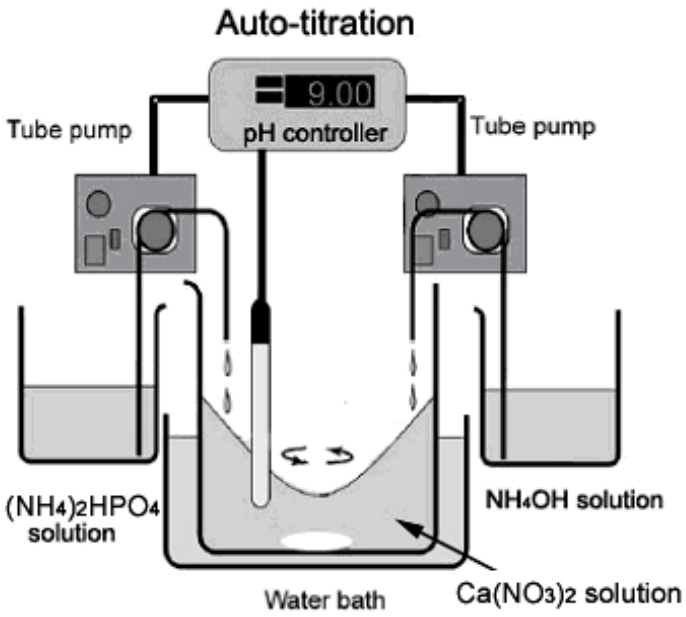

Figure 5-9. Schematic drawing of auto-titration used for wet precipitation.

5.2.2 Results

Figure 5-10 shows the XRD pattern of as-prepared powder by the two-step method, which indicates the good crystallinity of HAP product. The precipitation reaction took place as the following Equation (5):

(5) $6(NH_4)_2HPO_4+10Ca(NO_3)_2+8NH_4OH \rightarrow Ca_{10}(PO_4)_6(OH)_2+20NH_4NO_3+6H_2O$

SEM images (Figure 5-11a and Figure 5-11b) show that HAP aggregates prepared by this method ranges from several to tens of micrometers. These aggregates are assembled by small particles (Figure 5-11b).

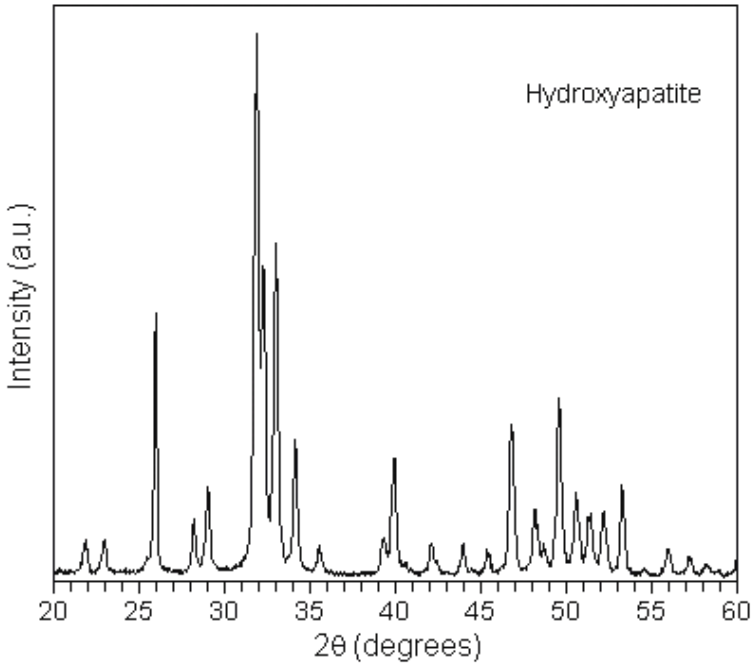

Figure 5-10. XRD pattern of HAP powder prepared by the two-step method.

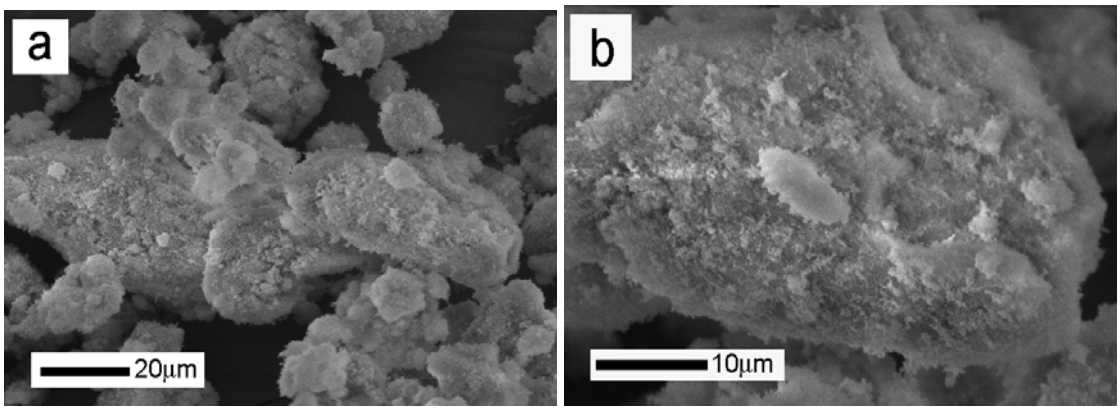

Figure 5-11. SEM images HAP particles prepared by the two-step method.

Acknowledgements

Chapter 5, in part, was a reprint of the materials in the previous publication: X. Zhang, K.S. Vecchio. *Journal of Crystal Growth* 2007, 308:133-140.

6 BETA-TRICALCIUM PHOSPHATE CERAMICS

Tricalcium phosphate [$Ca_3(PO_4)_2$, TCP] ceramics, especially β-TCP, are currently used for a number of dental and skeletal prosthetic applications due to their good biocompatibility, bioresorbability and osteointegration properties [113-118]. TCP can exist under three polymorphs [91, 153]: (i) β-TCP is stable below 1120℃; its space group is $R\bar{3}c$ and room temperature density is 3.07 $g \cdot cm^{-3}$. (ii) α-TCP is stable from 1120 to 1470℃, but can be quenched to room temperature as a metastable phase. Its space group is $P2_1/a$, and its room temperature density is 2.86 $g \cdot cm^{-3}$. (iii) α'-TCP is stable from 1470℃ to the melting point at 1756℃. Recently, Yashima and Sakai [154] reported that the space group of α'-TCP is $P\bar{3}m$.

Both β- and α-TCP have been widely used as synthetic bone substitutes. β-TCP products usually are resorbed by the host tissue in ~3-6 months after implantation. The resorbability of β-TCP products make it desirable as temporary scaffolds for new bone growth and finally replaced by newly formed bone. However, due to the poor mechanical strength, β-TCP products can only be used as filling materials for bone defects.

In this chapter, β-TCP powders with/without Mg substitution were prepared. With Mg substitution, the β- to α-TCP transition temperature increases. Highly dense β-TCMP ceramics (~99.4%) were produced by sintering the green bodies at 1250℃. Interconnected macroporous β-TCMP ceramics were fabricated both by the extrusion method with sucrose as the porogen, and by the replication mehod using polyurethane

foam. β-TCMP ceramics with porous structure in the center and a dense structural shell to mimic human bone were also created.

6.1 Dense β-TCP or β-TCMP ceramics

Highly dense β-TCP ceramics is hard to prepare, due to insufficient compaction when sintering below the β- to α-TCP transition temperature [90, 91]. Above the transition temperature, β- to α-TCP transformation causes the expansion of TCP during the sintering process and creates micro-cracks in the ceramics, which prevents TCP ceramics from further densification [92, 93].

In this investigation, β-TCP powders with/without Mg substitution were produced. With the increase of Mg^{2+} content in β-TCMP [$(Ca,Mg)_3(PO_4)_2$], the β- to α-TCP transition temperature increases [76, 91, 155, 156]. β-TCMP with 3mol% Mg^{2+} has the transition temperature above 1300℃. Dense β-TCMP ceramics can be produced by pressing ceramic green bodies at 100MPa and further sintering above 1150℃ for 2 hours. Quasi-static compression tests of dense β-TCP and β-TCMP ceramics were performed to evaluate the mechanical strength of these ceramics. Due to the presence of Mg in calcified living tissues (about 0.5% in bone or tooth enamel and more than 1% in tooth dentine [157]), β-TCMP prepared in this investigation, may have improved biological functions [158-160], and potential applications in bone and tooth replacement and augmentation .

6.1.1 Experimental

Synthesis of β-TCP and β-TCMP powders

Calcium nitrate tetrahydrate [$Ca(NO_3)_2 \cdot 4H_2O$, ACS reagent, Sigma-Aldrich], magnesium nitrate hexahydrate [$Mg(NO_3)_2 \cdot 6H_2O$, ACS reagent, Sigma-Aldrich] and ammonium phosphate dibasic [$(NH_4)_2HPO_4$, reagent grade, Sigma-Aldrich] were used as starting reagents, for calcium, magnesium and phosphorus, respectively.

The calcium nitrate solution was titrated into $(NH_4)_2HPO_4$ solution with continuous stirring (~700 rpm) and controlling final molar ratio of Ca/P as 1.5. $(NH_4)_2HPO_4$ solution was adjusted to pH ~10 before the titration and kept at pH ~9 during the titration with ammonium hydroxide solution. The precipitate (apatitic tricalcium phosphate) was rinsed with deionized water, separated by centrifuge and dried at 100℃ overnight. For β-TCMP, a predetermined amount of $Mg(NO_3)_2 \cdot 6H_2O$ as the Mg^{2+} source was dissolved in $Ca(NO_3)_2$ solution before the titration, and the final molar ratio of (Ca+Mg)/P is 1.5. The Mg content in the β-TCMP sample is calculated by the molar percentage of $Mg^{2+}/(Ca^{2+}+Mg^{2+})$ from the starting reagents. Hereafter, β-TCMP samples with 2 mol%, 3 mol%, 4 mol%, 5 mol%, 10 mol% Mg^{2+} in this investigation are designated as β-TCMP-2, β-TCMP-3, β-TCMP-4, β-TCMP-5 and β-TCMP-10, respectively.

The dried precipitate (β-TCP or β-TCMP precursor) was calcined at 800℃ in air for 3 hours to produce β-TCP or β-TCMP.

Ceramic sintering

Certain amount of β-TCP or β-TCMP powder was ground with several drops of 5 wt.% polyvinyl alcohol (PVA) solution in the mortar. The powder mixture was

uniaxially pressed in a stainless steel die on a load frame at 100 MPa to create compact green bodies. Green bodies were then sintered above 1100℃ in a muffle furnace in air, with a heating rate of 2℃/min and a dwell time of 2 hours.

Characterization

Ceramic densities were determined by Archimedes' method using deionized water. Quasi-static compression tests were conducted on a servohydraulic load frame (Instron 8501) at a strain rate of 10^{-3}/s. For each ceramic, 10-15 cylindrical specimens [~11.0 mm (diameter) × 4.5 mm (height)] were tested.

6.1.2 Results and discussion

Powder characterization

Figure 6-1 shows XRD pattern of β-TCP precursor (apatitic tricalcium phosphate) as prepared at room temperature (Figure 6-1a) and β-TCP after calcination of the precursor at 800℃ for 3 hours (Figure 6-1b). Broad diffraction peaks in Figure 6-1a indicate β-TCP precursor has small crystallite size and poor crystallinity. The diffraction peaks are close to those of hydroxyapatite (HAP, JCPDF #9-0432) as marked in the pattern, indicating the precursor has similar structure as HAP. The precursor (apatitic tricalcium phosphate) is reported to have formula of $Ca_9(HPO_4)(PO_4)_5(OH)$ [79, 161].

After calcinations of the precursor at 800℃ for 3 hours, good crystalline β-TCP formed (Figure 6-1b). All peaks match with β-TCP (JCPDF #9-0169), with some Miller indices labeled in the pattern.

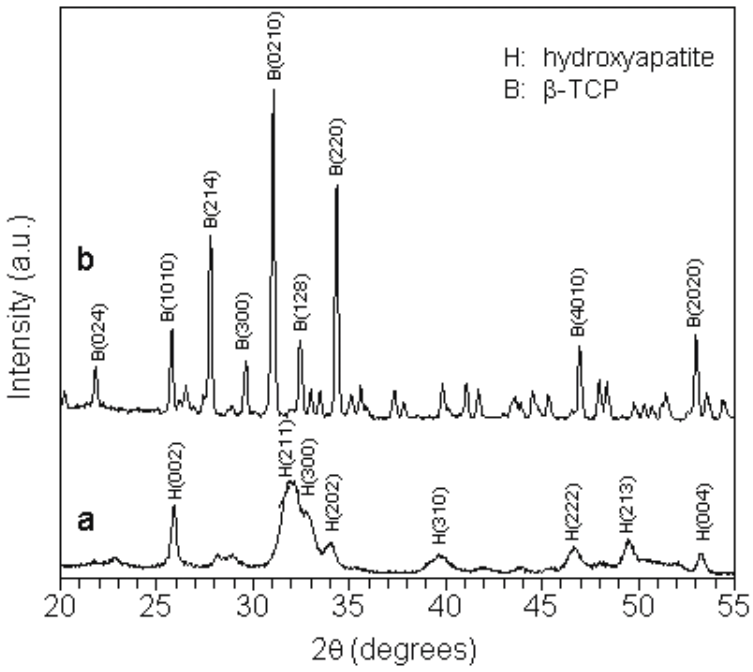

Figure 6-1. XRD pattern of (a) β-TCP precursor (apatitic tricalcium phosphate) and (b) β-TCP after calcination of the precursor at 800℃ for 3 hours.

The precipitation reaction and the calcination reaction to produce β-TCP are described as reactions (6) and (7) [78, 79] , respectively.

(6) $9Ca(NO_3)_2 + 6(NH_4)_2HPO_4 + 6NH_4OH \rightarrow Ca_9(HPO_4)(PO_4)_5(OH) + 5H_2O + 18NH_4NO_3$

(7) $Ca_9(HPO_4)(PO_4)_5(OH) \rightarrow 3Ca_3(PO_4)_2 + H_2O$

XRD pattern of β-TCMP-3 precursor as prepared (Figure 6-2a) and β-TCMP-3 produced at 800℃ (Figure 6-2b) are similar to the corresponding pattern in Fig. 1,

which indicates no new phase formed during the precipitation and calcination process with the presence of Mg^{2+}. The diffraction peaks in Figure 6-2b shift to large angles, compared to those of β-TCP in Figure 6-1b, indicating the substitution of Ca^{2+} by Mg^{2+} in β-TCP structure.

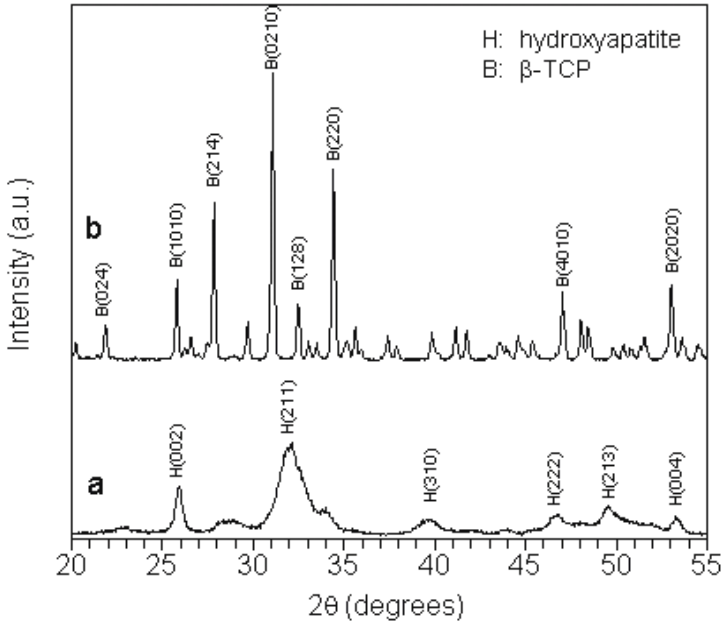

Figure 6-2. XRD pattern of β-TCMP-3 (3mol% Mg^{2+}) precursor (a) and β-TCMP-3 after calcination of precursor at 800℃ for 3 hours.

The precipitation of the β-TCMP precursor [$(Ca_{1-x}Mg_x)_9(HPO_4)(PO_4)_5(OH)$] and its decomposition to β-TCMP [$(Ca_{1-x}Mg_x)_3(PO_4)_2$] take place as Equations (8) and (9), respectively [162].

(8) $(9-9x)Ca(NO_3)_2+(9x)Mg(NO_3)_2+6(NH_4)_2HPO_4+6NH_4OH \rightarrow$

$$(Ca_{1-x}Mg_x)_9(HPO_4)(PO_4)_5(OH) +18NH_4NO_3+5H_2O$$

(9) $(Ca_{1-x}Mg_x)_9(HPO_4)(PO_4)_5(OH) \rightarrow 3(Ca_{1-x}Mg_x)_3(PO_4)_2+H_2O$

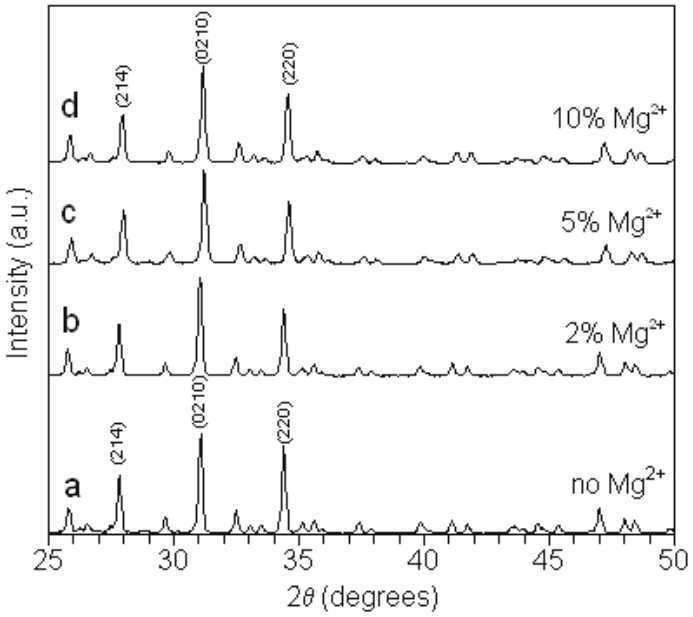

Figure 6-3. XRD pattern of (a) β-TCP, (b) β-TCMP-2, (c) β-TCMP-5 and (d) β-TCMP-10, produced at 800℃.

Figure 6-3 shows XRD pattern of β-TCMP samples with different Mg^{2+} content (up to 10 mol%) produced at 800℃. All peaks in the pattern match with β-TCP, indicating the incorporation of Mg^{2+} into the TCP structure. A maximum of 14.3 mol% Mg^{2+} can substitute Ca^{2+} in the β-TCP structure, without the formation of any new phase [28, 76]. With the increase of the content of Mg^{2+} (Figure 6-3a-d), diffraction peaks shift to large angles, indicating the contraction of the lattice constants. The refined lattice parameters (a and c) of β-TCP and β-TCMP were calculated from the diffraction patterns with MDI Jade 7 software, shown in Figure 6-4. Six peaks [Miller indices (3 0 0), (0 2 10), (1 2 8), (3 0 6), (1 1 12) and (2 0 0)] in each diffraction pattern were refined to calculate a and c values. The lattice parameters in Figure 6-4 are average values of lattice constants of at least 3 XRD patterns for each sample. For details of the refinement and calculation of lattice parameters from diffraction peaks, refer to Jade7 – XRD pattern

processing, identification & quantification, Materials Data, Inc. Both a and c values decreased with the increase of the content of Mg^{2+} (up to 10 mol%), due to the smaller ionic radius of Mg^{2+} (0.65 Å) compared to Ca^{2+} (0.99 Å).

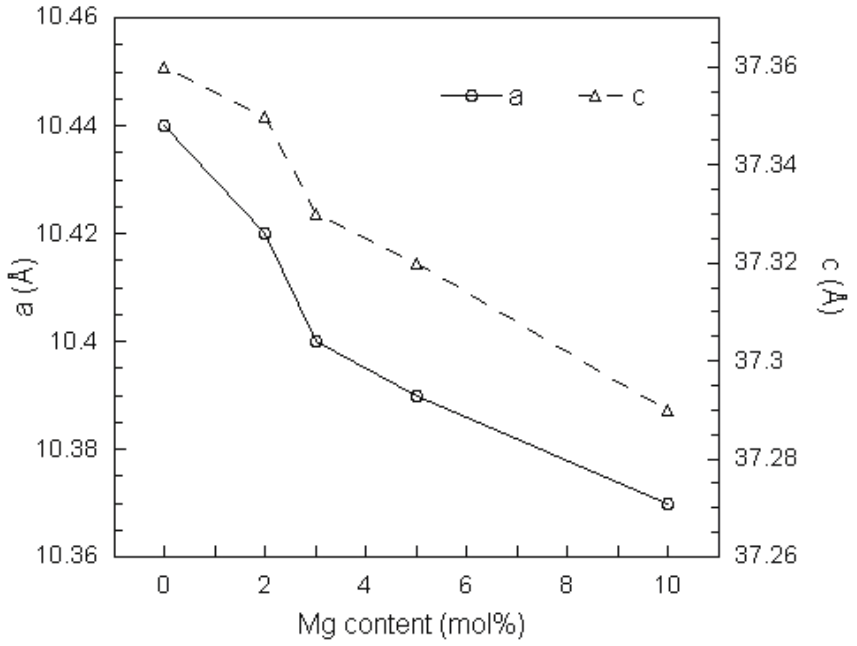

Figure 6-4. Influence of the incorporation of Mg^{2+} in β-TCP structure on the lattice parameters, a and c.

Figure 6-5a shows TG/DTA results of β-TCMP-3 precursor heated in air to 1300℃ with the heating rate of 5℃/min. The small endothermic peak around 725℃ in DTA curve indicates the decomposition of the precursor to form β-TCMP, Equation (4). The weight loss around the same temperature in the TG curve is the loss of water from the decomposition reaction. Figure 6-5b shows the DTA result of β-TCP powder heated in air with a heating rate of 5℃/min to 1000℃ and 2℃/min from 1000-1300℃. The exothermic peak around 1150℃ indicates the phase transformation from β- to α-TCP.

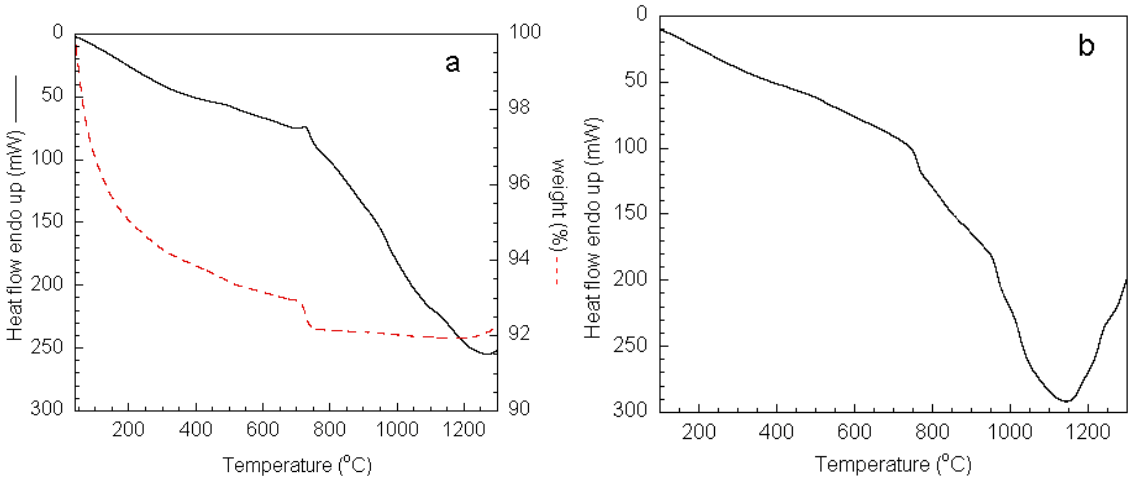

Figure 6-5. TG/DTA results of β-TCMP-3 precursor (a) and DTA curve of β-TCP powder (b) heated in air up to 1300℃.

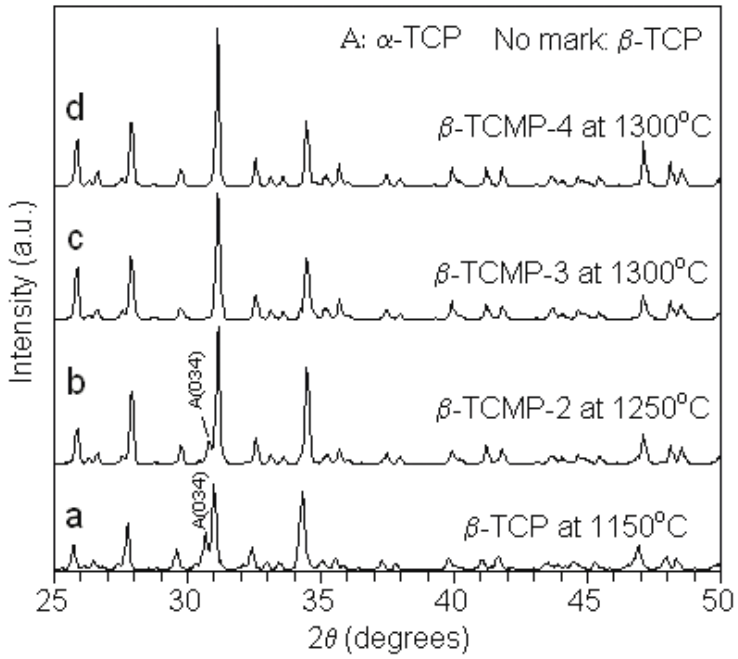

Figure 6-6. XRD pattern of β-TCP and β-TCMP samples after calcination at different temperatures for 2 hours: (a) pure β-TCP at 1150℃, (b) β-TCMP-2 at 1250℃, (c) β-TCMP-3 and (d) β-TCMP-4 at 1300℃.

Figure 6-6 shows XRD pattern of β-TCP and β-TCMP samples after calcination at different temperatures. Diffraction peak (034) from α-TCP (JCPDF #29-0359) was found in β-TCP sample after calcined at 1150℃ (Figure 6-6a), which is consistent with DTA result (Figure 6-5b). α-TCP was also found in β-TCMP-2 after calcined at 1250℃ (Figure 6-5b). No peak from α-TCP was found in β-TCMP-3 and β-TCMP-4 after calcination at 1300℃ for 2 hours, indicating that the phase transition temperature from β- to α-TCP in these samples exceeds 1300℃. These results demonstrate that the transition temperature from β- to α-TCP increases with the increase of Mg content in β-TCMP [76].

Ceramic density and microstructures

Figure 6-7 shows the measured density of β-TCP and β-TCMP-3 ceramics measured by Archimedes' method with deionized water. For each ceramic, 10-15 samples were used. For β-TCP ceramics, the average density of ceramics sintered at 1150℃ and 1250℃ are lower than that of ceramics sintered at 1100℃. This is caused by the formation of α-TCP in ceramics sintered at 1150℃ and 1250℃, which is indicated by the bulk XRD pattern (Figure 6-8b and Figure 6-8c) of the ceramics. β-TCP ($a = b = 10.44$ Å, $c = 37.38$ Å, $\alpha = \beta = 90^o$, $\gamma = 120^o$, cell volume = 3513 $Å^3$) to α-TCP ($a = 12.89$ Å, $b = 27.28$ Å, $c = 15.22$ Å, $\alpha = \gamma = 90^o$, $\beta = 126.2^o$, cell volume = 4318 $Å^3$) [28] transformation causes the expansion of TCP during the sintering process, which prevents TCP ceramics from further densification.

For β-TCMP-3 ceramics, only the β-TCP phase exists when sintered below 1300℃ (Figure 6-6c). The ceramic density increases with the increase of sintering temperature (Figure 6-7). The theoretical density of β-TCMP-3 is calculated to be 3.08 $g \cdot cm^{-3}$, based on the refined lattice constants (a = b = 10.40 Å, c = 37.33 Å, $\alpha = \beta = 90^{o}$, $\gamma = 120^{o}$) from XRD patterns. β-TCMP-3 ceramics sintered at 1150℃ and 1250℃, have average density of 2.98 $g \cdot cm^{-3}$ and 3.06 $g \cdot cm^{-3}$, with relative density of 96.8% and 99.4%, respectively. These results indicate that extremely dense β-TCMP ceramics can be prepared by sintering the ceramics above 1150℃ without the formation of α-TCP.

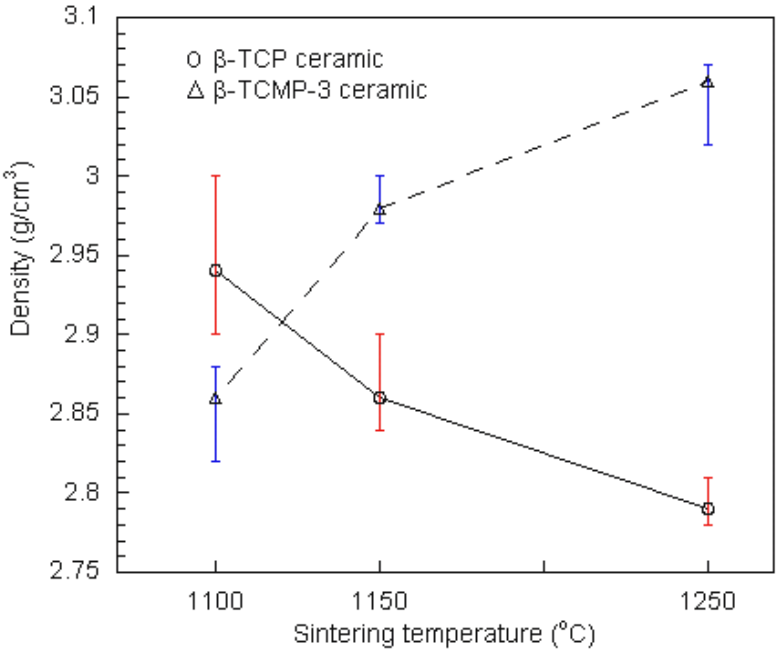

Figure 6-7. Average density of β-TCP and β-TCMP-3 ceramics sintered at different temperatures for 2 hours with error bars.

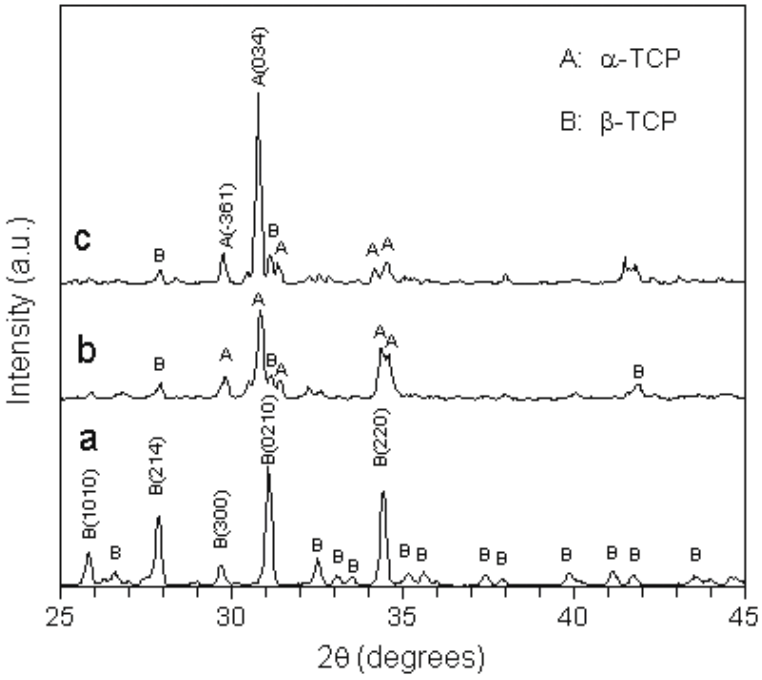

Figure 6-8. Bulk XRD pattern of β-TCP ceramics sintered at different temperatures: (a) 1100℃, (b) 1150℃ and (c) 1250℃.

SEM images of surfaces of β-TCP ceramics sintered at different temperatures are shown in Figure 6-9. β-TCP ceramics sintered at 1100℃ (Figure 6-9a) have grain size of several micrometers. A small amount of voids were found around grains, while micro-cracks were barely observed. After sintered at 1150℃ (Figure 6-9b), long cracks were observed in the ceramics. Some micro-cracks generated from the main cracks were also detected. The transformation from β-TCP to α-TCP can be observed by the formation of new continuous phase (α-TCP) around original β-TCP particles, which is consistent with XRD result (Figure 6-8b). The formation of α-TCP caused the expansion of ceramics, decreased the density (Figure 6-7) and created cracks.

After sintered at 1250℃, ceramics are mainly composed of α-TCP, which is indicated by the XRD result (Figure 6-8c). New grain boundaries of α-TCP can be observed, and the grain size is about several micrometers (Figure 6-9c and Figure 6-9d). More cracks were found in the ceramics (Figure 6-9c), compared to ceramics sintered at 1150℃. Micro-cracks (marked with arrows) were found even in dense portions of the sample (Figure 6-9d). Both intergranular and transgranular cracks are found in ceramics sintered at 1150℃ and 1250℃.

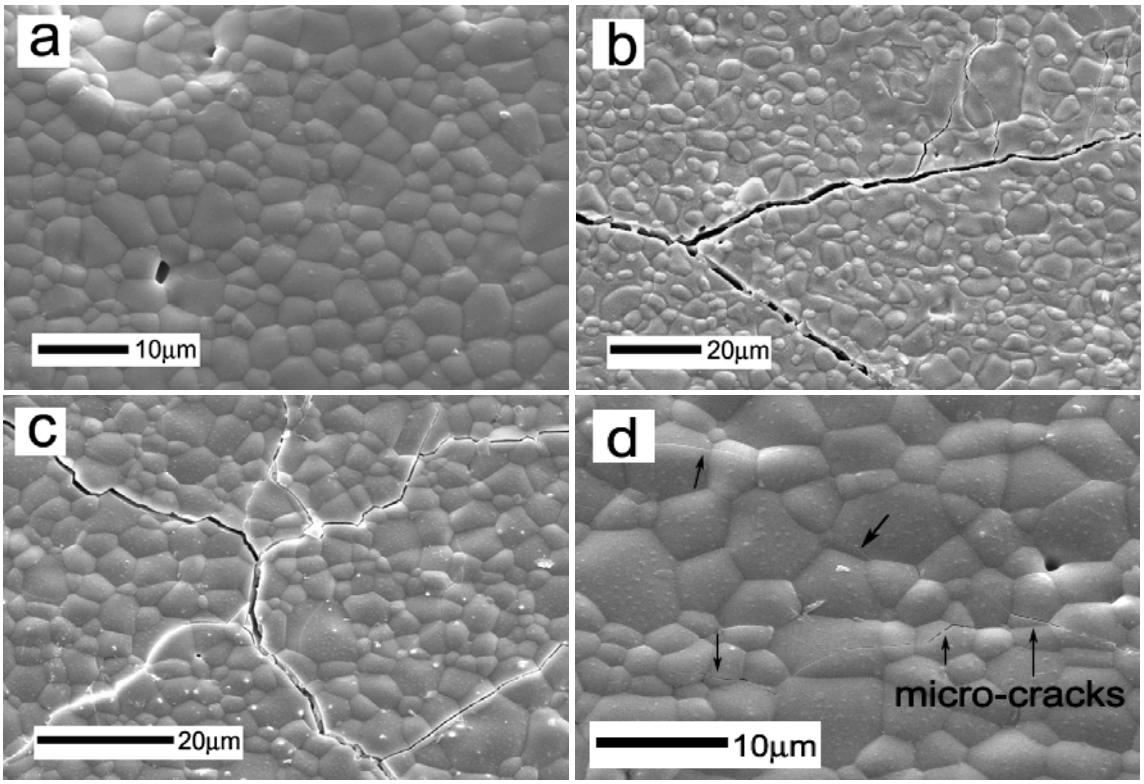

Figure 6-9. SEM images of surfaces of β-TCP ceramics sintered at different temperatures: (a) 1100℃, (b) 1150℃, (c) and (d) 1250℃.

Figure 6-10 shows SEM images of surfaces of β-TCMP-3 ceramics sintered at different temperatures. Voids around grains were found as the main defects in the ceramics sintered at 1100℃ (Figure 6-10a). Compared with β-TCP ceramics (Figure 6-9a), larger amount of voids were found in β-TCMP-3 samples. The grain size is about 1-4 micrometers (Figure 6-10a). Without phase transformation, β-TCMP grains grew up to several to ten micrometers when sintered at 1150℃ (Fig. 10b), and up to 20 micrometers at 1250℃ (Figure 6-10c). As a result of grain growth with the increase of sintering temperature, the density of β-TCMP-3 ceramics also increased, which is consistent with density measurement (Figure 6-7). Both intergranular and transgranular micro-cracks were found in β-TCMP-3 ceramics sintered above 1150℃ (Figure 6-10b and Figure 6-10c), which may be caused by severe contraction of the ceramics during the sintering process.

Mechanical strength of ceramics

Figure 6-11 shows typical stress-stain curves of β-TCP and β-TCMP-3 ceramics. The curves show a failure model of brittle materials. There are uncertainties in performing mechanical tests of ceramics in this investigation, due to the difference in specimen dimensions, existence of voids (Figure 6-9a and Figure 6-10a), macro-cracks (Figure 6-9b and Figure 6-9c) or micro-cracks (Figure 6-10b and Figure 6-10c).

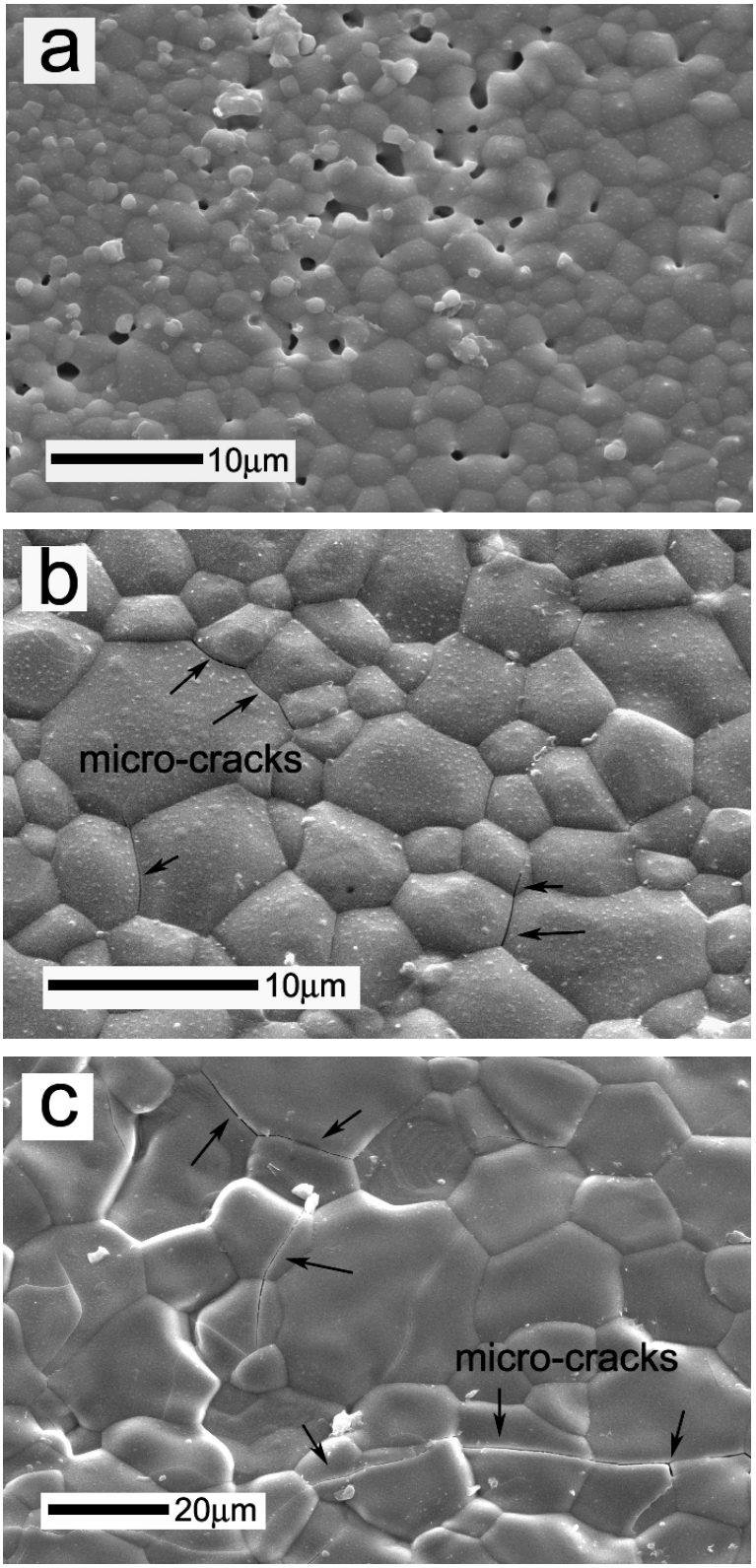

Figure 6-10. SEM images of surfaces of β-TCMP-3 ceramics sintered at different temperatures: (a) 1100℃, (b) 1150℃, and (c) 1250℃

The compressive strength of ceramics varies from specimen to specimen, which is indicated by Weibull distribution (Figure 6-12) of fracture stress of β-TCP and β-TCMP-3 ceramics sintered at 1100℃. Weibull analysis is applied by means of the following equation [163-165]:

$$P(V) = \exp\left[-\left(\frac{\sigma}{\sigma_0}\right)^m\right]$$

Where P(V) is the survival probability, σ_0 and m are Weibull parameters obtained experimentally, and σ is the compressive strength. The Weibull parameter 'm' for β-TCP and β-TCMP-3 ceramics are 5.92 and 4.22, respectively. The plots indicate that the 50% fracture probabilities (P(V) = 0.5) of β-TCP and β-TCMP-3 ceramics are ~540 MPa and 440 MPa, respectively, which are close to the average fracture strength of these two ceramics, 540 MPa and 430 MPa.

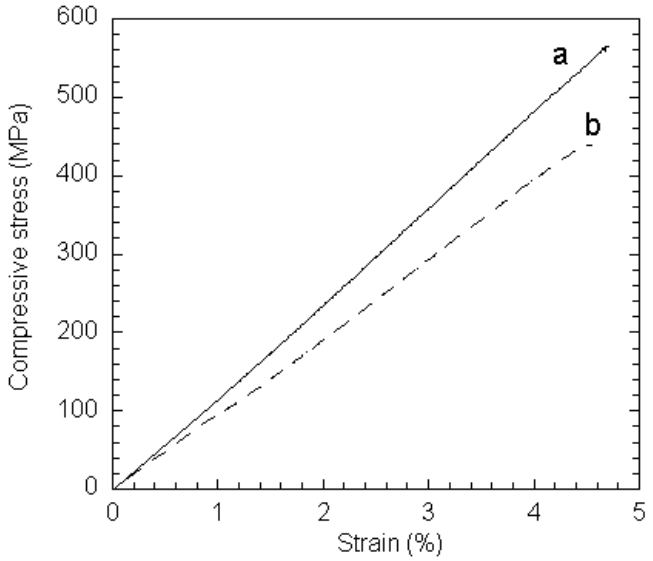

Figure 6-11. Quasi-static compressive stress-strain curves of (a) β-TCP and (b) β-TCMP-3 ceramics sintered at 1100℃ for 2 hours.

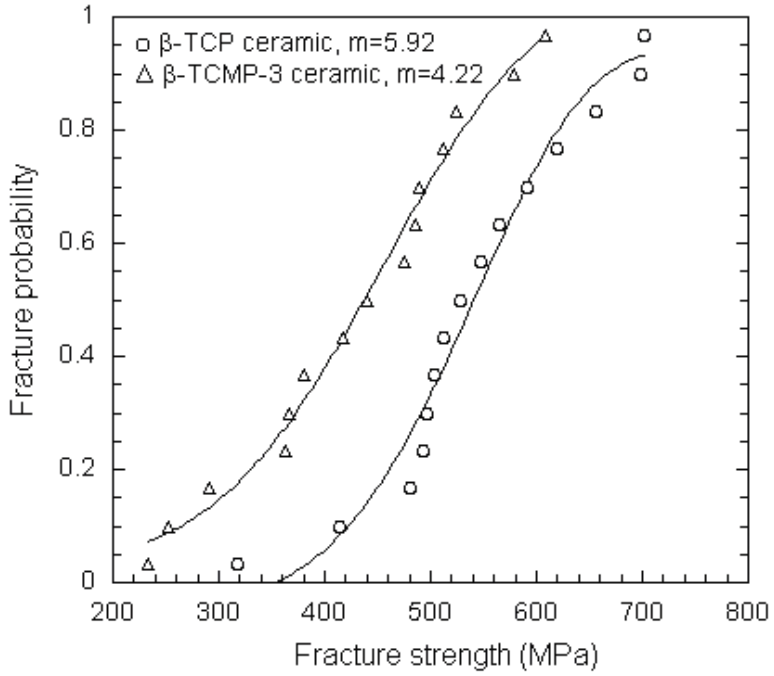

Figure 6-12. Weibull distribution of fracture stress of β-TCP and β-TCMP-3 ceramics sintered at 1100℃ for 2 hours.

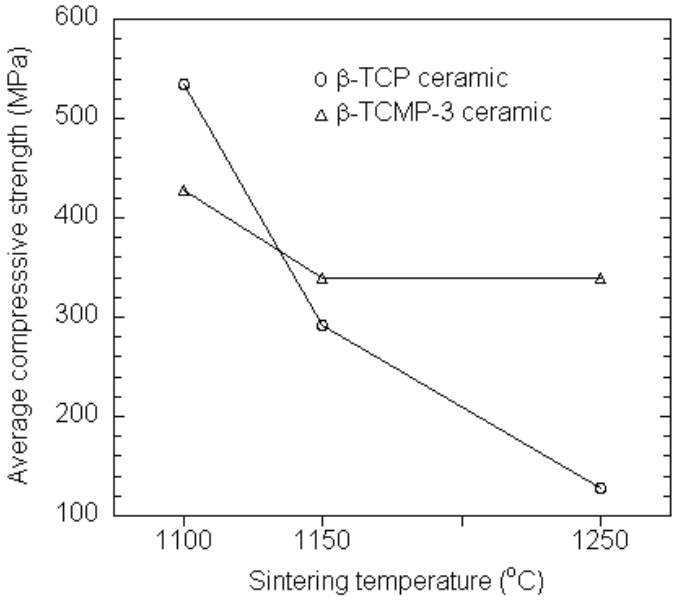

Figure 6-13. Average compressive strength of β-TCP and β-TCMP-3 ceramics sintered at different temperatures for 2 hours.

The average compressive strength of β-TCP and β-TCMP-3 ceramics are shown in Figure 6-13. The average strength of β-TCP ceramics sintered at 1100℃ is ~540 MPa. These ceramics have pure phase of β-TCP, indicating by the XRD result (Figure 6-8a), and micro-voids as the main defects (Figure 6-9a). Most samples sintered at 1100℃ fractured into small particles after failure in the compression tests. Ceramics sintered at 1150℃ and 1250℃ have average strength ~290 MPa and 130 MPa, respectively. These ceramics have α-TCP as the main phase (Figure 6-8b and Figure 6-8c) and macro- or micro-cracks as the main defects (Figure 6-9b-d). After failure in the compression tests, larger particles or pieces formed from these ceramics, which may be caused by fracture along the pre-existed cracks in the samples. The above results demonstrate that the formation of α-TCP at temperature above 1150℃, created cracks in the ceramics and decreased the mechanical strength.

The average compressive strength of β-TCMP-3 ceramics sintered at 1100℃ is ~430MPa, a little lower than that of β-TCP ceramics (540 MPa), due to larger amount of micro-voids in β-TCMP-3 ceramics (Figure 6-10a) compared with β-TCP ceramics (Fig. 9a). β-TCMP-3 ceramics sintered at 1150℃ and 1250℃ have the same average strength of ~340 MPa, which is lower than that of β-TCMP-3 ceramics sintered at 1100℃. Although the density of β-TCMP-3 ceramics increased with the increase of sintering temperature (Figure 6-7), the existence of micro-cracks and grain growth in the ceramics (Figure 6-10b and Figure 6-10c) sintered at temperatures above 1150℃ decreased the mechanical strength.

6.1.3 Conclusions

β-TCP or β-TCMP powders can be prepared by a two-step process: wet precipitation of apatitic tricalcium phosphate ('precursor') and calcination of the precursor at 800℃ for 3 hours. With the increase of Mg^{2+} content in the β-TCP structure, the transition temperature from β- to α-TCP increases. β-TCMP-3 (3mol% Mg^{2+}) has the transition temperature above 1300℃.

β-TCP ceramics prepared by pressing the green body at 100 MPa and sintering at 1100℃, have high average strength of ~540 MPa. β-TCP ceramics sintered above 1150℃ have α-TCP as the main phase, which caused the expansion of the samples, decreased the ceramic density, and created cracks in the samples. These pre-existed cracks in the ceramics caused fracture along cracks and decreased the compressive strength of the ceramics.

Dense β-TCMP-3 ceramics were prepared by sintering at temperature above 1150℃. Average relative density of β-TCMP-3 ceramics sintered at 1150℃ and 1250℃ are 96.8% and 99.4%, respectively. However, the formation of micro-cracks and grain growth in dense β-TCMP-3 ceramics sintered above 1150℃ decreased the compressive strength of the ceramics.

6.2 Porous β-TCP or β-TCMP ceramics

The important role of the morphology of ceramic implants has been considered since the use of porous material was first described in 1963 [166]. Many papers in the literature demonstrated a greater degree and faster rate of bone ingrowth or apposition with porous implants. The rate and quality of bone integration to the porous implants are believed to be dependent on pore size, porosity volume fraction, interconnection size, and interconnection density, both as a function of structural permeability and mechanics.

Scaffold permeability

Scaffolds should posses open pores, fully interconnected geometry in a highly porous structure with large surface to area volume ratios that will allow cell in-growth and an accurate cell distribution through the porous structure, and will facilitate the vascularization.

A pore size of 100 μm is generally considered as a minimum requirement for new bone ingrowth [128]. Earlier work [129] had previously shown that interconnection sizes were critical in determining the quality of tissue ingrowth within porous calcium aluminate ceramics. Interconnection sizes of >100, >40, and >5 μm were required for ingrowth of mineralized tissue, osteoid, and fibrous tissue, respectively. More recently, Lu *et al.* [167] demonstrated that when using either HAP or b-TCP, the critical pore interconnection size for bone ingrowth was only 50 μm. Any new bone formation or repair must always be preceded by the formation of a vascular network, the rapidity and

extent of which is strongly influenced by the degree of structural interconnectivity between pores [168].

These results would suggest that both pore size and pore interconnection size, which is often related to both pore size and the extent of porosity [169, 170], are likely to be responsible for the structural permeability of bone substitutes.

Scaffold mechanics

The mechanical behavior of various bone grafts vary widely [157, 171, 172] in different applications. However, any bone substitute must permit even load distribution and should not be overly stiff, so as not to produce load concentrations or stress shielding [173]. Thus, appropriate modification of the macrostructure to distribute loads and match the intended host tissue will improve the biocompatibility, such as has been demonstrated with the use of hydrothermally converted corals with highly porous structures similar to anisotropic cancellous bone in the filling of cancellous bone defects [171].

Additionally, it has been demonstrated that in the longer term, both micro- and macroporosity influence bone adaptation [174-176], where it was proposed that a reduction in strut modulus associated with increasing microporosity levels was sufficient to shift the strut modulus below a threshold value resulting in a swing in the equilibrium local bone cell activity toward a greater degree of stable bone apposition.

In this section, interconnected macroporous β-TCP or β-TCMP ceramics with micropores in the struts are prepared either by a two-step pressing method with sucrose as porogen or replication of polyurethane foam.

6.2.1 β-TCP or β-TCMP powders from solid-state reactions

Solid-state reactions were used to prepare β-TCP and β-TCMP in this section. For β-TCP, DCPA and $CaCO_3$ powders were weighted with the proper ratio and ground in a mortar to create a homogeneous mixture. The mixture was then heated in the muffle furnace at 1000℃ for 6 hours to complete the reaction (Figure 6-14a). The formation of α-TCP by heating β-TCP at 1150℃ for 4 hours was conformed by XRD result (Figure 6-14b).

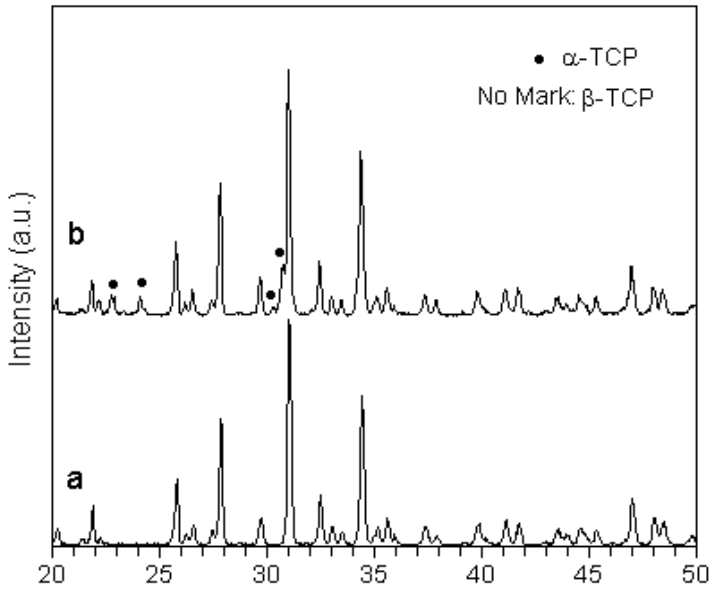

Figure 6-14. XRD of (a) β-TCP prepared from solid-state reaction of DCPA and $CaCO_3$ powder at 1000℃ for 6 hours and (b) the products after heating β-TCP at 1150℃ for 4 hours.

β-TCMP was prepared by adding certain amount of MgO to the mixture of DCPA and $CaCO_3$ with (Ca+Mg)/P molar ratio of 1.5. Hereafter, β-TCMP samples with 1

mol%, 3 mol%, 5 mol%, 10 mol% Mg^{2+} prepared by the solid-state reactions in this investigation are designated as β-TCMP1, β-TCMP3, β-TCMP5 and β-TCMP10, respectively.

To study reaction mechanisms, thermal analysis (TG/DTA) of mixtures of DCPA and $CaCO_3$ with/without MgO (Figure 6-15b and Figure 6-15a), and DCPA (Figure 6-15c) or $CaCO_3$ (Figure 6-15d) alone, were performed at a heating rate of 10℃/min in air. Peaks around 450℃ in Figure 6-15a-c indicate the pyrophosphate of DCPA shown as Equation (12). Around 750℃, $CaCO_3$ decomposed to CaO as Equation (13) (Figure 6-15a, b and d). Meanwhile, $Ca_2P_2O_7$ started to react with CaO to form β-TCP at the same temperature indicated by Equation (14). The whole reaction [Equation (10)] to produce β-TCP is a summation of Equations (12)-(14). For β-TCMP, the whole reaction took place as Equation (11).

(12) $2CaHPO_4 \rightarrow Ca_2P_2O_7 + H_2O$

(13) $CaCO_3 \rightarrow CaO + CO_2$

(14) $Ca_2P_2O_7 + CaO \rightarrow Ca_3(PO_4)_2$

(10) $2CaHPO_4 + CaCO_3 \rightarrow \beta\text{-}Ca_3(PO_4)_2 + H_2O + CO_2$

(11) $(1-x)\,CaCO_3 + xMgO + 2CaHPO_4 \rightarrow (Ca_{3-x}Mg_x)(PO_4)_2 + H_2O + (1-x)CO_2$

Figure 6-16 shows XRD patterns of β-TCP, β-TCMP5 and β-TCMP10 produced at 1000℃. All peaks in the pattern match with β-TCP, demonstrating the incorporation of Mg^{2+} into β-TCP structure. With the increase of the content of Mg^{2+} (Figure 6-16a-c), diffraction peaks shift to large angles, indicating the contraction of lattice constants.

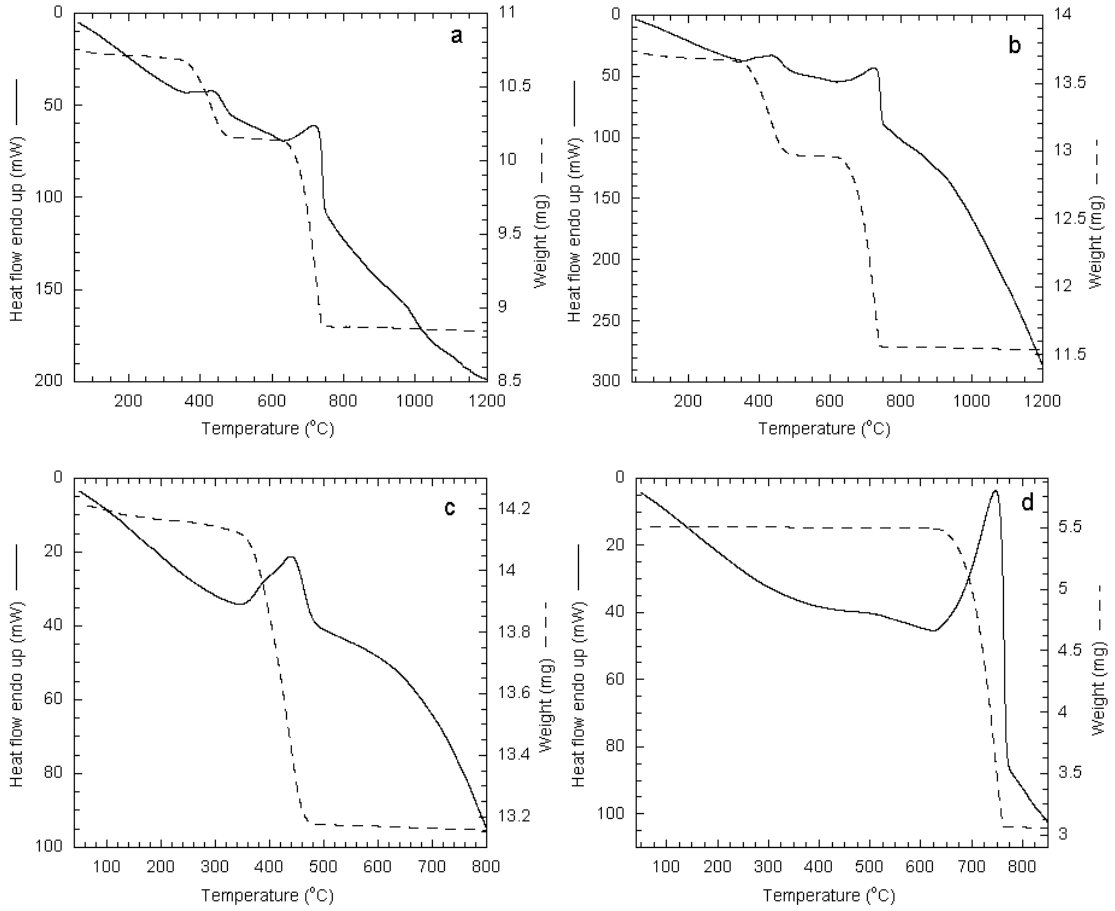

Figure 6-15. Thermal analysis data at a heating rate of 10℃/min for: (a) the mixture of DCPA and $CaCO_3$ with Ca/P molar ratio of 1.5; (b) the mixture of DCPA and (95%CaCO3+5%MgO); (c) DCPA and (d) $CaCO_3$.

No phase transformation from β- to α-TCP was found after heat treatment of β-TCMP1 at 1200℃ for 2 hours in air (Figure 6-17a). However, after being heated at 1250℃ for 2 hours, a small amount of α-TCP was detected (Figure 6-17b). For β-TCMP3, no phase transformation was found after heat treatment at 1300℃ for 2 hours (Figure 6-17c). These results indicate that β- to α-TCP transition temperature increases with the increase of Mg mol% in β-TCMP.

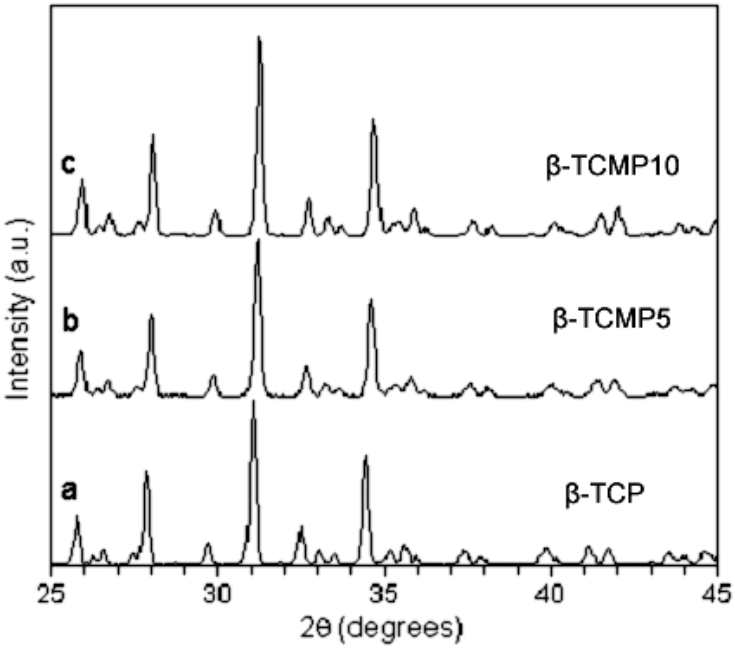

Figure 6-16. XRD pattern of β-TCP and β-TCMP samples.

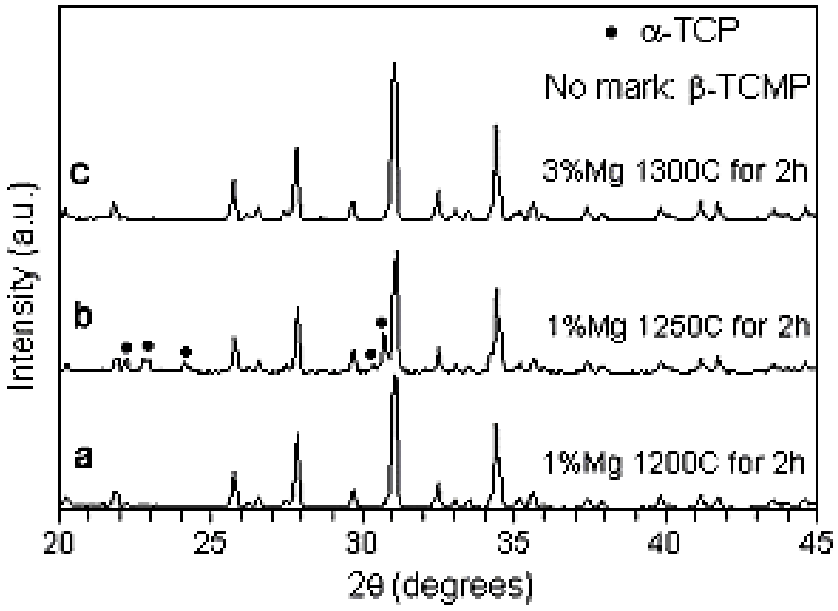

Figure 6-17. XRD pattern of β-TCMP samples after heat treatment at different temperatures for 2 hours: (a) β-TCMP1 at 1200℃; (b) β-TCMP1 at 1250℃; (c) β-TCMP3 at 1300℃.

To create macroporous ceramics, two methods were used: extrusion with sucrose as porogen and replication of polymeric foam, which are described in details in Sections 6.2.2 and 6.2.3, respectively.

6.2.2 Porous ceramics by the extrusion with a prorogen

Porous β-TCMP ceramics were produced by the extrusion method, with sucrose used as the porogen in this method. Sucrose particles in the range of 250-500 μm were collected by sieving, and mixed with β-TCMP3 powder in a mortar with several drops of water. The volume ratio of β-TCMP3/sucrose was ~1.0. The mixture was first uniaxially pressed in the die at 20MPa to form an initial compact at room temperature. This compact was heated at 170℃ for 30 minutes to partially melt the sucrose, and then hot pressed at the same temperature to 60 MPa. The green body was then heated to 600℃ in a muffle furnace with a heating rate of 4 ℃/min to burn off the sucrose, and further sintered at 1250℃ with a heating rate of 2 ℃/min and dwell time of 2 hours to create macroporous ceramic.

SEM images of the porous β-TCMP3 ceramics are shown in Figure 6-18. The pore size is in the range of 100-300 μm. Most pores in the ceramic are open and interconnected. This may be linked to good connection of the partially melted sucrose in the second-step pressing at 170℃, which then forms well-interconnected pores in the extrusion.

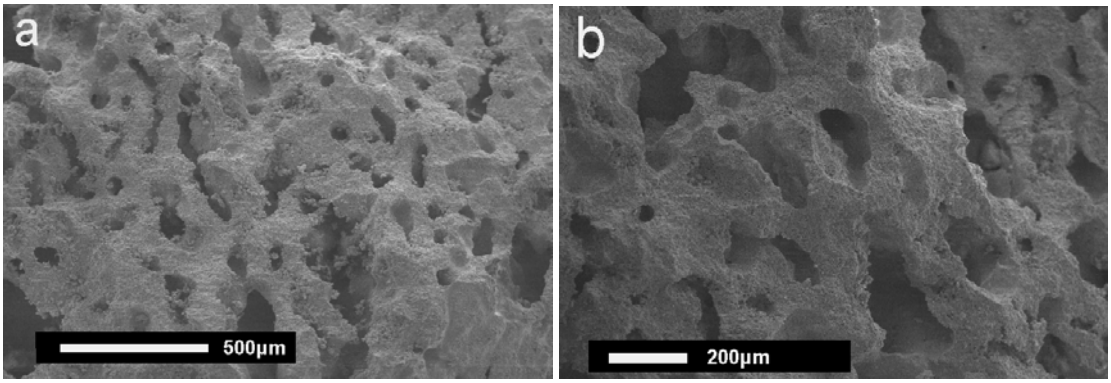

Figure 6-18. SEM images of macoporous β-TCMP3 ceramics prepared from extrusion method with sucrose as a porogen.

6.2.3 Porous ceramics by the replication using polyurethane foams

For the replication of polyurethane sponge method, ceramic slurry was prepared by mixing β-TCMP3 powder with 5 wt.% polyvinyl alcohol (PVA) in different ratios. The slurry was infiltrated into macroporous polyurethane (PU) pieces (1cm×1cm×1cm), which was then heated to 600℃ with a heating rate of 4 ℃/min for pyrolysis of the PU foam, and further sintered at 1250℃ with a heating rate of 2℃/min and dwell time of 2 hours to create the macroporous ceramic.

Figure 6-19a shows the original PU foam piece (1cm×1cm×1cm), which has three-dimensional interconnected porous structure. Figure 6-19b-d show the porous β-TCMP3 ceramics created by the replication method. The slurry used for Figure 6-19b-d are different combinations of β-TCMP3(g) and PVA(mL): b. 2g+1.5mL, c. 2g+2mL, d. 1.5g+1mL and e. 1.5g+1.5mL. The ceramic replications maintain the three-dimensional interconnected structures of the original PU foam. Higher porosity were observed in samples of Figure 6-19d and Figure 6-19e, than that in the samples of Figure 6-19b and Figure 6-19c. This indicates that ceramic porosity increases with the decrease of the

amount of ceramic powder in the slurry. However, a small amount of ceramic powder (<1g) was not enough to form intact porous scaffold from 1cm^3 PU foam.

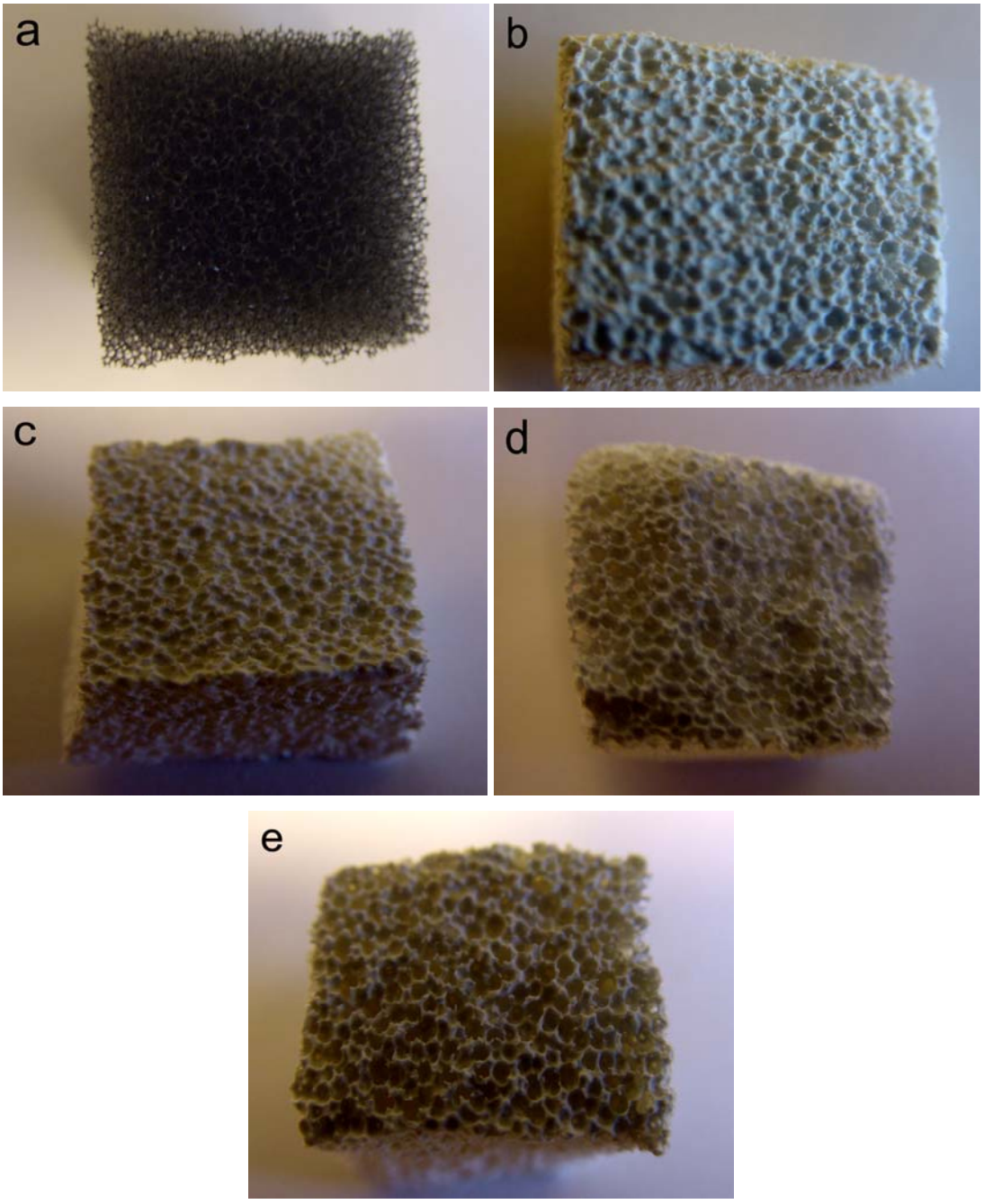

Figure 6-19. Photos of original PU foam (a) and porous β-TCMP3 ceramics created by the replication method (b, c, d and e).

Figure 6-20 shows SEM images of PU foam and porous β-TCMP3 ceramics. The original PU foam has an interconnected porous structure (Figure 6-20a). The pore size is in the range of 100-500 μm, and the connected strut size is ~100 μm. A few open pores were found in β-TCMP3 ceramic created with the slurry of 2g powder and 1.5mL PVA (Figure 6-20b and Figure 6-20c), which are ~200-400 μm. For β-TCMP3 ceramic produced with the slurry of 1.5 g powder and 1.5 mL PVA, there is a relatively large amount of open pores (Figure 6-20d and Figure 6-20e), which are interconnected and in the size range of 100-500 μm. Micropores were also found on the struts of these ceramics (Figure 6-20f).

Conclusions

β-TCMP and β-TCP were prepared by solid-state reactions of DCPA and $CaCO_3$ with/without MgO. The process followed multiple-step reactions with the increase of heating temperature. DCPA first pyrolyzed into $Ca_2P_2O_7$ around 450℃. Around 750℃, $CaCO_3$ decomposed to CaO, and $Ca_2P_2O_7$ started to react with CaO to produce β-TCP at the same temperature.

With the increase of Mg^{2+} content in β-TCP structure, the transition temperature from β- to α-TCP increases. β-TCMP3 (3 mol% Mg^{2+}) has the transition temperature above 1300℃. These results are consistent with those from Section 6.2.

Macroporous β-TCMP ceramics were prepared by both the extrusion method with sucrose as a porogen, and the replication method using polyurethane foams.

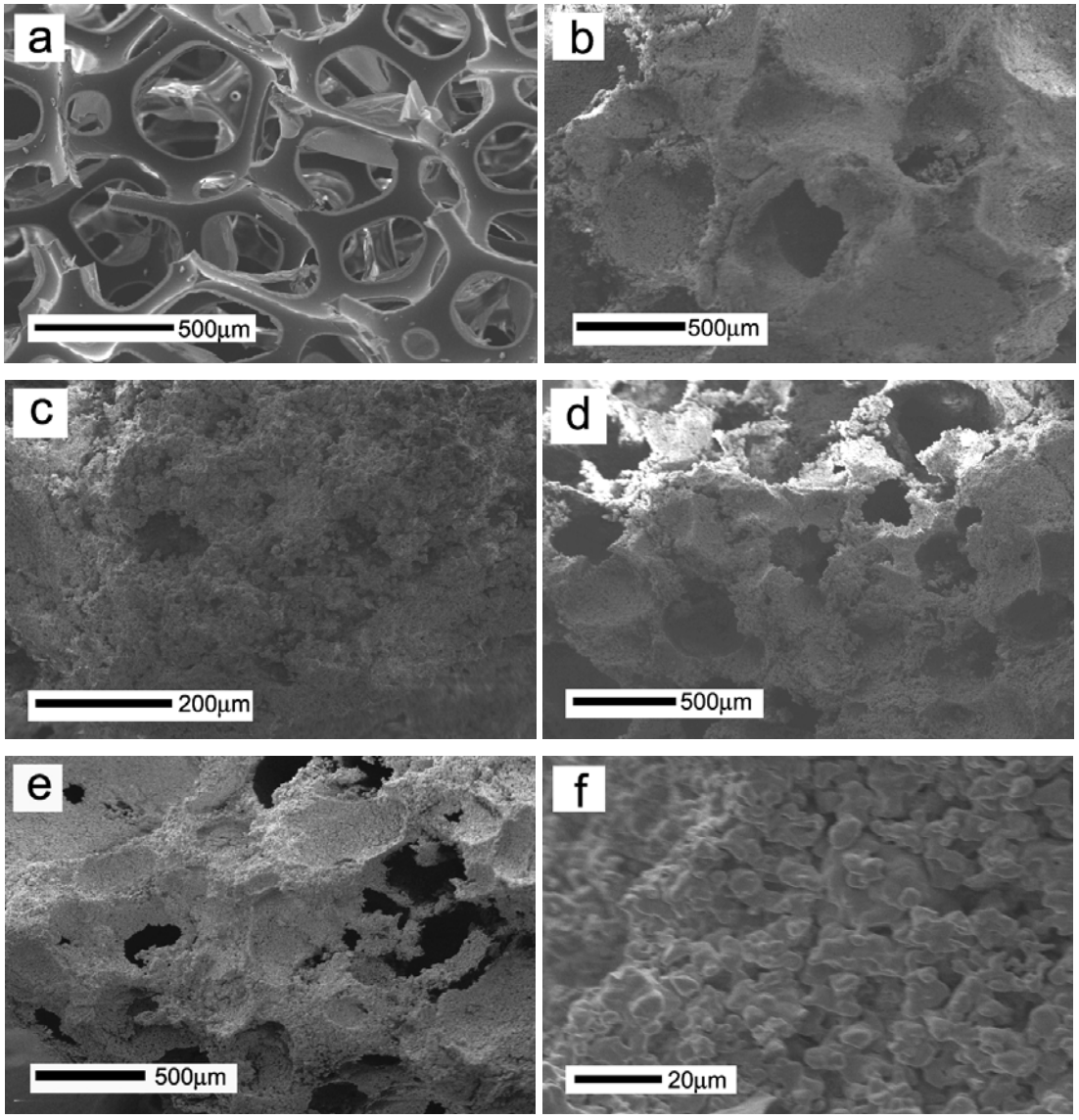

Figure 6-20. SEM images of PU foam (a), β-TCMP3 ceramics produced with the slurry of 2g powder and 1.5mL PVA (b and c), and with the slurry of 1.5g powder and 1.5mL PVA (d, e and f).

6.3 Bone-mimicking β-TCMP ceramics

Interconnected macroporous β-TCP ceramics are preferred to be used as bone defect filler, considering the ability for infiltration of bone cells and vessels into the scaffold. However, most macroporous β-TCP ceramics are too brittle to work as temporary

scaffolds in implant surgery. Dense β-TCMP ceramics have the strength, which meet the mechanical requirement, but their dense structures don't facilitate new bone ingrowth. Therefore, the combination of dense and porous structure, mimicking human bone, is necessary to meet both permeability and mechanical requirements.

In this section, resorbable β-TCMP ceramics with porous structures in the center surrounded by dense shell-like structures were created. The outside dense structures give the strength to scaffold, which can then be used in load-bearing cases. The central porous structures enable infiltration of bone cells and vessels, and finally ingrowth of new bone.

PU foams were cut into cylindrical pieces, 10mm (diameter) × 10mm (height). β-TCMP3 slurry was infiltrated into these cylindrical pieces, as described in Section 6.2. A piece of foam was then centered in a paper cylinder mold, 18mm (diameter) × 20mm (height).

β-TCMP-3 powder (as prepared in Section 6.1) was ground, and mixed with 5 wt.% PVA to make a viscous slurry, which was filled into the gap between the foam and the mold. The green body with the mold (Figure 6-21a) was then heated to 600℃ at a heating rate of 4℃/min to burn off the PU foam and paper cylinder, and further heated from 600℃ to 1250℃ at a rate of 2℃/min, and sintering at 1250℃ for a dwell time of 2 hours.

Figure 6-21b shows the ceramic piece after sintering the green body at 1250℃. The porous structure in the center surrounded by a dense shell structure can be seen in the image. There is a significant shrinkage of the green body (~18mm in diameter) to the

ceramic piece (~12mm in diameter), which is mainly cansed by densification of the outside dense portion.

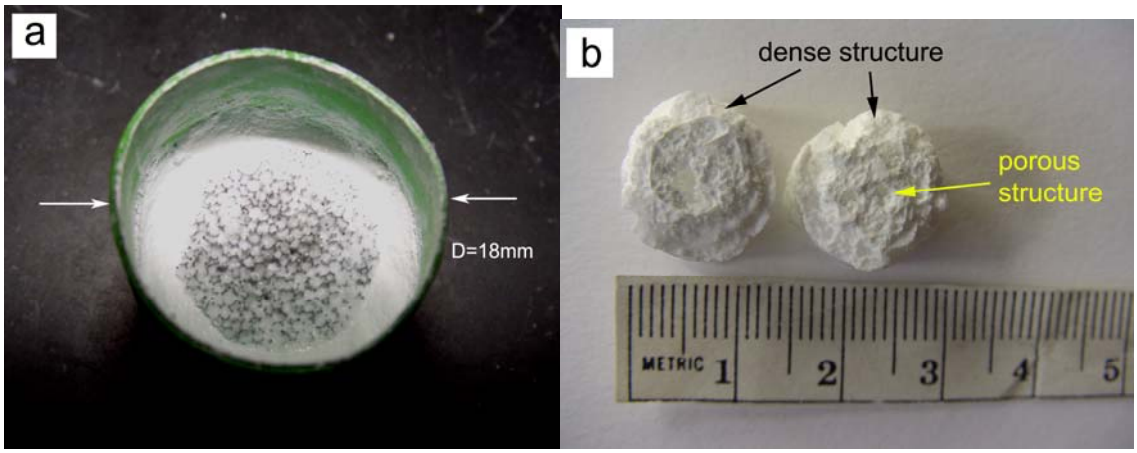

Figure 6-21. Photos of (a) paper cylinder mold used to create green body from β-TCMP slurry and PU foam, and (b) ceramic piece after sintering the green body at 1250℃ for 2 hours.

Figure 6-22 shows SEM images of the ceramic piece section. Figure 6-22a shows the central porous portion is well bonded to the outside dense structure in the ceramic. Figure 6-22b and Figure 6-22c are images of the outer dense structure, which is composed of densified micro-size grains, with a small amount of micropores. Figure 6-22d and Figure 6-22e show the macroporous structure created from the PU foam. The pores are in the range of 100-500μm, and most pores are interconnected. The strut in the porous portion (Figure 6-22f) is formed by necking micro-size particles; a large amount of micropores were found in the strut.

This particular designed β-TCMP ceramic can meet both mechanical and permibility requirements to work as a scaffold in minor-load bearing cases, and potentially load-bearing cases.

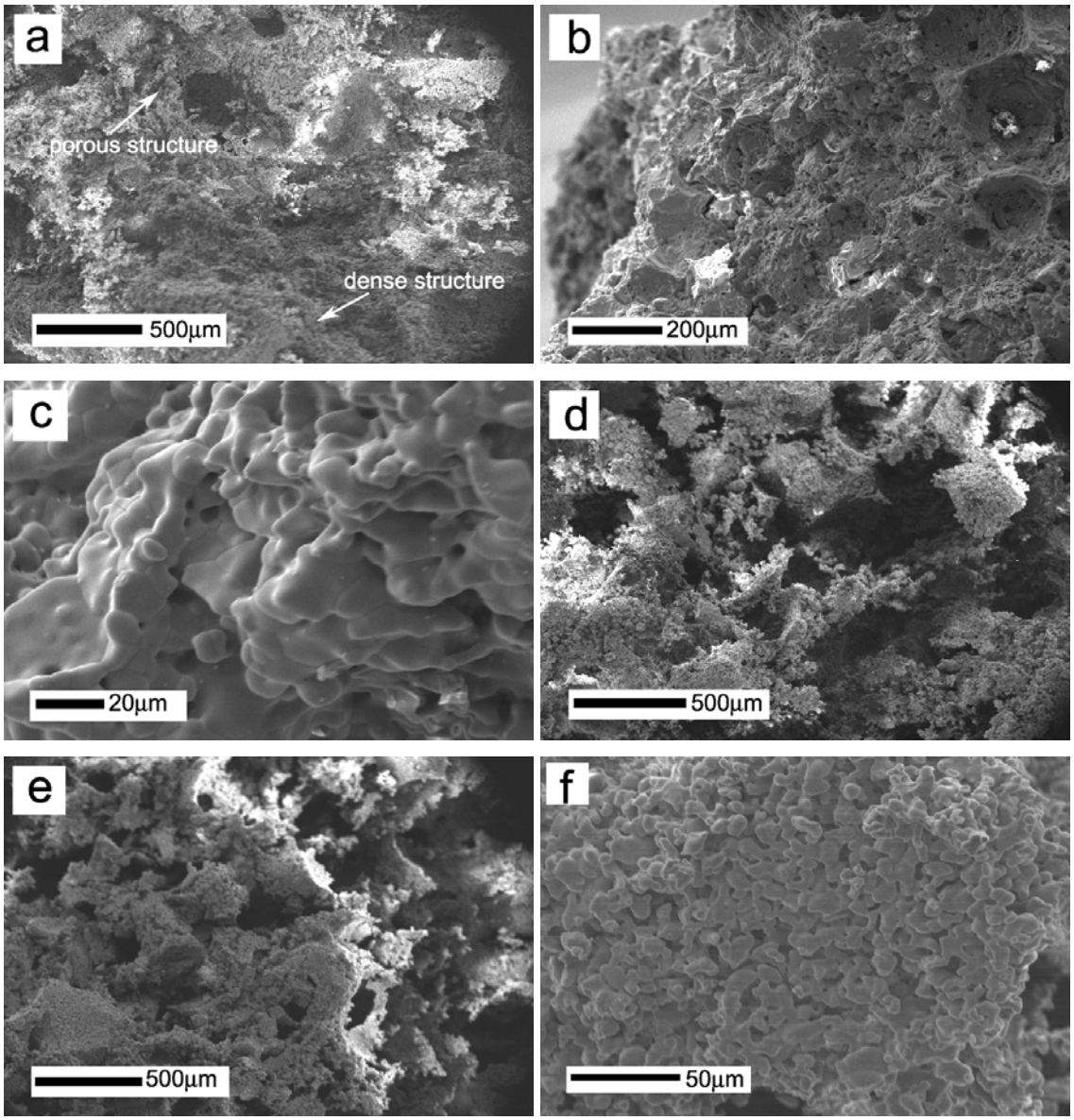

Figure 6-22. SEM images of the ceramic section with porous structure in the center and dense structure outside: (a) porous structure welded by the dense structure; (b) and (c) from dense portion; (d)-(f) from porous portion.

Acknowledgements

Chapter 6, in part, was a reprint of the materials in the manuscript: X. Zhang, F. Jiang, T. Groth and K.S. Vecchio. Preparation, Characterization and Mechanical

performance of β-TCP Ceramics with/without Magnesium Substitution. Submitted to Journal of Materials Science: Materials in Medicine.

7 SUMMARY AND FUTURE WORK

1. In Section 4.1, dense structures of HAP were created by hydrothermal conversion of conch and clamshells at relative low temperature (~200ºC). The average partially converted conch or clamshell samples have mechanical strength close to that of compact human bone, which indicates that the converted shell samples can be used as implants in load-bearing applications. After implantation in rat femoral defects for 6 weeks, newly formed bone was found to grow up to and around the converted shell samples. The tightly joined interface between the implant and bone indicates the good biocompatibility of these converted shell samples. Comparing to the traditional sintering methods, the hydrothermal method to create dense HAP from seashells with high mechanical strength is valuale in the perspective of cost and effectiveness.
2. Sea urchin spines were converted to resorbable Mg-substituted tricalcium phosphate (β-TCMP) instead of non-resorbable HAP by the hydrothermal reaction at relative low temperature ~180ºC, while maintaining the three-dimensional interconnected porous structure (Section 4.2). In-vivo tests, in rat femoral defects for 6 weeks, show good bioactivity and osteoconductivity of these porous β-TCMP implants. New bone was found to grow up to and around the implants. Some new bone was found to migrate through the pores, starting from the outside of the implant through the pores at the edge of the implants. Growth of new bone into the center of the

3. porous structure and the eventual resorption of β-TCMP sample may be expected in longer duration in-vivo experiments.
4. White coral (porosity ~40%) pieces were converted into HAP at 250ºC for 2 days, while maintaining original macroporous structures (Section 4.3.1). Some HAP and β-TCP particles were found on the surfaces of the stems, which are believed to form through the dissolution-reprecipitation process, although the main conversion is ion-exchange process. In Section 4.3.2, cuttlebone samples (porosity ~93%) were also hydrothermal converted into HAP at 160ºC for 8 hours, while maintaining the three-dimensional interconnected macroporous structures. This hydrothermal conversion method is effective to produce macroporous HAP in contrast to ceramic sintering with porogens.
5. HAP rods, with a small amount of β-TCP as a byproduct, were synthesized by the hydrothermal reaction of dicalcium phosphate anhydrous (DCPA) and cuttlebone powder (aragonite polymorph of $CaCO_3$) or $CaCO_3$ chemical (calcite polymorph of $CaCO_3$) from 120ºC to 180ºC for different durations (Section 5.1). The synthesis is observed to be a nucleation-growth process. Both DCPA and calcium carbonate provide ion sources to the solution for the nucleation and growth of HAP. HAP rods synthesized would have potential application as reinforcement of HAP ceramics.
6. In Section 5.2, good crystalline HAP particles were prepared through a two-step process. HAP was first precipitated from $(NH_4)_2HPO_4$ and $Ca(NO_3)_2$ solution at 80℃, which was then hydrothermal treated at 140℃ for 24 hours to improve the product crystallinity. This HAP product can be used to produce HAP or biphasic calcium phosphate ceramics in future.

7. In Section 6.1, β-TCP or β-TCMP powders can be prepared by a two-step process: wet precipitation of apatitic tricalcium phosphate ('precursor') and calcination of the precursor at 800℃ for 3 hours. With the increase of Mg^{2+} content in β-TCP structure, the transition temperature from β- to α-TCP increases. β-TCMP-3 (3 mol% Mg^{2+}) has its transition temperature above 1300℃.

   Dense β-TCP ceramics prepared by pressing the green body at 100 MPa and sintering at 1100℃, have the average strength of 540 MPa. However, above 1150℃, α-TCP was found in the ceramics, and both the density and strength of ceramics decreased. Highly dense β-TCMP-3 ceramics can be prepared by sintering at temperatures above 1150℃ without the transformation from β- to α-TCP. The average relative density of β-TCMP-3 ceramics sintered at 1150℃ and 1250℃ are 96.8% and 99.4%, respectively. Therefore, Mg-substitution is an effective method to prevent phase transformation during the sintering of β-TCP ceramics.

8. Solid-state reactions from DCPA and $CaCO_3$ powders were used to prepare β-TCP (Section 6.2.1). β-TCMP was produced with the addition of MgO to the mixture. The reaction was completed at 1000℃ for 6 hours. Interconnected macroporous β-TCMP ceramics were either created by the extrusion method with sucrose as the porogen (Section 6.2.2) or by the replication method using polyurethane foams (Section 6.2.3). β-TCMP ceramics can be sintered at high temperature to create the macroporous structures without the formation of α-TCP.

9. Resorbable β-TCMP ceramics with porous structure in the center surrounded by dense structure were created. This particular designed β-TCMP ceramic can meet

both mechanical and permeability requirements, when used as a scaffold in minor-load bearing cases.

10. For future work, coating of biodegradable polymers onto the converted coral and cuttlebone samples will be considered to improve the mechanical strength of these products. By mixing HAP and β-TCP prepared in our experiments, biphasic calcium phosphate (BCP) powders can be produced. BCP ceramics in dense/porous forms can be created.

REFERENCES

1 Laurencin CT, Attawia M, and Borden MD, Current Opnion in Orthopedics 1999; 10: 445-451.

2 Enneking W, J.Am.Coll.Sur. 2005; 201: 5-6.

3 LeGeros RZ, Clinical Materials 1993; 14: 65-88.

4 Karageorgiou V and Kaplan D, Biomaterials 2005; 26: 5474-5491.

5 Hing KA, Int. J. Appl. Ceram. Technol. 2005; 2: 184-199.

6 LeGeros RZ, Clinical Orthopaedics and Related Research 2002; 395: 81-98.

7 Vallet-Regí M, González-Calbet JM, Progress in Solid State Chemistry 2004; 32: 1-31.

8 Aoki H, Kato K, Ogiso M, and T. T, J. Dent. Eng. 1977; 18: 86-89.

9 Baron VC, Levin MP, and Adams DF, J. Periodontal. 1986; 57: 764-770.

10 Cranin AN, Tobin GP, and Gelbman J, Compend. Contin. Educ. Dent. 1987; 8: 334-345.

11 Denissen HW and De Groot K, J. Prosthet. Dent. 1979; 42: 551-556.

12 Elliger RF, Nery EB, and Lynch KL, Int. J. Perio. Restor. Dent. 1986; 3: 223-233.

13 Albee FH, Ann. Surg. 1920; 71: 32-36.

14 Dalculsi G, Passuti N, Martin S, Deudon C, LeGeros RZ, and Raher S, J. Biomed. Mater. Res. 1990; 24: 379-396.

15 Sun L, Berndt CC, Gross KA, and Kucuk A, Journal of Biomedical Materials Research 2001; 58: 570-592.

16 Walter PV, J. Chir. und Augen-Heilkunde 1821; 2: 571.

17 Ollier L, Victor Masson. 1867, Paris.

18 Senn N, Amer. J. Med. Sci. 1889; 98: 219-243.

19 Gluck T, Berl. Klein. Wochenschr. 1891; 21: 79.

20 Bush LF, J. Bone Joint Surg. 1947; 29A: 620.

21 Urist MR, Science 1965; 150: 893.

22 Cameron DA, The biochemistry and physiology of bone. 1972: Academic. 191-236.

23 Martin RB, Burr DB, and Sharkey NA, Skeletal tissue mechanics. 1998: Springer.

24 Hing KA, Phil. Trans. R. Soc. Lond. 2004; 362A: 2821-2850.

25 McConnel D, Apatite. 1973: Springer.

26 Posner AS, Physiol. Rev. 1969; 49: 760-792.

27 Suchanek W and Yoshimura M, Journal of Materials Research 1998; 13: 94-117.

28 Elliot JC, Structure and chemistry of the apatites and other calcium orthophosphates. 1994, New York: Elsevier.

29 Le Geros RZ and Le Geros JP, Dense hydroxyapatite. An introduction to biocramics, ed. J.W. L. L. Hench. 1993: World Scientific. 39-180.

30 Posner AS, Physiol. Rev. 1969; 49: 760-792.

31 Bourne GH, The chemistry and physiology of bone. 1972: Academic. 1-4.

32 Frikemeier CG, The Journal of Bone & Joint Surgery 2006; 84: 454-464.

33 Cockin J, J. Bone Jt. Surg. 1971; 53B: 153.

34 Younger EM and Chapman MW, J. Orthop. Trauma 1989; 3: 192-195.

35 Boyce T, Edwards J, and Scarborough N, Orthop. Clin. North Am. 1999; 30: 571-581.

36 Palmer SH, Gibbons CL, and Athanasou NA, J. Bone Joint Surg. Br. 1999; 81: 333-335.

37 Niederauer GG, Lee DR, and Sankaran S, Sports Med. arthrosc. Rev. 2006; 14: 163-168.

38 Laesson S and Bauer TW, Clinical Orthopaedics and Related Research 2002; 395: 23-32.

39 Brown WE and Chow LC, Cements Research Progress -1987, ed. P.W. Brown. 1988, Westerville, OH: The American Ceramic Society. 351.

40 Martin RI and Brown PW, J. Mater. Sci. Mater. Med. 1995; 6: 138.

41 Brown PW, Martin RI, and TenHuisen KS, Bioceramics: Materials and Applications, ed. R.P. Rusin and G.S. Fishman. Ceramic Transactions Vol.48. 1995: American Ceramic Society. 37.

42 Fulmer MT and Brown PW, J. Mater. Res. 1993; 8: 1687.

43 Ishikawa K, Miyamoto Y, Kon M, Nagayama M, Asaoka K, Biomater. 1995; 16: 527.

44 Tamura J, et al., J. Biomed. Mater. Res. 1984; 29: 551.

45 Gross V and Brandes J, J Biomed Mater Res 1981; 15: 291-305.

46 Cao W and Hench LL, Ceramic Int. 1996; 22: 493-507.

47 Eppley BL and Prevel CD, J. Craniofac. Surg. 1997; 8: 103-109.

48 Kumar AV, Staffenberg DA, and Petronio JA, J. Craniofac. Surg. 1997; 8: 97-99.

49 Weisberger EC and Eppley B, Laryngoscope 1997; 107: 716-719.

50 Bostman O, MakelaEA, and Sodergard J, J. Pediatr. Orthop. 1993; 13: 242-245.

51 Ishaug-Riley SI, Crane-Kruger GM, Yaszemski MJ, and Mikos AG, Biomaterials 1998; 19: 1405-1412.

52 Czernuszka JT and Lawson AC, Proc Instn Mech Engrs H 1998; 212: 413-425.

53 Ma PX and Wei G, Biomaterials 2004; 25: 4749-4757.

54 Wang Y, et.al., Journal of Materials Science: Materials in Medicine 2005; 16: 341-345.

55 Zhang LJ, et.al., Materials Letters 2004; 58: 719-722.

56 Yoshikawa H, et.al., Biomaterials 2005; 26: 73-79.

57 Elliott JC, Mackie PE, and Young RA, Science 1973; 180: 1055-1057.

58 Chappell H, Atomistic Simulations of Hydroxyapatite. 2006, University of Cambridge: Cambridge, U.K.

59 Young RA and Elliott JC, Arch. Oral Biol. 1966; 11: 699-707.

60 Lazic S, Zec S, Miljevic N, and Milonjic S, Thermochimica Acta 2001; 374: 13-21.

61 Kim SR, et al., Biomaterials 2003; 24: 1389-1398.

62 Bigi A, Boanini E, and Rubini K, Journal of Solid State Chemistry 2004; 177: 3092-3098.

63 Kumar R, Prakash KH, Yennie K, Cheang P, and Khor KA, Key Eng Mater 2005; 284-286: 59-62.

64 Calixto de Andade M, Filgueiras MRT, and Ogasawara T, Journal of European Ceramic Society 2002; 22: 505-510.

65 Jinawath S, Polchai D, and Yoshimura M, Mater Sci Eng C 2002; 22: 35-39.

66 Yoshimura M, Sujaridworakun P, Koh F, Fujiwara Takeshi, Pongkao D, and Ahniyaz Anwar, Mater Sci Eng C 2004; 24: 521-525.

67 Zhang F, Zhou ZH, Yang SP, Mao LH, Chen HM, and Xu XB, Materials Letters 2005; 2005: 1422-1425.

68 Zhang X and Vecchio KS, J Cryst Growth 2007; 308: 133-140.

69 Nakahira A, Sakamoto K, Yamaguchi S, Kaneno M, Takeda S, and Okazaki M, J Am Ceram Soc 1999; 82: 2029-32.

70 Shih WJ, Chen YF, Wang MC, and Hon MH, Journal of Crystal Growth 2004; 270: 211-218.

71 Jaffee EB, Geological Survey Circular 1951; 135.

72 Verbeeck RMH, de Maeyer EAP, and Driessens FCM, Inorg. Chem. 1995; 34: 2084.

73 Elliott JC and Young RA, Nature 1967; 214: 904.

74 Dickens B, Schroeder LW, and Brown WE, J Solid State Chem 1974; 10: 232-248.

75 Terpstra RA, Driessens FCM, Schaeken HG, and Verbeeck RMH, Z Anorg Allg Chem 1983; 507: 206-212.

76 Enderle R, Gotz-Neunhoeffer F, Gobbels M, MÜller FA, and Greil P, Biomaterials 2005; 26: 3379-3384.

77 Gregory TM, Moreno EC, Patel JM, and Brown WE, J. Res. Natn. Bur. Stands. 1974; 78A: 667-674.

78 Gibson IR, Rehman I, Best SM, and Bonfield W, Journal of Materials Science: Materials in Medicine 2000; 12: 799-804.

79 Prieto Valdes JJ, Ortiz Lopez J, Rueda Morales G, Pacheco Malagon G, and Prieto Gortcheva V, Journal of Materials Science: Materials in Medicine 1997; 8: 297-301.

80 Manjubala I, Sastry TP, and Suresh Kumar RV, Journal of Biomaterials Application 2005; 19: 341-360.

81 Yang DJ, et al., Key Engineering Materials 2006; 309-311: 227-230.

82 Yang X and Wang Z, J. Mater. Chem. 1998; 8: 2237-2244.

83 Lin F, Liao C, Chen K, Sun J, and Lin C, Journal of Biomedical Materials Research 2000; 51A: 157-163.

84 Kaplan DL, Curr Opin Solid State Mater Sci 1998; 3: 232-236.

85 Belcher AM, Wu XH, Christensen RJ, Hansma PK, Stucky GD, and Morse DE, Nature 1996; 381: 56-58.

86 Sudo S, et al., Nature 1997; 387: 563-564.

87 Lin A, Meyer MA, and Vecchio KS, Mater. Sci. Eng. C 2006; 26: 1380-1389.

88 White E and Shore EC, Dental Clinics of North America 1986; 30: 25.

89 Roy DM and Linnehan S, Nature 1974; 247: 220-222.

90 Itatani K, Takahashi M, Howell FS, and Aizawa M, Journal of Materials Science: Materials in Medicine 2002; 13: 707-713.

91 Famery R, Richard N, and Boch P, Ceram. Int. 1994; 20: 327-336.

92 Tampieri A, Celotti G, Szontagh F, and Landi E, Journal of Materials Science: Materials in Medicine 1997; 8: 29-37.

93 Itatani K, Nishioka T, Seike S, Howell FS, Kishioka A, and Kinoshita M, J. Am. Ceram. Soc. 1994; 77: 801-805.

94 LeGeros RZ, Gatti AM, Kijkowska R, Mijares DQ, and LeGeros JP, Key Eng Mater 2004; 254-256: 127-130.

95 Camprasse S, Camprasse G, Pouzol M, and Lopez E, Clin Mater 1990; 5: 235-250.

96 Lamghari M, et al., Bone 1999; 25: 91S-94S.

97 Lopez E, Vidal B, Berland S, Camprasse S, Camprasse G, and Silve C, Tissue Cell 1992; 24: 667-79.

98 Atlan G, et al., Biomaterials 1999; 20: 1017-1022.

99 Xu Y, Wang DZ, Yang L, and Tang HG, Mater Charact 2001; 47: 83-87.

100 Rocha JHG, Lemos AF, Agathopoulos S, Kannan S, and Ferreira JMF, J Biomed Mater Res Part A 2006; 77: 160-168.

101 Zaremba CM, Morse DE, Mann S, Hansma PK, and Stucky GD, Chem Mater 1998; 10: 3813-3824.

102 Zhang X and Vecchio KS, Mater Sci Eng C 2006; 26: 1445-1450.

103 Ni M and Ratner BD, Biomaterials 2003; 24: 4323-4331.

104 Kinard FW, J Chem Educ 1980; 57: 783-784.

105 Nyquist RA, Putzig CL, and Leugers MA, The handbook of infrared and Raman spectra of inorganic compounds and organic salts. 1997, San Diego: Academic press. 78-79.

106 Bakmain J, Hannoyer B, and Lopez E, J Biomed Mater Res 1999; 48: 749-754.

107 Chen B, Peng X, and Fan J, Key Eng Mater 2005; 288-289: 673-676.

108 Chateigner D, Hedegaard C, and Wenk HR, J Struct Geol 2000; 22: 1723-1735.

109 Menig R, M.M., Meyers MA, Vecchio KS, Mater Sci Eng A 2001; 297: 203-211.

110 Hou DF, Zhou GS, and Zheng M, Biomaterials 2004; 25: 751-756.

111 Kamat S, Su X, Ballarini R, and Heuer AH, Nature 2000; 405: 1036-1040.

112 Hing KA, Int J Appl Ceram Technol 2005; 2: 184-199.

113 Peters F and Reif D, Mat-wiss u Werkstofftech 2004; 35: 203-207.

114 Kondo N, et.al., Biomaterials 2005; 26: 5600-5608.

115 Koepp HE, et al., J Biomed Mater Res Part B: Appl Biomater 2004; 70: 209-217.

116 Matsushita N, et al., J Biomed Mater Res Part A 2004; 70: 450-458.

117 Miranda P, Saiz E, Gryn K, and Tomsia AP, Acta Biomaterialia 2006; 2: 457-466.

118 Kumta PN, Sfeir C, Lee DH, Olton D, and Choi D, Acta Biomaterialia 2005; 1: 65-83.

119 Toba Y, Kajita Y, Masuyama R, Takada Y, Suzuki K, and Aoe S, J Nutr 2000; 130: 216-220.

120 Weber JN, White EW, and Lebiedzik J, Nature 1971; 233: 337-339.

121 Su X, Kamat S, and Heuer AH, J Mater Sci 2000; 35: 5545-5551.

122 Politi Y, Arad T, Klein E, Weiner S, and Addadi L, Science 2004; 306: 1161-1164.

123 Raz S, Hamilton PC, Wilt FH, Weiner S, and Addadi L, Adv Funct Mater 2003; 13: 480-486.

124 Towe KM, Science 1967; 157: 1048-1050.

125 Donnay G and Pawson DL, Science 1969; 166: 1147-1150.

126 Nissen HU, Science 1969; 166: 1150-1152.

127 Rezwan K, Chen QZ, Blaker JJ, and Boccaccini AR, Biomaterials 2006; 27: 3413-3431.

128 Klawitter JJ, Bagwell JG, Weinstein AM, and Sauer BW, J. Biomed. Mater. Res. 1976; 10: 311-323.

129 Klawitter JJ and Hulbert SF, J. Biomed. Mater. Res. Symp. 1971; 2: 161-229.

130 Boletzky Sv, Sepia officinalis. Cephalopod life cycles, ed. B. PR. Vol. I. 1983, New York: Academic. 31-53.

131 Birchall JD and Thomas NL, Journal of Materials Science 1983; 18: 2081-2086.

132 Sherrard KM, Biol. Bull. 2000; 198: 404-414.

133 Denton EJ and Gilpin-Brown JB, J. Mar. Biol. Assoc. 1961; 41: 319.

134 Law SL, Lo WY, Lin FM, and Chang CH, International Journal of Pharmaceutics 1992; 84: 161-166.

135 Yamamura K, Iwata H, Osada T, Yotsuyanagi T, and Nabeshima T, Japanese Journal of Pharmacology 1994; 66: 433-438.

136 Laurencin CT, et al., Biomaterials 2001; 22: 1271-1277.

137 Ripamonti U and Ma S, Reddi ah matrix 1992; 12: 202-212.

138 Yoshimura M and Suda H, Hyd*roxyapatite and Related Materials, e*d. C.B. Brown PW. Vol. 45. 1994, Boca Raton, Florida.

139 Vecchio KS, Zhang X, Massie JB, Wang M, and Kim CW, Acta Biomaterialia 2007; 3: 910-918.

140 De Maeyer EAP, Verbeeck RMH, and Naessens DE, J. Crystal Growth 1994; 135: 539.

141 Ishikawa K and Eane ED, J. Dent. Res. 1993; 72: 474.

142 Cuneyt Tas A and Bhaduri SB, J. Am. Ceram. Soc. 2004; 87: 2195.

143 Kandori K, Shimizu T, Yasukawa A, and Ishikawa T, Colloids Surf. B 1995; 5: 81.

144 Kandori K, Saito M, Takebe T, Yasukawa A, and Ishikawa T, J. Colloid Interface Sci. 1995; 174: 124.

145 Kandori K, Fudo A, and Ishikawa T, Colloids Surf. B 2002; 24: 145.

146 Suchanek W, Yashima M, Kakuhana M, and Yoshimura M, Biomaterials 1996; 17: 1715.

147 Suchanek W, Yashima M, Kakihana M, and Yoshimura M, J. Am. Ceram. Soc. 1997; 80: 2805.

148 Shih WJ, Chen YF, Wang MC, Hon MH, J. Crystal Growth 2004; 270: 211.

149 Kay MI, Young RA, and Posner AS, Nature 1964; 204: 1050.

150 Fujishiro Y, Yabuki H, Kamakura K, Sato T, and Okuwaki A, J. Chem. Technol. Biotechnol. 1993; 57: 349.

151 Kandori K, Horigami N, Yasukawa A, and Ishikawa T, J. Am. Ceram. Soc. 1997; 80: 1157.

152 Ban S and Maruno S, J. Biomed. Mater. Res. 1998; 42: 387.

153 Ando J, Bull Chem Soc Jpn 1958; 31: 196-201.

154 Yashima M and Sakai A, Chem. Phys. Lett. 2003; 372: 779-783.

155 Wolff DMB, Ramalho EG, and Acchar W, Materials Science Forum 2006; 530-531: 581-586.

156 Marchi J, et.al., Materials Research Bulletin 2007; 42: 1040-1050.

157 De Groot K, Bioceramics of Calcium Phosphate. 1983, Boca Raton, Florida: CRC Press.

158 Lagier R and Baud CA, Pathology - Research and Practice 2003; 199: 329-335.

159 Ryan LM, et al., Calcif. Tissue Int. 1999; 65: 374-377.

160 Vecchio KS, Zhang X, Massie JB, Wang M, and Kim CW, Acta Biomaterialia 2007; 3: 785-793.

161 Destainville A, Champion E, Bernache-Assollant D, and Laborde E, Mater. Chem. and Phys. 2003; 80: 269-277.

162 Kannan S, Lemos AF, Rocha JHG, and Ferreira JMF, J. Am. Ceram. Soc. 2006; 89: 2757-2761.

163 Menig R, Meyers MH, Meyers MA, and Vecchio KS, Acta Materialia 2000; 48: 2383-2398.

164 Menig R, Meyers MH, Meyers MA, and Vecchio KS, Materials Science & Engineering A 2001; 297: 203-211.

165 Wachtman JB, Mechanical Properties of Ceramics. 1996, New York: Wiley-Interscience.

166 Smith L, Arch Surg 1963; 87: 653-661.

167 Lu JX, et al., J. Mater. Sci. Mater. Med. 1999; 10: 111-120.

168 Rubin PA, Popham JK, Bilyk JR, and Shore JW, Ophthal. Plast. Reconstr. Surg. 1994; 10: 96-103.

169 Hing KA, Best SM, Tanner KE, Bonfield W, and Revell PA, J. Biomed. Mater. Res. A 2004; 68: 187-200.

170 Li S, De Wijn JR, Li J, Layrolle P, and De Groot K, Tissue Eng. 2003; 9: 535-548.

171 Holmes R, Mooney V, Bucholz R, and Tencer A, Clin. Orthop 1984; 188: 252-262.

172 Hing KA, Best SM, and Bonfield W, J. Mater. Sci. Mater. Med. 1999; 10: 135-145.

173 Holmes RE, Plast. Reconstr. Surg. 1979; 63: 626-633.

174 Bignon A, et.al., J. Mater. Sci. Mater. Med. 2003; 14: 1089-1097.

175 Boyde A, Corsi A, Quarto R, Cancedda R, and Bianco P, Bone 1999; 24: 579-589.

176 Hing K, et.al., J. Mater. Sci. Mater. Med. 2005; 16: 467-475.